

LOW-TEMPERATURE PROCESSING FOR AEROSOL-JET PRINTED SILVER
CONTACTS

By

Atef M. Abu-Ageel

A DISSERTATION

Submitted to
Michigan State University
in partial fulfillment of the requirements
for the degree of

Electrical Engineering - Doctor of Philosophy

2021

ABSTRACT

LOW-TEMPERATURE PROCESSING FOR AEROSOL-JET PRINTED SILVER CONTACTS

By

Atef M. Abu-Ageel

After 3D printing was commercialized in the early 1990s, the industry experienced huge interest from tool developers who capitalized on additive manufacturing and enjoyed noticeable growth as a result. Multiple industries are weighing the benefits of 3D printing and what it can offer in terms of savings in operations cost and also adding new features to their customers. It is predicted that the global 3D market in terms of equipment, materials, software, and services will reach \$31 billion by 2030 according to industry analysts.

Electronic devices' major fabrication element is the creation of conductive structures and interconnects utilizing additive or subtractive processes. Most electronic systems are fabricated using photolithography, which is a subtractive process that is frequently complex and time-consuming using expensive clean facilities. Furthermore, this process generates large amounts of harmful waste in most cases. 3D inkjet printing techniques for the purpose of fabricating electronic devices are less expensive compared to photolithography. 3D printing has recently begun to be attractive as a potential technology to supersede lithographic processes for lower-volume and rapidly emerging areas. For example, conductive silver inks cover a wide range of markets, including organic light emitting diodes, photovoltaics, antennas, ceramic capacitors, radio frequency identification, medical devices, and many more. The high conductivity of metals printed using materials like silver or copper inks gives the flexibility to print thinner and longer circuit trace lines on complex geometries without compromising overall resistivity values, which can result in major cost savings for rapid prototyping and low-volume situations.

In this work, silver ink is used to form a contact material that could be used as an ohmic metal contact material realized at low processing temperatures for soft electronic material applications such as organic light emitting diodes and transparent photovoltaics. The silver ink is printed using Aerosol Jet Printing technology and cured using an optical heating pulse system and can result in useful metal contacts without exceeding 35°C. The proposed technique does not require a cleanroom environment. This makes the proposed method of printing the contacts in ambient conditions cost-efficient and easy to implement without significantly sacrificing performance when higher temperature processing cannot be used.

I dedicate my dissertation work to my wife Shantell and my children Michael, Chelsea, Zakariah, Khaled, Gabriel and Layla. I dedicate this dissertation to my wife Shantell who has been an endless source of support and motivation during challenging times. A special feeling of gratitude to my loving mother Fatmeh Alhawamdeh whose words of encouragement and push for persistence are embedded in my heart. I also dedicate this dissertation to my father Mohammad Abu Ageel who passed away in 2012 and who always believed in me. My sisters Makarem, Nawal, Wafa'a and Fatena and my brothers Nayef, Nawwaf, Nezar and Malek who always have never left my side and are very special.

Once again, I dedicate this work and give special thanks to my best friend and awesome wife Shantell for being there for me throughout the entire graduate program. You have been my best cheerleader.

ACKNOWLEDGEMENTS

I wish to thank my committee members who were more than generous with their expertise and precious time. A special thanks to Dr. John Albrecht, my committee chairman for his guidance, reading, encouraging, dedication and most of all patience throughout the entire process. I thank Dr. Richard Lunt, Dr. Virginia Ayres, Dr. Wen Li and Dr. John Papapolymerou for agreeing to serve on my committee. I would like to acknowledge and thank the College of Engineering for allowing me to conduct my research and providing any assistance requested. Special thanks go to the Electrical Engineering staff members Brian Wright and Meagan Kroll for their continued support.

Many thanks to my wife Shantell, for your encouragement, support, confidence, and love. You've inspired me to give my best effort and always reach higher, I will continue striving to make you proud.

I thank my colleagues in the MOE Lab for their presence during devices fabrication; Dr. Patty Pillai, for spending the time and walking me through the process of the OLED devices fabrication, your efforts were remarkable. To my friend Matt Bates, who was very patient and his willingness to go above and beyond, spending long hours in the lab during the fabrication and testing; you are truly a gentleman.

I would like to thank Kim Trapp at Enovate Medical for her encouragement and support. I also would like to thank my coworkers at Froude, Inc. for their support and encouragement, especially, Chris Walker, Andy Sadlon, Mike Golda, Julie Smith and Juliann Blanford for their faith and support. I appreciate my other friends: Terry O'Connell, Dan Sutton, Diane Nossal, Chris

Middlemass, Mike Mardis, Darrick Henry and Matt Janisse. I also would like to thank Chris Walker for helping me in formatting my dissertation.

TABLE OF CONTENTS

LIST OF TABLES	x
LIST OF FIGURES	xii
KEY TO SYMBOLS AND ABBREVIATIONS	xvii
CHAPTER 1: INTRODUCTION	1
1.1 Motivation	1
1.2 Problem Statement	1
1.3 Literature Review	3
1.4 Proposed Method.....	7
1.5 Dissertation Organization.....	8
CHAPTER 2: EXPERIMENTAL TECHNIQUES	11
2.1 3D Printing - General Purpose	11
2.1.1 Objet Connex350™ Printer	11
2.1.2 Ink - 3D Printing Material	12
2.1.3 Design File Requirement.....	13
2.2 3D Printing - Metallic Silver for Electronic Applications	14
2.2.1 Optomec Aerosol Jet® 5X Printer	14
2.2.2 Clariant EXPT Prelect TPS 50G2 Silver Ink	15
2.2.3 Design File Requirement.....	15
2.3 3D Printing - Curing Techniques	16
2.3.1 Hot Plate	16
2.3.2 H3S Basics	16
2.4 3D Printed Electronics - Electronic Properties Characterization	18
2.4.1 Conductivity	18
2.4.2 Transmission Line Measurements.....	19
2.5 3D Printed Electronics - Physical and Materials Properties Characterization	19
2.5.1 Surface Profiler	19
2.5.2 Thermogravimetric Analysis.....	20
2.5.3 Scanning Electron Microscope.....	21
2.5.4 Grain Size Measurement	22
CHAPTER 3: 3D PRINTED COMPONENTS AND APPLICATIONS.....	24
3.1 Overview	24
3.2 3D Printing for Education, Research and Entrepreneurship	24
3.2.1 Maple-seed Robotic Flyer	24
3.2.2 3D Inkjet-Printed MRF	25
3.2.3 3D Print Material.....	26
3.2.4 Learners Evaluation.....	27
3.2.5 Conclusion.....	28
3.3 Phosphor-based Optical Cavity	28

3.3.1	History and Goal	28
3.3.2	Optical Cavity Design	29
3.3.3	System Design using Collimating and Focusing Lenses	31
3.3.4	Performance Analysis	32
3.3.5	Discussion and Conclusion	33
CHAPTER 4:	METAL AEROSOL JET PRINTING	35
4.1	Motivation	35
4.2	Three Transmission Line Test Circuits	36
4.3	Design and AJP of Silver Ink Squares	37
4.3.1	Material Thickness and Conductivity Measurements	38
4.4	Transmission Line (Type-1a)	40
4.4.1	Material Thickness Measurement (Type-1a)	41
4.4.2	RF Data Measurement (Type-1a)	42
4.5	Transmission Line (Type-1b)	43
4.5.1	Material Thickness Measurement (Type-1b)	44
4.5.2	RF Data Measurement (Type-1b)	44
4.6	Transmission Line (Type-2)	45
4.7	Transmission Line (Type-3)	45
4.7.1	Material Thickness Measurement (Type-3)	46
4.7.2	RF Data Measurement (Type-3)	47
4.8	Highly Conductive Ink for Flexible Electronic Devices	47
4.8.1	Metal Organic Silver Ink	48
4.8.2	Experimental Circuit Fabrication	49
4.8.3	Results and Discussion	51
4.9	Conclusion	54
CHAPTER 5:	3D PRINTED ELECTRONICS WITH OPTICAL CURING	57
5.1	3D Printed Silver Ink Test Structures on Glass Substrates	57
5.2	Optical Pulse Heating Profile and Exposure Time	57
5.3	Sample Mounting for Optical Curing in the H3S	59
5.4	Sintering Results	60
5.5	Layer Thickness Measurements	64
5.6	Conductivity Measurement	65
5.7	Summary of Fabrication vs Conductivity	68
5.8	Silver Contact Uniformity Using SEM	69
5.9	Sample Preparation for SEM	70
5.10	Initial Material Uniformity Investigations with Film Thickness Measurements	71
5.11	Summary of Initial Thickness Investigations	74
5.12	Nanocrystalline Morphology and Grain Size Investigation	75
5.13	Grain Size Analysis	83
5.13.1	Sample Calculation	83
5.13.2	Analysis of Grain Uniformity	85
5.14	Film Composition by EDS Analysis	86
5.15	Grain Boundary Analysis	89
5.16	Conclusion	92

CHAPTER 6:	CONCLUSION AND FUTURE WORK	94
6.1	Conclusion.....	94
6.2	Future Work	96
6.2.1	MRF Microfabrication	97
6.2.2	Inkjet Printing of Optical Cavity Reflective Mirror	97
6.2.3	Future Inkjet Printed OLED Structure	97
6.2.4	Other Methods of Curing Silver Ink	99
APPENDIX.....		103
BIBLIOGRAPHY.....		119

LIST OF TABLES

Table 1 - Summary of the literature survey of 3D printed material characteristics and properties	5
Table 2 - 3D printing literature survey summary of various techniques' advantages and disadvantages.....	6
Table 3 - VeroWhite Plus physical properties	13
Table 4 - Learning lab questionnaire results	27
Table 5 - Throughput analysis of the optical cavity for four design variations	33
Table 6 - Desired temperature and exposure time for the samples	59
Table 7 - Measured sample temperatures during sintering for 20-30 minutes at 35°C	61
Table 8 - Measured sample temperatures during sintering for 50 minutes at 100°C	62
Table 9 - Conductivity and % of bulk silver conductivity measurement summary at 35°C.....	66
Table 10 - Conductivity and % of bulk silver conductivity measurement summary at 100°C.....	67
Table 11 - Material thickness comparison between NanoMap 500LS and SEM	74
Table 12 - Average, standard deviation and S.E.M calculations for 5 imaged Ag grains in 1-layer printed Ag (a) post curing and (b) post storage.	84
Table 13 - Conductive volume calculations.....	85
Table 14 - Lattice mismatch compared to 2.942 Å for pure cubic Ag.....	90
Table 15 - Comparison of curing technologies	92

Table 16 - Grain size measurement for 1-layer sintered at 35°C for 20 minutes - September 2019	104
Table 17 - Grain size measurement for 1-layer sintered at 35°C for 20 minutes - after storage	105
Table 18 - Grain size measurement for sample 3 - after storage	106
Table 19 - Average, standard deviation and S.E.M calculations for sample 3	106
Table 20 - Grain size measurement for sample 4 - after storage	108
Table 21 - Average, standard deviation and S.E.M calculations for sample 4	108
Table 22 - Grain size measurement for sample 5 - after storage	110
Table 23 - Average, standard deviation and S.E.M calculations for sample 5	110
Table 24 - Grain size measurement for sample 6 - after storage	112
Table 25 - Average, standard deviation and S.E.M calculations for sample 6	112
Table 26 - Grain size measurement for sample 7 - after storage	114
Table 27 - Average, standard deviation and S.E.M calculations for sample 7	115
Table 28 - Grain size measurement for sample 8 - after storage	116
Table 29 - Average, standard deviation and S.E.M calculations for sample 8	116
Table 30 - Samples post curing and post storage summary	118

LIST OF FIGURES

Figure 1 - (a) Objet Connex350 TM printer (b) Printer parts	12
Figure 2 - (a) 3D part in STL format, (b) ASCII file format, and (c) Binary file format	14
Figure 3 - (a) Aerosol Jet 5X printer (b) Printer parts	15
Figure 4 - KEWA TM motion manager software	16
Figure 5 - (a) H3S and (b) System components.....	17
Figure 6 - (a) Pro4-440N configuration (b) Probe separation distance (c) Measurement result display.....	19
Figure 7 - (a) NanoMap 500LS profilometer (b) Silver ink sample under test	20
Figure 8 - TA TGA Q500 thermogravimetric analyzer	20
Figure 9 - (a) JEOL JSM-7500F field emission SEM system (b) JEOL cold cathode FE SEM column cross section.....	21
Figure 10 - (a) R-filter selectively detects secondary and backscattered electrons (b) Energy ranges selected by the R-filter	22
Figure 11 - Design of MRFs with (a) 1-wing (b) 4-wings.....	26
Figure 12 - (a) Cross-sectional view and (b) 3D design of the optical cavity	30
Figure 13 - Light source (a) prototype with a green light optical cavity and (b) assembly during operation	31
Figure 14 - Laser light coupling using (a) collimating and (b) focusing lenses.	32

Figure 15 - Phosphor Absorption for (a) Version 1 and (b) Version 2.....	33
Figure 16 - (a) 10mm x 10mm silver ink square sketch (b) VMTools™ properties(c) 10mm x 10mm serpentine fill (d) 3D printed model on glass substrate.....	37
Figure 17 - Silver ink (a) step height and (b) average roughness (R_a) measurements.....	38
Figure 18 - (a) Pro4 setup, (b) Silver ink material geometry, and (c) SP4 4-point probe head....	40
Figure 19 - (a) CPWG sketch (b) CPWG serpentine fill (c) VMTools™ properties (d) 3D printed model (e) Feature size measurement	41
Figure 20 - Type-1a Silver ink (a) step height measurement and (b) average roughness (R_a).....	42
Figure 21 - Type-1a RF measurement	42
Figure 22 - (a) CB-CPW sketch (b) CB-CPW serpentine fill (c) VMTools™ properties (d) 3D printed model (e) Feature size measurement.....	43
Figure 23 - Type-1b RF measurement	44
Figure 24 - (a) CPWG sketch (b) CPWG serpentine fill (c) VMTools™ properties (d) 3D printed model on DuPont AC182500EM (e) 3D printed model on 1mil Kapton tape (f) Feature size measurement.....	46
Figure 25 - Type-3 RF measurement	47
Figure 26 - (a) Flexible film (b) Foldable film (c) Resistivity measurement	50
Figure 27 - TGA measurement of the Clariant ink diluted with deionized water in dry air.....	51
Figure 28 - (a) Electrical conductivity of printed and sintered Ag as a function of temperature and sintering time (b) 10 x 10 mm silver ink layers sintered on a hot plate.	52

Figure 29 - Shrinking behavior of the printed Ag layer printed on glass substrate and sintered on a hot plate	52
Figure 30 - Simulated and measured insertion loss per millimeter and return loss for different susbtartes: LCP (a) and Kapton (b)	54
Figure 31 - (a) Dual samples (b) Single sample	59
Figure 32 - (a) Heater crystal in place (b) Heater ON	60
Figure 33 - Time vs. temperature to stabilize at (a) 35°C and (b) 100°C	63
Figure 34 - Cured samples stored in vacuum desiccator	64
Figure 35 - (a) NanoMap 500LS from AEP Technology (b) Sample measurement result	64
Figure 36 - Silver thickness and roughness vs No. of printed layers at (a) 35°C and (b) 100°C ..	65
Figure 37 - Resistivity (ρ) and conductivity (σ) vs No. of printed layers at 35°C	66
Figure 38 - Resistivity (ρ) and conductivity (σ) vs No. of printed layers at 100°C	67
Figure 39 - Conductivity as %-Ag conductivity for (a) Thermally cured (b) Optically cured at 35°C and 100°C	69
Figure 40 - (a) Samples 2 and 4 mounted on aluminum stub (b) Pure osmium coater Neoc-AN (c) JEOL JSM-7500F SEM	71
Figure 41 - SEM micrographs of cross-sections of printed silver regions after light-pulse sintering at 35°C with the number of printed layers and sintering times indicated for each row. Column (a) shows the broad scan of the cross-section samples, including the damage from the liquid nitrogen fracture process used for preparation. Column (b) shows that the regions of printed silver are uniform across the micron scale.	72

Figure 42 - SEM micrographs of cross-sections of printed silver regions after light-pulse sintering at 100°C with the number of printed layers and sintering times indicated for each row. Column (a) shows the broad scan of the cross-section samples, including the damage from the liquid nitrogen fracture process used for preparation. Column (b) shows that the regions of printed silver are uniform across the micron scale.....	73
Figure 43 - Material thickness after (a) 35°C and (b) 100°C curing using NanoMap and SEM ..	74
Figure 44 - Post curing SEM measurement for 1-layer sample sintered at: (a) and (c) 35°C for 20 minutes. (b) and (d): Post storage SEM measurement	76
Figure 45 - Post curing SEM measurement for 1-layer sample sintered at: (a) and (c) 100°C for 50 minutes. (b) and (d): Post storage SEM measurement	77
Figure 46 - Post curing SEM measurement for 3-layer sample sintered at: (a) 35°C for 30 minutes (c) 100°C for 50 minutes. (b), (d) and (e): Post storage SEM measurement	78
Figure 47 - Post curing SEM measurement for 5-layer sample sintered at: (a) and (c) 35°C for 30 minutes. (b) and (d): Post storage SEM measurement	79
Figure 48 - Post curing SEM measurement for 5-Layer sample sintered at: (a) and (c) 100°C for 50 minutes. (b) and (d): Post storage SEM measurement	80
Figure 49 - Post curing SEM measurement for 10-layer sample sintered at: (a) 35°C for 30 minutes (c) 100°C for 50 minutes. (b) and (d): Post storage SEM measurement.....	81
Figure 50 - Post curing SEM measurement for 15-layer sample: (a) Damage due to liquid nitrogen fracture (c) sample sintered at 35°C for 30 minutes. (b) and (d): Post storage SEM measurement.....	82

Figure 51 - Post curing SEM measurement for 15-layer sample: (a) Damage due to liquid nitrogen fracture (c) sample sintered at 100°C for 50 minutes. (b) and (d): Post storage SEM measurement.....	83
Figure 52 - Measured grain dimensions and the processed SEM images from which they were extracted for the 1-layer printed Ag (a,b) post curing and (c,d) after storage, respectively.....	84
Figure 53 - Grain size measurement histogram for printed films post storage.....	86
Figure 54 - (a) Ag-O film (b) Ag-O-Cl Crystallites (c) Glass substrate	88
Figure 55 - Dense nanocrystalline films for growth conditions (a) 35°C for 20 min and (b) 100°C for 50 min.	90
Figure 56 - (a) An electron traversing an Ag grain versus an Ag ₂ O grain boundary experiences an orders of magnitude difference in resistance. (b) Materials and geometric properties both influence whether transport is volumetric or along grain boundaries.	91
Figure 57 - Proposed 3D print OLED device structure	99
Figure 58 - Sample 3 (a) Grain vs length (nm) (b) Processed image	107
Figure 59 - Sample 4 (a) Grain vs length (nm) (b) Processed image	109
Figure 60 - Sample 5 (a) Grain vs length (nm) (b) Processed image	111
Figure 61 - Sample 6 (a) Grain vs length (nm) (b) Processed image	113
Figure 62 - Sample 7 (a) Grain vs length (nm) (b) Processed image	115
Figure 63 - Sample 8 (a) Grain vs length (nm) (b) Processed image	117

KEY TO SYMBOLS AND ABBREVIATIONS

2D	Two-Dimensional
3D	Three-Dimensional
ABS	Acrylonitrile Butadiene Styrene
Ag	Silver
AgO	Silver (II) Oxide
AgO ₂	Silver (I) Oxide
Ag ₂ O	Silver (I) Oxide
Ag ₂ O ₃	Silver (I,III) Oxide
Ag ₄ O ₄	Tetrasilver Tetroxide
AJP	Aerosol Jet Printing
Alq ₃	Tris (8-hydroxyquinoline) aluminum (III)
ASA	Acrylonitrile Styrene Acrylate
ASCII	American Standard Code for Information Interchange
BMP	Bitmap
BST	Barium Strontium Titanate
CAD	Computer-Aided Design
CB-CPW	Conductor-Backed Coplanar Waveguide
CCD	Center for Coatings and Diamond
CHCL ₃	Chloroform
Cl	Chlorine
CNT	Carbon Nanotubes

CPW	Coplanar Waveguide
CPWG	Coplanar Waveguide
DICOM	Digital Imaging and Communications in Medicine
DLP	Digital Light Processing
DMF	Dimethylformamide
DPO	Diversity Program Office
DXF	Document EXchange Format
EBM	Electron Beam Melting
EDS	Energy Dispersive Spectroscopy
EMT	Effective Medium Theory
ETL	Electron Transport Layer
FCC	Face-Centered Cubic
FDM	Fused Deposition Modeling
FITS	Flexible Image Transport System
FRP	Fiber-Reinforced Plastic
GIF	Graphics Interchange Format
GPS	Global Positioning System
GUI	Graphical User Interface
H3S	Heraeus Humm3 [®] System
HIPS	High Impact Polystyrene
HTL	Hole Transport Layer
IR	Infrared
ITEC	Information Technology Empowerment Center

JPEG	Joint Photographic Experts Group
K-12	Kindergarten -12
LABE	Low-Angle Backscattered Electron
LCD	Liquid Crystal Display
LCP	Liquid Crystal Polymer
LED	Light Emitting Diode
LNF	Lurie Nanofabrication Facility
MRF	Maple-seed Robotic Flyer
MSU	Michigan State University
NP	Nanoparticle
NPD	N,N'-Di(1-naphthyl)-N,N'-diphenyl-(1,1'-biphenyl)-4,4'-diamine
O	Oxygen
OLED	Organic Light Emitting Diode
PC	Polycarbonate
PC-ABS	Polycarbonate-Acrylonitrile Butadiene Styrene
PEDOT:PSS	Poly(3,4-Ethylenedioxythiophene) Polystyrene Sulfonate
PETG	Polyethylene Terephthalate Glycol
PLA	Polylactic Acid
PP	Polypropylene
PRG	Toolpath File
PVAC	Poly Vinyl Acetate
R _a	Average Roughness
RF	Radio Frequency

RFID	Radio Frequency Identification
RGB	Red, Green and Blue
RPM	Revolutions per Minute
RTP	Rapid Thermal Process
SCCM	Standard Cubic Centimeters per Minute
SCD	Single-Crystalline Diamond
SDL	Selective Deposition Lamination
SEI	Secondary Electron Imaging
SEM	Scanning Electron Microscopy
SID	Society for Information Display
Si	Silicon
SLA	Stereolithography
SLC	Stereolithography Contour
SLM	Selective Laser Melting
SLS	Selective Laser Sintering
SOI	Silicon-On-Insulator
SSLG	Straight Solid Light Guide
STEM	Science, Technology, Engineering and Mathematics
STL	Standard Tessellation Language
TGA	Thermogravimetric Analysis
TIFF	Tagged Image File Format
TiO ₂	Titanium Dioxide
TPE	Thermoplastic Elastomer

TPV	Transparent Photovoltaic
UA	Ultrasonic Atomizer
UV	Ultraviolet
VTE	Vacuum Thermal Evaporation
WiFi	Wireless Fidelity
WPD	Wilkinson Power Divider
a	Lattice Constant
A	Ampere, Unit of Electrical Current
\AA	Angstrom, Unit of Length Equal to 10^{-10} m
$^{\circ}\text{C}$	Degree Celsius
e	Electron
g	Gram
I	Current
k	Kilo
λ	Wavelength
L	Length
m	meter
MPa	Mega Pascal, Pressure Unit
Ω	Ohm, Unit of Electrical Resistance
$\text{Pas}\cdot\text{s}$	Pascal-Second, Viscosity Unit
Φ_{solid}	Conductive Volume
ρ	Resistivity
R	Resistance

R_s	Sheet Resistance
s	Seconds
S	Siemens
σ	Conductivity
$\sigma_{eff,EMT}$	Effective Conductivity Silver Ink
t	Thickness
V	Voltage
W	Width

CHAPTER 1: INTRODUCTION

1.1 Motivation

Over the last two decades a tremendous progress in printing electronic devices has been achieved with additive manufacturing. The precision printing highly-conductive metal is a key feature for electronic device integration when it comes to the device contact layout, circuit wiring, and final system packaging [1]. Curing process conditions have a major effect on the quality of the final printed structure. As the printed metal feature sizes approach 10 microns and smaller, and the strong possibility of deformation due to the heat applied to cure the material, the curing conditions become increasingly challenging and complicated [2]. Cracks or holes can be introduced to the thin films within the device with curing temperatures of 150°C or more which negatively impacts the active materials along with lowering the final contact conductivity that can be achieved [3].

1.2 Problem Statement

In order to achieve good ohmic contacts, higher temperature and longer curing time play major roles in removing the additives from the ink particles. Most ink-jet printed materials require high sintering temperatures in order to solidify and form good contacts. Traditional spin coated materials, such as sol-gel materials that can also be inkjet-printed, require sintering temperatures above 500°C to form a dense layer free of additives [4] or over 200°C to form conductive silver nanoparticle (NP) traces [5]. For device structures that involve organic materials as the active electronic parts, it is well-known that a sintering temperature of ~150°C is needed to remove the ink additives and show useful conductivity patterns without damaging the active regions. This is fundamentally challenging since the metal ink solvents may also be organic or water based, so the same curing process can both cure the ink and destroy the devices without great care. This can be

achieved using precise annealing, like small laser spot sizes, so the surrounding materials can be protected during the curing process. In this work, a fundamentally unexplored approach is considered for overcoming the temperature incompatibility of metal ink curing. A pulsed light system that is capable of controlling three profiles during the process, i.e. pulse width, intensity and frequency has been demonstrated to cure standard printed silver ink contacts at 35°C for 30 minutes and eliminate the need of using ultraviolet (UV) or laser systems that can present potential damage to the active material. The resulting conductivity of the low-temperature cured silver is sufficient ($> 15\%$) to be used for a range of applications that do not normally require extremely low contact resistances or high power dissipations, e.g., light-emitting diodes.

Organic materials in such devices like organic light emitting diodes (OLEDs), TPVs, many flexible electronics, and electronics on paper to name a few require low temperature thermal processing conditions to cure the metal contacts of those devices. The majority of the existing curing systems from direct hot plate to UV flashing to laser sintering could affect the performance of the active material in those devices. To avoid the high temperature degradation of the active material during the sintering process a low thermal budget system is needed to perform this task without causing the active material to fail.

In this thesis, the focus is on an alternative curing process for Aerosol-Jet Printed (AJP) silver NP inks which have been previously studied extensively on glass substrates by curing with heat in ovens, hot plates, and UV flash methods for comparison. The main drawback of those methods is the high temperature ($\sim 200^\circ\text{C}$) that was needed in order to remove the silver ink additives in order to achieve good conductivity. As described above, this high sintering temperature is not adequate for most organic materials. The goal is to achieve curing at

temperatures below 150°C with total sintering times less than 1 hour, as these proposed conditions will not affect the active materials in OLED and TPV devices.

1.3 Literature Review

Three-dimensional (3D) printing techniques date back to the 1980s. In 1981, Hideo Kodama presented one of the earliest examples, a 3D solid polymer model that was hardened using UV light [6]. After early demonstrations, 3D printing technology evolved over the years by introducing computer-aided design (CAD) software to create 3D models [7] [8] which has enabled widespread industrial, commercial, and household printers to become ubiquitous through simple software. Specifically of interest to this work, printing using metal particles became practical after research groups used the same basic 3D printing concepts to print metal contacts on glass or ceramic substrates for small prototype electronic devices. For example, Jang *et al.* [9] presented a crack-free inkjet printed microstructure that can be sintered at high temperature to form reasonable conductivity metal and good adhesion to glass substrates. Direct inkjet printing is another method that was used to print highly-conductive copper patterns [10] [11].

AJP is a major technique for printing electronics with fine features [12] and the most mature AJP metal deposition processes are for silver ink NPs. High conductivity results [13] with large conductivity percentages (>80%) compared with bulk silver have been reported for AJP deposited silver under elevated thermal sintering conditions that are often incompatible with organic materials, such as organic electronics or substrates. UV flash sintering has been used recently in an attempt to mitigate the temperature intolerance issue within the organic substrate [14]. Laser sintering has also been deployed as another solution to obtain precise heating around the fine features of the electronic device, especially with active organic materials as those devices require low-temperature curing although local temperatures can be quite high [15]. Along with

oven and laser sintering, chemical sintering methods [16] and high-intensity light pulse systems [17] have also been examined as friendly curing systems to organic materials but without widespread technological success. The characteristics and properties of various 3D printed materials as surveyed in the review article [18] are summarized in Table 1. As with every technology, 3D printing techniques have their own advantages as well as drawbacks. Table 2 summarizes the pros and cons of 3D printing techniques as collected from [19] - [35].

	Acrylonitrile Butadiene Styrene (ABS)	Thermoplastic Elastomers (TPE)	Poly(lactic Acid (PLA)	High Impact Polystyrene (HIPS)	Polyethylene Terephthalate Glycol (PETG)	Nylon	Fiber-Reinforced Plastic (FRP)	Acrylonitrile Styrene Acrylate (ASA)	Polycarbonate (PC)	Polypropylene (PP)	Metal Filled	Wood Filled	Polyvinyl Alcohol (PVA)
Ultimate Strength	40 MPa	26-43MPa	65MPa	32MPa	53MPa	40-85MPa	45-48MPa	55MPa	72MPa	32MPa	20-30MPa	46MPa	78MPa
Stiffness	5/10	1/10	7.5/10	10/10	5/10	5/10	10/10	5/10	6/10	4/10	10/10	8/10	3/10
Durability	8/10	9/10	4/10	7/10	8/10	10/10	3/10	10/10	5/10	6/10	4/10	3/10	7/10
Maximum Service Temperature	98°C	60-74°C	52°C	100°C	73°C	80-95°C	52°C	95°C	121°C	100°C	52°C	52°C	75°C
Thermal Expansion Coefficient	90µm/m.°C	157µm/m.°C	68µm/m.°C	80µm/m.°C	60µm/m.°C	95µm/m.°C	57.5µm/m.°C	98µm/m.°C	69µm/m.°C	150µm/m.°C	33.75µm/m.°C	30.5µm/m.°C	85µm/m.°C
Density	1.04g/cm ³	1.19-1.23g/cm ³	1.243g/cm ³	1.03-1.04g/cm ³	1.23g/cm ³	1.06-1.14g/cm ³	1.3g/cm ³	1.07g/cm ³	1.2g/cm ³	0.9g/cm ³	2-4g/cm ³	1.15-1.25g/cm ³	1.23g/cm ³
Printability	8/10	6/10	9/10	6/10	9/10	8/10	8/10	7/10	6/10	4/10	7/10	8/10	5/10
Extruder Temperature	220-250°C	225-245°C	190-220°C	230-245°C	230-250°C	220-270°C	200-230°C	235-255°C	260-310°C	220-250°C	190-220°C	190-220°C	185-200°C
Bed Temperature	90-110°C	45-60°C	45-60°C	100-115°C	75-90°C	70-90°C	45-60°C	90-110°C	80-120°C	85-100°C	45-60°C	45-60°C	45-60°C
Heated Bed	Required	Optional	Optional	Required	Required	Required	Optional	Required	Required	Required	Optional	Optional	Required
Price (per kg)	\$10-\$40	\$30-\$70	\$10-\$40	\$24-\$32	\$20-\$60	\$25-\$65	\$30-\$80	\$38-\$40	\$40-\$75	\$60-\$120	\$50-\$120	\$25-\$55	\$40-\$110
Flexibility		✓				✓			✓				✓
Elasticity		✓											
Impact Resistance	✓			✓		✓		✓	✓				
Soft		✓								✓			✓
Composite							✓				✓	✓	
UV Resistant								✓					
Water Resistant					✓					✓			
Dissolvability				✓									✓
Heat Resistant	✓			✓		✓		✓	✓	✓			
Chemically Resistant					✓								
Fatigue Resistant		✓			✓	✓			✓	✓			✓

Table 1 - Summary of the literature survey of 3D printed material characteristics and properties

3D Printing Technique	Sintering Type	Methodology	Type of Material	Bed Plate Size	Pros	Cons	Reference
<i>Stereolithography (SLA)</i>	UV light curing	Localized copolymerization	Polymer resin materials: 1. Photo curable titanium dioxide (TiO ₂)/epoxy acrylate. 2. CNT/acrylic ester barium strontium titanate (BST)/epoxy.	7.9"x7.9"x9.9" 10"x10"x10" 20"x20"x24"	1. High resolution printed parts. 2. Nozzle doesn't clog. 3. Dental applications use.	1. High cost. 2. Cytotoxicity of residual uncured resin.	[19] [20] [21] [22] [23]
<i>Digital Light Processing (DLP)</i>	UV light curing	Photo polymerization	Liquid resin materials: 1. Polyester. 2. Vinyl ester. 3. Epoxy.	7.6"x4.7"x9.06"	1. Excellent print quality. 2. Faster than SLA printing. 3. Low cost compared to SLA.	1. Liquid resin is wet and hazardous. 2. Resin has distinct smell causing headache.	[19] [24] [25] [26] [35]
<i>Selective Laser Sintering / Melting (SLS/SLM)</i>	Sintering	Powder melting	Powder materials: 1. Polyimide powder. 2. Aluminum-filled nylon. 3. Glass-filled nylon. 4. Carbon-fiber filled nylon.	11.81"x11.81"x11.81" 29.53"x21.65"x21.65"	1. No support structure. 2. Strong final product. 3. Small to medium batch production.	1. Shrinkage and Warpage due to sintering and cooling. 2. High cost. 3. Requires post processing.	[19] [22] [27]
<i>Fused Deposition Modelling (FDM)</i>	Extrusion	Liquid polymer through nozzles	Thermoplastic materials: 1. ABS. 2. ASA. 3. Polycarbonate-acrylonitrile butadiene styrene (PC-ABS).	12"x12"x12" 24"x36"x36"	1. Precision. 2. Strength. 3. Large Builds. 4. Rapid Turnaround. 5. Low cost. 6. High speed.	1. Uses thermoplastic polymers only. 2. Filament material form only. 3. Lack of homogeneity in extruded material.	[19] [23] [28]
<i>Binder Jetting</i>	Binder technology	Localized application of binder	Sheet material foils such as: 1. Paper. 2. Metal. 3. Plastics. 4. Fiber glass	12"x12"x12"	1. High resolution. 2. Multi color capability. 3. Low cost compared to SLA and SLM.	1. Degrading inkjet process. 2. Shrinkage. 3. Lower density parts. 4. High surface roughness.	[19] [22] [29] [30]
<i>Selective Deposition Lamination (SDL)</i>	Paper bonding/laminating	Papers layering and shaping	Any sheet material such as: 1. Paper. 2. Metal. 3. Plastic. 4. Fiber glass.	12"x12"x12"	1. Low cost. 2. Ability to make full color models. 3. Precise and smooth finished parts. 4. Faster technique.	1. Requires post processing. 2. Longer build time as number of layers increase.	[19] [22] [31]
<i>Electron Beam Melting (EBM)</i>	Electron beam	Metal particles fusing	1. Metal alloys.	Diameter x Height 13.78"x14.96"	1. High volume productivity. 2. Low cost. 3. Suitable for complex medical implants. 4. Good for light-weight components. 5. No support structure needed.	1. Limited build volume. 2. Residual stress due to vacuum environment. 3. Oxidation due to vacuum environment. 4. Exclusively used in metals.	[32] [33] [34]

Table 2 - 3D printing literature survey summary of various techniques' advantages and disadvantages

1.4 Proposed Method

The curing methodology developed for the first time in the context of electronics metal contacts in this thesis was inspired by recent advances in fiber optics integration. The objective of this investigation was to develop a low temperature ($\ll 150^\circ\text{C}$) silver ink curing process using a programmable controlled-dose pulsed-light source originally developed for automated fiber placement, the Heraeus Humm3[®] System (H3S). The system uses flash lamp sources which are comparable to lasers in terms of power but allows better control of programmed energy delivery profiles. Precise control can be achieved using energy, duration, and pulse repetition frequency. The apparatus is sufficiently agile for focusing heating on target areas which ensures proper material uniformity after annealing [36]. Compared with wave infrared (IR) heat guns or laser illumination, the broadband (UV to IR) energy transfer results in better adhesion for the printed tracks as well as highly uniform films [37]. Again, the H3S has performed favorably against both these methods for fiber placement as well so it was anticipated that this would provide a reasonable alternative for electronics. None of the previous studies of which we are aware have involved the curing of conductive layers, which has been developed during this thesis research.

To assess our process, we take recent advances in laser sintering as a benchmark, which resulted in silver conductivity values of 26% that of bulk Ag in a process compatible with paper substrates [38]. We chose this measure because the conductivity is an appreciable fraction of the bulk silver value, indicative of results most often seen when the silver NP ink is held at 150°C or higher. This sharp conductivity improvement threshold crossing through 150°C has been well-documented, see, e.g., the temperature dependence shown in [39]. The goal of this thesis is to answer two main questions. One is whether the low temperature optical curing process results in conductivity values similar to the state-of-the-art for printed silver ink that has been commonly

processed with thermal curing. The second is to understand that if reasonable conductivity values are repeatedly observed, what is the microstructure and material composition as obtained through microscopy and chemical analysis. Both of these objectives were fulfilled and are elaborated in this thesis.

The results of this research demonstrate the light-pulse curing process on AJP deposited silver ink as a function of the thickness of the metal under curing conditions that achieve controlled temperatures of 35°C for time intervals from 20 to 30 minutes and 100°C for 50 minutes. The measured conductivity is compared to that of bulk silver and the material uniformity was investigated and documented using cross-sectional scanning electron microscopy (SEM). This curing process demonstrates that the silver NP ink material can be cured at very low thermal budgets and result in conductive features practical for electronics. This method accurately demonstrates the potential of using the H3S or equivalent broadband light source as a new approach for fast, low temperature annealing for metal NP conductive inks.

1.5 Dissertation Organization

This thesis is organized along the following lines with the common theme of my research progression from rudimentary 3D printing to the execution and results of the work outlined in Section 1.4.

Chapter 2 demonstrates important elements of the experimental fabrication and characterization techniques used in this research. Those elements are provided to clarify the conditions for reproducibility for each contribution in the subsequent chapters.

Chapter 3 presents my early graduate studies' work on the design, 3D printing, and electronic circuit assembly for a maple-seed robotic flyer (MRF). The main goal of this work was a Michigan State University (MSU) / Electrical and Computer Engineering Department initiative

to introduce 3D printing concepts to Kindergarten-12 (K-12) students, first year engineering students at MSU as well as summer camp participants through the diversity program office (DPO) at MSU in order to gauge the student's interest in the science, technology, engineering and mathematics (STEM) concepts. The other goal was to print the circuit metal traces on the rib side of the MRF and attach the electronic components using conductive glue and check the resulting MRF performance. Another aspect of producing MRFs was microfabrication which can increase the repeatability, enable multiple MRF sizes and produce high quantities. Microfabrication of MRFs may be part of future work as discussed in Chapter 6. This chapter also demonstrates my work on the design and 3D printing of an optical cavity that receives violet/blue light from a 405nm/445nm laser and emits visible light using a single aperture. The other goal of this work was to print the highly reflective mirror in the optical cavity using aluminum NP ink and characterize the cavity performance. This work could be part of future work as discussed in Chapter 6.

Chapter 4 focuses on my initial work on experimenting with AJP metal printing. I utilized the Optomec Aerosol Jet® 5X for the 3D printing of silver ink with the idea of using published structures as a guide to understand annealing conditions that would result in useable metal structures for radio frequency (RF) applications. The idea was to create CAD files replicating the three types of transmission lines that were presented in [40], cure them on a hot plate at temperatures between 160°C to 200°C for 20 minutes, measure the material conductivity, test the fabricated lines in terms of thickness, sizes, and measure the RF scattering parameters. The goal was to gauge if the transmission line material would be sufficiently conductive if sintered for short periods of time using a hot plate. The fact that this method did not produce high quality results was a motivation for seeking alternative curing methods later in my research. This chapter also demonstrates my work on aerosol jet printing on glass substrates as well as flexible substrates for

wearable and flexible electronic devices. My contribution to a collaboration among several MSU engineers included silver ink printing on glass substrates and liquid crystal polymer (LCP) / Kapton foils, curing the devices on a hot plate, and measuring RF scattering parameters. This published work proves that we were able to reach 70% of bulk silver conductivity using a hot plate as the curing method for long sintering times (~16 hours) and temperatures between 150°C and 200°C. Despite the fact that we reached high metal conductivity using this method, the conditions were clearly not suitable to cure the contacts of devices with organic materials. Overcoming this challenge became the final focus of my dissertation research.

Chapter 5 shows the use of the H3S optical pulse technology to sinter the printed metal contacts that could be used for OLED and TPV contacts, and well within thermal tolerances. This measured data in Chapter 5 shows that the AJP silver ink contacts can achieve 17% of bulk silver conductivity with 20 to 30 minutes of curing time at 35°C, which makes the broadband light sources a good candidate for curing the contacts of OLED and TPV devices that can handle up to 150°C for shorter periods of time without degrading the organic material. We also analyzed the stored silver thin films in terms of grain size measurement as well as atomic percent silver oxide chemistries using SEM.

Lastly, Chapter 6 discusses the conclusion and future work of this thesis.

CHAPTER 2: EXPERIMENTAL TECHNIQUES

Key elements of the experimental fabrication and characterization techniques used in this thesis research are provided to clarify the conditions for reproducibility for each contribution in the subsequent chapters.

Section 2.1 describes the Objet Connex350™ printer functionality and the type of material that was used to produce the MRF in section 3.2. Section 2.2 discusses the Optomec Aerosol Jet® 5X printing methodology and the deployment of that technology to 3D print the silver ink tracks presented in Chapter 4 and Chapter 5. Section 2.3 clarifies the use of a hot plate to thermally cure the silver ink films in Chapter 4 and the H3S system to optically cure the silver ink NP contacts in Chapter 5. Section 2.4 presents the conductivity measurement using a Pro-4 system as well as the RF transmission lines losses using Agilent network analyzer. These measurements were carried out as described in Chapter 4 and Chapter 5. Section 2.5 discusses the physical and materials properties in terms of material thickness using NanoMap 500LS, thermogravimetric analysis (TGA) using TA Instruments TGA Q500, scanning electron microscopy using JEOL JSM 7500F and grain size measurements using the NIH ImageJ package. These measurements and analysis appear in Chapter 4 and Chapter 5.

2.1 3D Printing - General Purpose

This section provides a brief description of the 3D printer, material and design file software for my early work experimenting with 3D printing techniques.

2.1.1 Objet Connex350™ Printer

The Objet Connex350™ printer has the ability to print multiple parts simultaneously through jet heads. The system is capable of printing parts and assemblies from different materials and colors as a single build. The printer utilizes Objet PolyJet Matrix™ Technology to print digital

materials; this concept allows to print certain Shore A values “Hardness Scale Measure” [41] to match the values of the intended production materials. This approach allows for quick prototyping including testing and molding process simulation [42]. Figure 1 shows the Objet Connex350™ printer (a) and the printer parts (b).

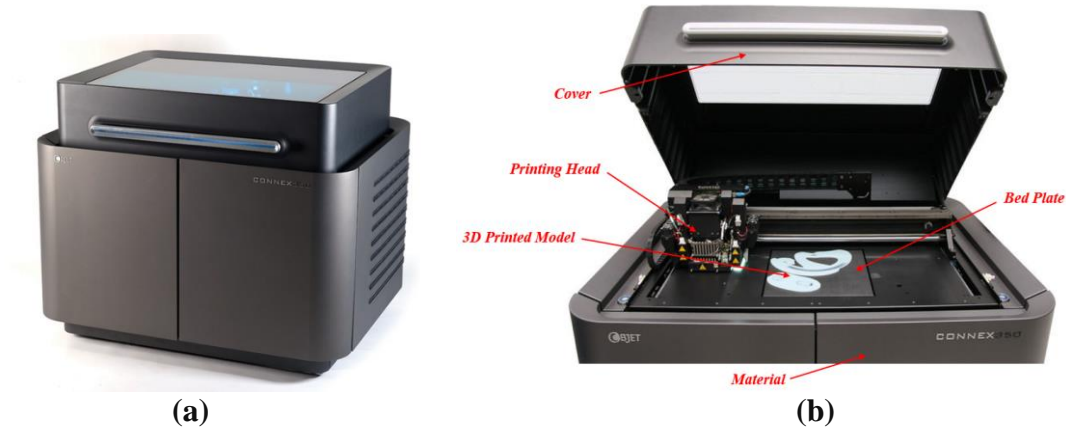


Figure 1 - (a) Objet Connex350™ printer (b) Printer parts
(Images (a) and (b) reproduced with permission from [43].)

2.1.2 Ink - 3D Printing Material

We used VeroWhite Plus as the 3D printing material for the MRF and the optical cavity. VeroWhite Plus is a resin material (Opaque PolyJet Resin) that is capable of forming 3D models from a base of photosensitive polymer liquid. UV light is used to solidify the liquid one layer at a time to form the final product. VeroWhite Plus is used to make smooth and precise 3D objects for prototyping purposes [44]. VeroWhite Plus physical properties are shown in Table 3 as collected from [45].

Mechanical Properties	Metric
Color/Appearance	White
Tensile Strength	58 MPa
Elongation at Break	10%-25%
Modulus of Elasticity	2500 MPa
Flexural Strength	93 MPa
Izod Notched Impact	25 J/m
Shore D Hardness	85 D
Heat Deflection Temperature	48°C

Table 3 - VeroWhite Plus physical properties

2.1.3 Design File Requirement

The Objet Connex350TM printer utilizes Objet StudioTM software to generate the proper file that can be read by the printer. The software has the following features [42]:

- Simplicity in material selection.
- Easy separation of parts into sub-assemblies.
- Slicing of the file on the go.
- Automatic parts placing on the bed plate.
- Real time structure support creation.

The 3D model can be designed using any CAD software and then converted into Standard Tessellation Language (STL), Stereolithography Contour (SLC) or objDF file so the printer can interpret easily. According to Stratasys [46], “An objDF file describes both the geometry of a single object, the materials and finish required to print it. The objDF file can represent an object that is a single STL file, or an object assembled from component STL files”. STL means encoding the surface geometry of the object in some sort of tiles fashion like triangles and store the information about these triangular geometries. Information can be stored in two ways: American

Standard Code for Information Interchange (ASCII) encoding and binary encoding. According to Sculpteo [47], “Both types save the components of the unit normal vector to the triangle and the coordinates of the vertices”. Figure 2 shows (a) a 3D part in STL format and depicts the two types of STL formats, ASCII format (b) and binary format (c) [48].

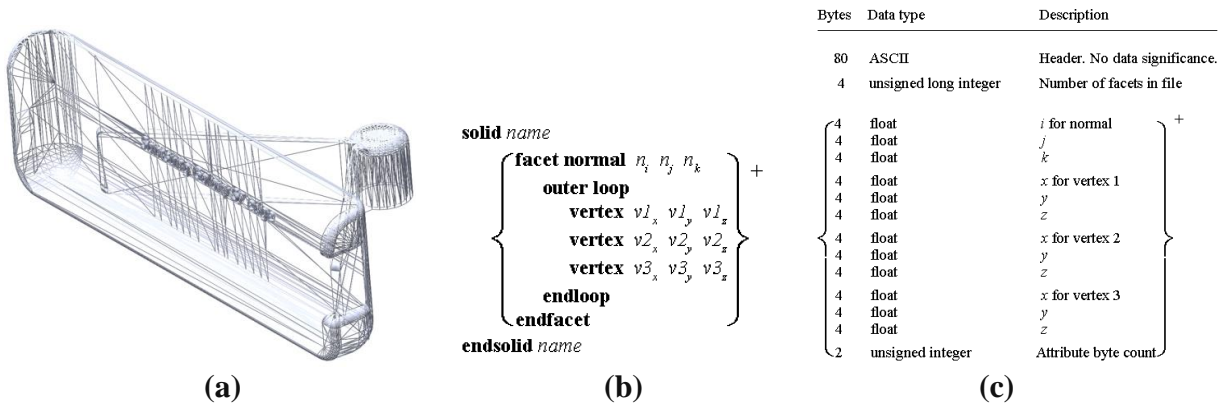


Figure 2 - (a) 3D part in STL format, (b) ASCII file format, and (c) Binary file format
(Images (b) and (c) reproduced with permission from Automated Fabrication by Marshall Burns [48].)

2.2 3D Printing - Metallic Silver for Electronic Applications

This section provides a brief description of the metallic 3D printer, silver ink and design file requirement for my work on metal inkjet printing.

2.2.1 Optomec Aerosol Jet® 5X Printer

The Aerosol Jet process focuses the deposition of the ink on the substrate using aerodynamics. The atomizer holds the ink, then it creates a dense mist of material droplets ranging from 1 to 5 microns in diameter. The mist is injected into the deposition head and is focused by sheath gas that surrounds aerosol mist as an annular ring. As the sheath gas and aerosol combine in the nozzle, they accelerate and the mist becomes a tight stream of droplets flowing inside the sheath gas. The sheath gas serves the purpose of preventing the material clogging in the nozzle. Dry Nitrogen or compressed gas are the two gas choices for the system. Maintaining a distance of

2 to 5 mm over the substrate will guarantee focused stream with high velocity for better material resolution [49]. Figure 3 shows the Optomec Aerosol Jet® 5X printer (a) and the printer parts (b).

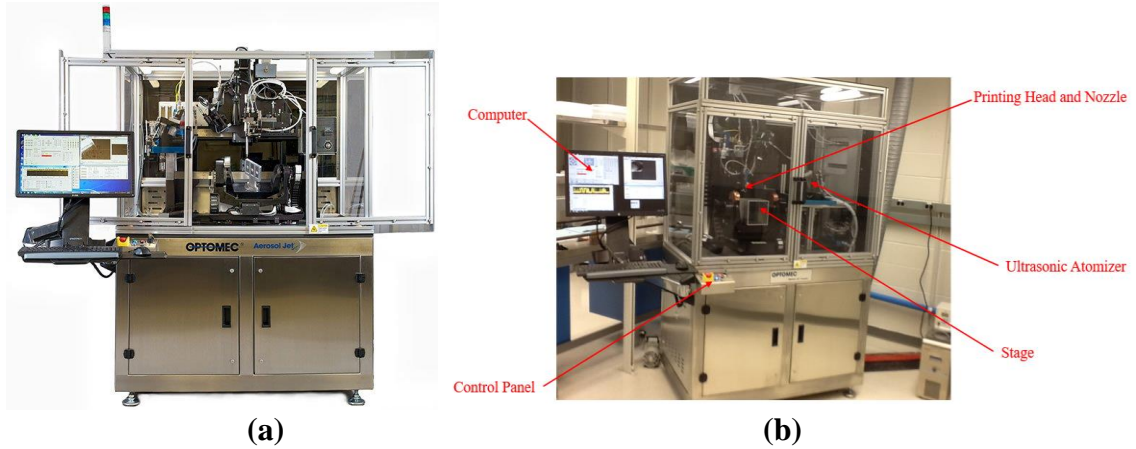


Figure 3 - (a) Aerosol Jet 5X printer (b) Printer parts

(Image (a) reproduced with permission from [50] and image (b) reproduced with permission from [51].)

2.2.2 Clariant EXPT Prelect TPS 50G2 Silver Ink

The TPS 50G2 silver ink is a mixture of silver colloid, CAS No. 7440-22-4, concentration 30-50 %w/W and Ethenediol (Ethylene Glycol), CAS No. 107-21-1, concentration 10-20 %w/W. Density is ca. 1.74 g/cm³ at 20°C. Decomposition temperature is ca. 350°C. The ink viscosity is ca. 25 mPas.s at 23°C [52]. The recommended solvents used with this ink are deionized (DI) water or Ethylene glycol. The dilution ratio is 1:1, ink: DI water at ambient temperature [53].

2.2.3 Design File Requirement

The printer is controlled using CAD data which is translated into a vector-based tool path. This tool permits ink patterning through the two-dimensional (2D) or 3D motion control system [49]. The 2D pattern of silver ink can be designed using CAD software such as AutoCAD® or SolidWorks® and the file can be saved as Document EXchange Format (DXF) file. VMTTools™ is a utility converts the DXF file into a toolpath (PRG) file that can be read by the Aerosol Jet Workstation Control (KEWA™) Software. The toolpath generates commands that drive the printer during the deposition process to build the desired pattern. The toolpath allows the operator to

define the outer edges of an object and then fill the inner area with the material [54]. Figure 4 shows KEWA™ software during the printing process.

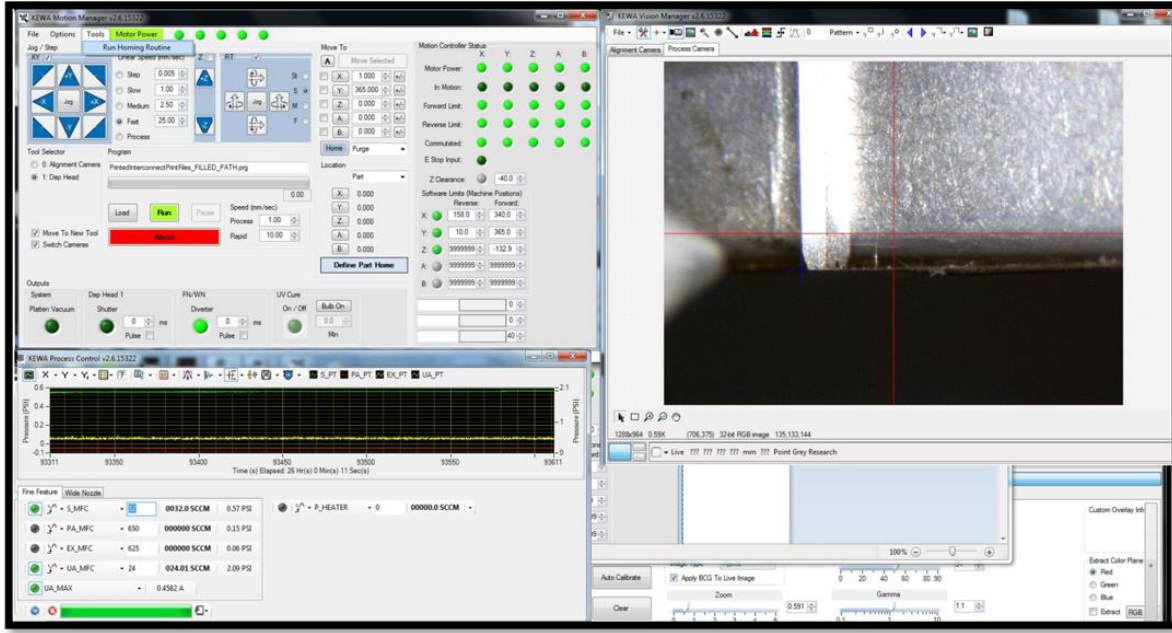


Figure 4 - KEWA™ motion manager software

2.3 3D Printing - Curing Techniques

This section provides a brief description of the curing techniques we used for sintering the printed metal ink.

2.3.1 Hot Plate

We initially utilized IKA hot plate, model number C-MAG HS 7. The system is equipped with magnetic stirrer and chemical resistance ceramic heating plate. Heating temperature is 50-500°C with a turning knob for heat control.

2.3.2 H3S Basics

Use of the H3S was central to the original work performed in this thesis. Its combination of features offered a new and fundamentally unexplored approach for overcoming the temperature incompatibility of metal ink curing by hot plate or laser sintering with polymeric structures that require low-temperature processing. The H3S offers optimal heating for automated fiber

placement (AFP), a flexible, controllable heat solution for rapid lay-up of thermosets, dry fiber and thermoplastics, with three programmable parameters. With sophisticated control, the pulsed light source can be used to deliver uniform, highly controllable heat to target area, over a wide range of temperatures [55].

The H3S controls the heat profile using 3 programmable pulse parameters [55]:

- Pulse Energy - where the system maintains equal time interval between pulses while changing pulse energy level; i.e. 3 pulses (low energy) followed by 3 pulses (high energy “2 x low energy level”).
- Pulse Duration - where the system maintains same energy level but changes the pulse duration; i.e. shorter pulse time for the first 3 pulses (low pulse duration) followed by longer pulse time for the next 3 pulses (high pulse duration).
- Pulse Frequency - where the system maintains same energy level but changes the pulse frequency; i.e. shorter pulse frequency for the first 3 pulses (low pulse frequency) followed by longer pulse frequency for the next 3 pulses (high pulse frequency).

Normal operation is at more than 50Hz, at this frequency the human eye sees a continuous light source. Figure 5 shows (a) the H3S and (b) the system components.

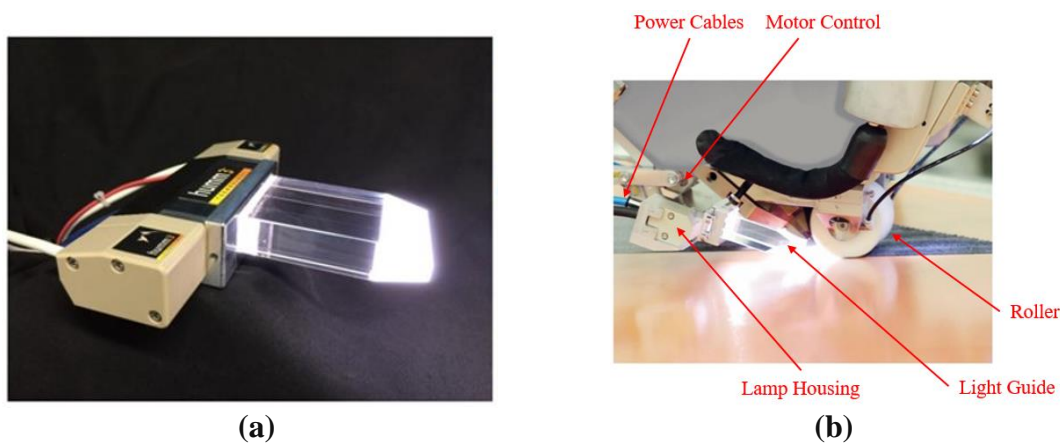


Figure 5 - (a) H3S and (b) System components
(Images reproduced with permission from [56].)

Some of the H3S advantages for this application include [55]:

- Fast heat/cool, there is no residual lamp heat.
- Heat time and temperature are equivalent to laser systems.
- Small responsive head for difficult bends.
- High level system with 3-parameter heat profile.
- Fast response control system to AFP head speed.
- Heat zone size is adjustable.
- No enclosure required as the system is built with enhanced safety.

2.4 3D Printed Electronics - Electronic Properties Characterization

This section provides a brief description of the systems we used to measure the silver ink DC conductivity and transmission line losses at RF frequencies.

2.4.1 Conductivity

Lucas Labs Pro-4 Four Point Resistivity System, model - Signatone QuadPro Resistivity System Pro4-440N with Keithley® 2400 sourcemeter (supply and measure current-voltage in one instrument) [57] and Head model - SP4-62180TFS (62.5mil (0.15875cm) spacing between tips, 180 gram spring pressure, Tungsten Carbide, 5mil radius tip with standard flying lead termination, 15inch wire) [58] were used to measure resistivity. Samples conductivity was calculated as the inverse of resistivity. Figure 6 shows Pro4-440N configuration (a) probe separation distance (b) and measurement result display (c).

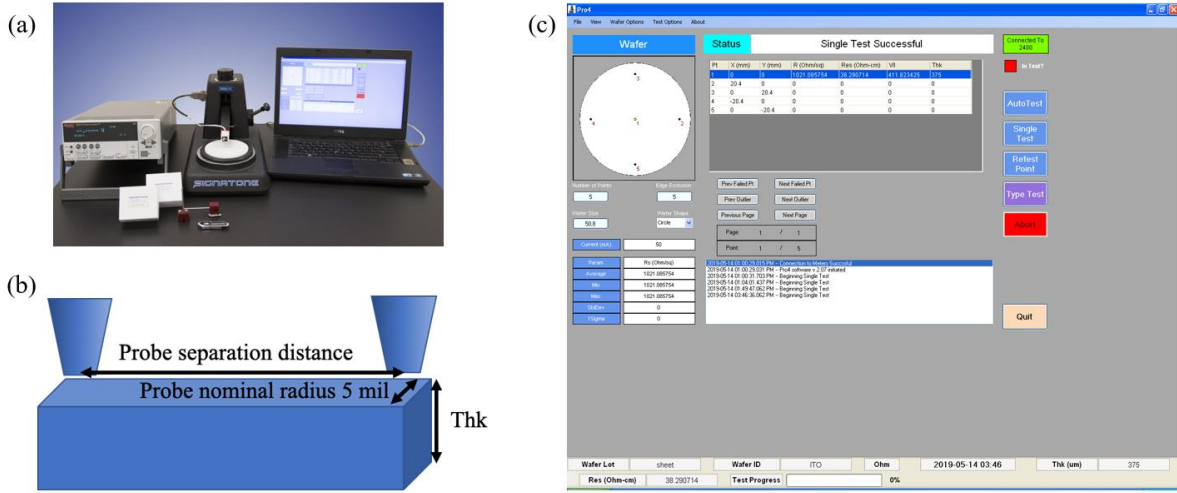


Figure 6 - (a) Pro4-440N configuration (b) Probe separation distance (c) Measurement result display

(Image (a) reproduced with permission from [57].)

2.4.2 Transmission Line Measurements

Agilent N5227A PNA Network Analyzer (for 10MHz - 67 GHz) [59] and VDI WR10-VNAX extension modules (for 75 - 110 GHz) [60] were used to measure the losses of standard transmission lines at RF frequencies.

2.5 3D Printed Electronics - Physical and Materials Properties Characterization

This section provides a brief description of the systems we used to measure material thickness, determine silver ink contents after curing and check thin film uniformity.

2.5.1 Surface Profiler

AEP Technology, Model - NanoMap 500LS 3D Contact Stylus Surface Profilometer (2μm diamond stylus tip) was used to measure the material thickness. The profilometer provides the raw data and using the software functions we were able to measure the roughness as R_a value (calculated as the roughness average of the surfaces measured microscopic peaks and valleys). The system has wide vertical range with high accuracy as a result of the dual optical sensor design, up to 500μm vertical range with coarse sensor and up to 0.1nm vertical resolution with fine sensor [61]. Figure 7 shows the NanoMap 500LS profilometer (a) and a silver ink sample under test (b).

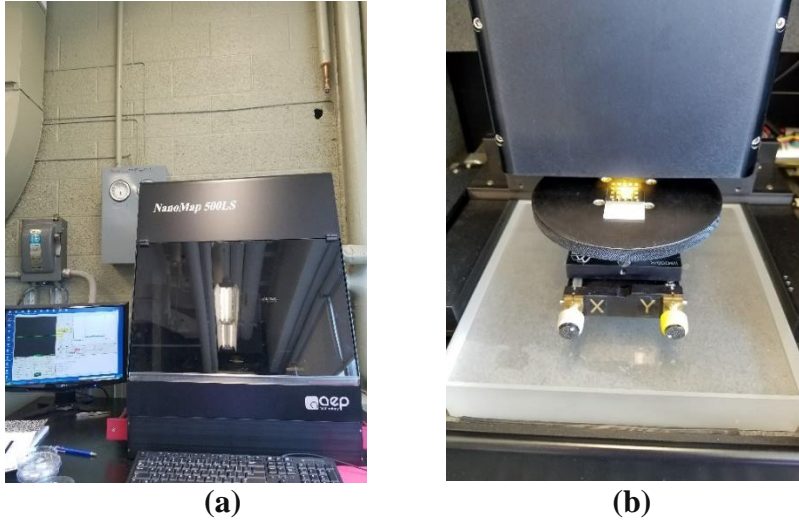


Figure 7 - (a) NanoMap 500LS profilometer (b) Silver ink sample under test

2.5.2 Thermogravimetric Analysis

TA Instruments TGA Q500 was used to conduct the thermal weight-change analysis for the inkjet-printed silver ink on glass substrate. The TGA Q500 is able to heat the sample under test up to 1000°C. The high-resolution feature offers precise temperature [62]. The system is equipped with two mass flow controllers to purge the gas and balance furnace temperature [63]. Figure 8 shows TA TGA Q500 thermogravimetric analyzer.



Figure 8 - TA TGA Q500 thermogravimetric analyzer
(Image ©2020 TA Instruments/Waters Corporation reproduced with permission from [64].)

2.5.3 Scanning Electron Microscope

The JEOL JSM 7500F was used to study the physical basis of the silver ink-based film and transmission line electronic performance. A nanocrystalline silver morphology was consistently demonstrated, whose uniformity, grain size, and stoichiometry were assessed using secondary electron imaging (SEI), low-angle backscattered electron (LBE) imaging and x-ray energy dispersive spectroscopy (EDS). The JEOL JSM 7500F with a cold field emission emitter at the Center for Advanced Microscopy, Michigan State University is designed for the demanding applications in the range of 1,000X to 1,000,000X. It is the highest resolution SEM in the State of Michigan. The 7500F is designed for maximum resolution and information extraction by use of multiple advanced secondary and backscattered electron detectors, a special energy filter for the detected electrons, and electron beam deceleration [65] [66]. Figure 9 shows JEOL JSM-7500F field emission SEM system (a) and cold cathode FE SEM column cross section (b).

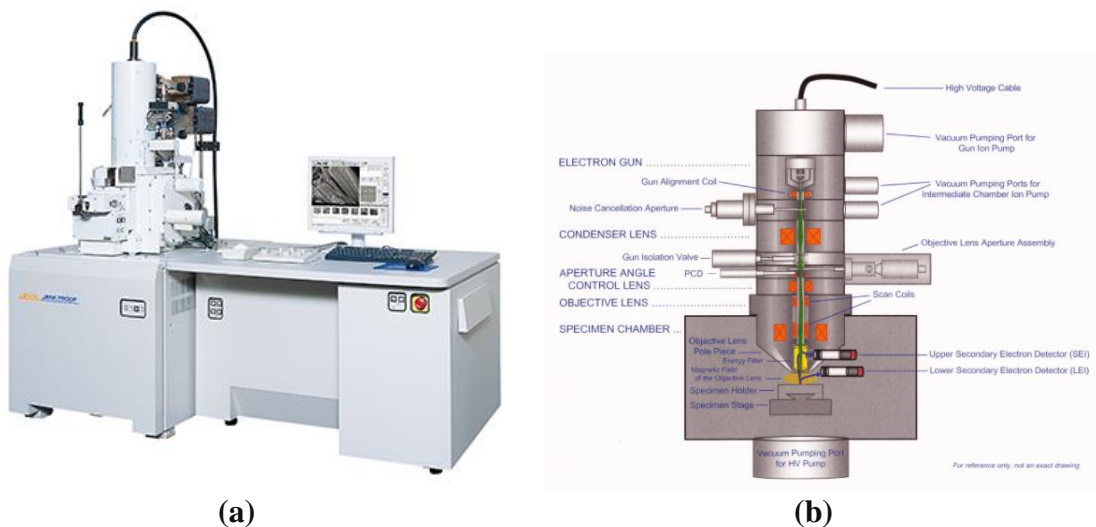


Figure 9 - (a) JEOL JSM-7500F field emission SEM system (b) JEOL cold cathode FE SEM column cross section

(Images reproduced with permission from [65], Credit: JEOL USA.)

JEOL JSM-7500F comes with a built-in R-filter allows for freely selection of secondary electrons and backscattered electrons by maintaining location of the incident electrons on the

center of the electron optics. When a beam of electrons strikes a sample, a variety of electrons are produced due to elastic and inelastic scatter. Figure 10 shows the R-filter (a) spectrum (b). The low energy peak on the left is the secondary electrons and the high energy peak on the right is the backscattered electrons. There are a number of electrons that fall outside the peaks (Auger electrons, Plasmon losses, etc.). The R-filter consists of 4 electrodes. By varying the polarity and magnitude of the voltages on the electrodes, you can filter the energy level of the electrons that make it to the upper detector. The R-filter allow you to mix the signals for secondary and backscattered electrons. The greatest use of this filter is on samples that have a slight amount of charging. The "charging" secondary electrons often have a slightly higher energy than do the non-charging secondary electrons. By carefully adjusting the filter, you can exclude these high energy secondary electrons and in some cases remove the charging artifacts [67].

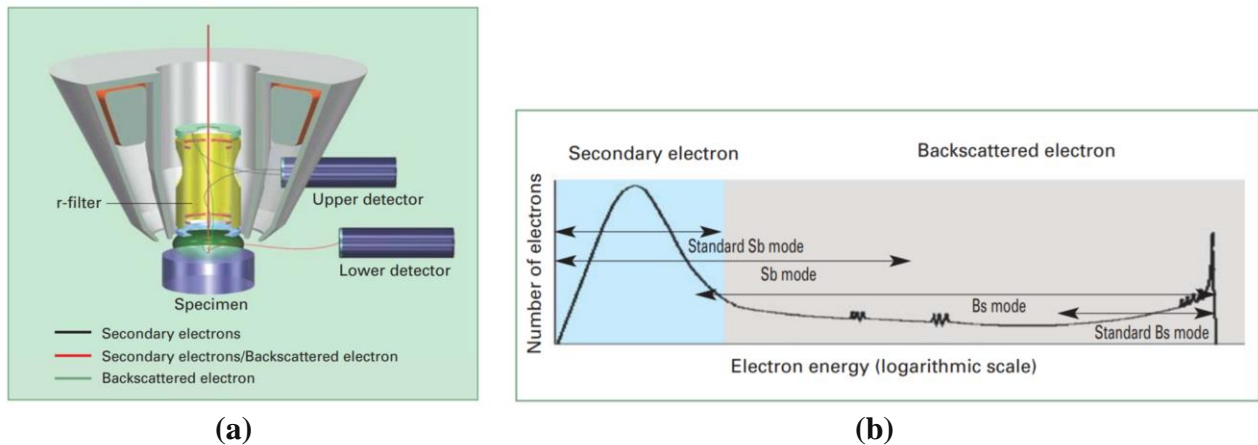


Figure 10 - (a) R-filter selectively detects secondary and backscattered electrons (b) Energy ranges selected by the R-filter

(Images (a) and (b) reproduced with permission from [67], Credit: JEOL USA.)

2.5.4 Grain Size Measurement

NIH ImageJ package was used to measure the grain sizes in the SEM images. ImageJ is an open source Java image processing and analysis program. The software can be used directly as an online applet or can be downloaded on Windows, Apple or Linux operating systems. The software

can read multiple image formats such as Tagged Image File Format (TIFF), Graphics Interchange Format (GIF), Joint Photographic Experts Group (JPEG), Bitmap (BMP), Digital Imaging and Communications in Medicine (DICOM) and Flexible Image Transport System (FITS). The software is able to calculate specific area and pixel value. It measures angles and distances. It also comes with other features such as contrast manipulation, sharpening, smoothing, edge detection and median filtering [68].

CHAPTER 3: 3D PRINTED COMPONENTS AND APPLICATIONS

3.1 Overview

This section demonstrates my early work on the design, 3D print and electronic circuit assembly for a MRF that led to a publication with the Journal of Education and Training Studies - Red Fame [69] and for the design, 3D print and tests of a laser optical cavity that resolves a significant problem with LED projectors in a cost-effective manner, this work led to a publication with The Society for Information Display (SID) [70].

3.2 3D Printing for Education, Research and Entrepreneurship

There have been many advances in man-made robots and nature-made systems that intrigued many researchers to build new concepts that could serve many objectives for educators in the outreach and STEM programs [69]. Robots expanded into many applications that serve humanity such as humanoid robotic dolls for children with autistic disorder and dance partner [71] [72] autonomous underwater robots for marine applications [73] as well as robots searching for life on Mars [74]. Some researchers deployed LEGO® MINDSTORMS® as part of the first-year curriculum for college students [75].

3.2.1 Maple-seed Robotic Flyer

Engineering systems that were inspired by nature have been deployed in multiple areas of great interest to education, technology and outreach programs. Pertinent to this work, controlled and non-controlled robotic fliers based on the flying concepts exhibited by of nature-made maple seeds have been recently demonstrated [69] [76] - [81]. STEM programs benefit greatly from the deployment of the man-made fliers as they focus and encourage critical thinking and inquiry approaches among students [82].

As shown in Figure 11, MRFs have been designed, fabricated and tested to enhance the learning knowledge of the pre-K children, free-will adult learners, underrepresented areas, undergraduate and graduate students. The concepts are designed for research-oriented educational purposes, entrepreneurship education and cross-functional research. The models of learning introduced through the MRF generations are innovative and can increase the students' interest in engaging in one of the STEM programs. Robotics have been used in trans-disciplinary programs like mathematics, electronics, chemistry, computer science and material science [83].

Our work focused on using the MRF to teach STEM concepts (weight-carrying capacity, revolutions per minute (RPM), blinking light emitting diode (LED), acceleration, sensing...etc.) to K-12 students and also incorporating the concepts in undergraduate engineering course for first year students in the college of engineering at Michigan State University. Inkjet-printed MRFs vary from simple (1-wing) to (2-wings) to complex (4-wings) that can carry electronic circuit assembly (sensors, LEDs, wireless interface, global positioning system (GPS) and battery) [69].

3.2.2 3D Inkjet-Printed MRF

We explored the 4-wing inkjet-printed MRF by adding different design options related to wireless interfaces, sensors, energy sources (battery vs capacitor) as well as using different packaging. The study of different types of MRF opens the door for mass production, starting with inkjet-printing of a complete MRF system; i.e. placeholders for control electronics, sensors, and a battery. Objet Connex350™; a commercial inkjet printer allows different plastic materials like VeroWhite Plus to be used. Design of MRFs with 1-wing (a) and 4-wings (b) are shown in Figure 11 [69].

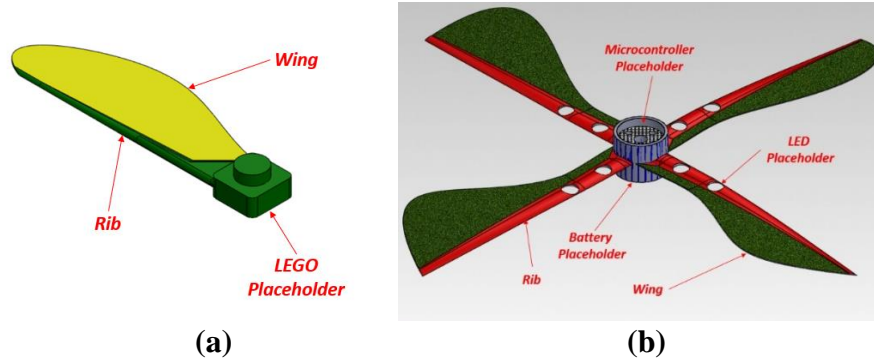


Figure 11 - Design of MRFs with (a) 1-wing (b) 4-wings

The major goal of the 4-wings MRF design is to collect, store, and use data from the nearby atmosphere. The information will be stored in memory and can be transmitted over wireless fidelity (WiFi) network to a central location for analysis. The current version of the 4-wing was built with a temperature sensor and a three-axis acceleration sensor for RPM measurements [84] [85], speed of wind, time of flight, atmosphere temperature, along with other parameters. The development of MRF with its simple to extremely complex learning disciplines led to modules and designs that can be deployed for humanitarian applications in natural disasters areas, i.e. detecting wild fires direction spread. The idea of utilizing the MRF was adopted by the University of Michigan in collaboration with Michigan State University to study tornados. We are one of the first research groups at Michigan State University to publish journal articles utilizing Objet Connex350 printer. The concept of MRF was taught in outreach programs for underrepresented students at the Information Technology Empowerment Center (ITEC) in Lansing, Michigan along with the summer camps of the DPO at MSU and Dr. Dean Asalm's summer camps [69].

3.2.3 3D Print Material

We utilized Objet Connex 350 printer to print the MRF structure (wing and rib) using VeroWhitePlus material. The material is rigid, durable and heat resistance. The material can be used for general purpose applications due to its high resolution and opaque white color. VeroWhite

Plus has great properties especially if used with the PolyJet process, so models that are produced with this material will have smooth contour surfaces that require less post production cleaning [86] [45].

3.2.4 Learners Evaluation

Questionnaire forms have been used to evaluate the learner's experience. It was noticeable that the college level students were able to digest most of the concepts that were taught during the lab. MRF lab learners were broken down into two groups, lab year 1 and lab year 2. The flow of activities coupled with the experiment's design are very important for the learner experience. It was noted that well-developed lab experiments that has detailed instructions along with clear goals helped in completing the activities in a timely manner. The learning lab questionnaire results are summarized in Table 4 [69].

No.	Question											Average Score Lab Year 1	Average Score Lab Year 2
	Not Satisfied	1	2	3	4	5	6	7	8	9	10 Satisfied		
1.	This experiment was a good learning experience for me											8.35	7.25
2.	My interest in this experience											8.91	7.47
3.	The laboratory experiences are well-designed											8.79	8.29
4.	Overall rating of experiment											8.90	8.01
5.	Innovation and fun in the experiment											-	8.12

Table 4 - Learning lab questionnaire results
(Table reproduced with permission from [69].)

The feedback from the lab learners came back positive as the average response for each question asked scored over 8 as noted above. The interest was very high among the K-12 learners as the lab experiments excited their interest and most of them were very engaged. Overall, the MRF experiments have valuable techniques that can catch the student's interest and get him motivated even to further enhance the experiment itself and make the MRF unique. The team work among the students generated a positive and collaborative environment that will become part for the team work mindset in the future [69].

3.2.5 Conclusion

We successfully developed a passive MRF that was equipped with sensory electronics for the purpose of engaging K-12 students as well as college students at MSU into STEM concepts. The learners showed great interest in learning the concepts proposed through the MRF experiment and also led to a fun and collaborative team work among the participants. Since we were successful in building the first prototype using off the shelf electronic component, the research will continue in the future to utilize microfabrication techniques to mass produce the MRF with different sizes and different application purposes. Some future applications could be in humanitarian application for fighting fires as well as the deployment in tornados to study their formation and behavior [69].

It is feasible to inkjet print silver as the conductive tracks on the rib side of the MRF and cure the tracks using pulsed light system. The H3S system has the ability to cure the conductive tracks at low temperature that doesn't damage or deform the MRF rib structure. Electronic components can then be attached to the rib side using conductive glue. Microfabrication is another approach that can be used to mass produce MRFs. This topic will be discussed further in Chapter 6 as a future work.

3.3 Phosphor-based Optical Cavity

We utilized a low-cost commercially available laser to generate visible light for etendue-limited applications. The major component in the design is a phosphor-based optical cavity that receives a 405nm/445nm laser light and converts it into speckle-free green light at a selected etendue [70].

3.3.1 History and Goal

Despite the fact that LEDs as a visible light source provide better power efficiency and have longer lifetime comparing to lamps, they still suffer the high etendue problem that make them

unsuitable for specific projection applications [87]. Commercially available lasers and lamps are also not the right choice in terms of cost and performance for mobile applications [88]. The main goal of this work was to build a compact laser-driven solid-state light source that can be used for etendue-limited application like a pico-projector. In the current market, LEDs and visible lasers are the common light sources for pico-projectors. Nonetheless, lasers are costly, and LEDs have high etendue values that lead to limited screen brightness. Hence, there is unmet need for a solid-state light source that can be built with a reasonable cost and meet the desired performance of pico-projectors [70] as well as the ability to be embedded into portable devices [89]. In 2009, Samsung reported speckle suppression for red, green and blue (RGB) using coherent beams in the pico-projection system [90]. In 2010, Casio developed a similar concept using a hybrid light source, they used red and blue LEDs joined with a 445nm laser that is capable of exciting a green phosphor layer on a rotating wheel generating green light. Casio system is capable of providing a screen brightness between 1,000 lm to 3,500 lm [91]. In 2014, Abu-Ageel *et al.* [92] reported a high-power laser-driven light source that uses an array of 445nm violet lasers coupled with an optical cavity that generates visible light for specific applications similar to cinema projectors [92]. Moreover, other companies such as Panasonic Corporation utilized 405nm lasers to build a high-power light source that can excite RGB phosphor layers that are deposited on a rotating wheel and capable of producing 60W of RGB light utilizing 405nm lasers [93].

Overall, this work shows the development of a condensed visible solid-state light source that is capable of providing sufficient light at a selected etendue for pico-projection uses [70].

3.3.2 Optical Cavity Design

The major part in the proposed solution is a phosphor-based optical cavity that accepts violet/blue light from a $405\text{nm} \pm 5\text{nm}$ laser and releases visible light using a solo slit. The received

light is reprocessed inside the cavity until it is completely immersed by the phosphor layer and then re-radiated as visible light at the selected wavelength. Figure 12 shows a cylindrical cavity that entails a straight solid light guide (SSLG) with its top surface coated with a highly reflective mirror except the slit which will receive violet laser light and transfer it into visible light, a phosphor layer printed over a highly reflective mirror at the bottom side of the SSLG, and heat dissipation during the light conversion process will be handled using a heat sink attached to the mirror. The purpose of having the air gap between bottom side of the SSLG and phosphor layer is to ensure that Lambertian light emitted from the phosphor is driven within the SSLG through total internal reflection at its non-coated sidewalls [70].

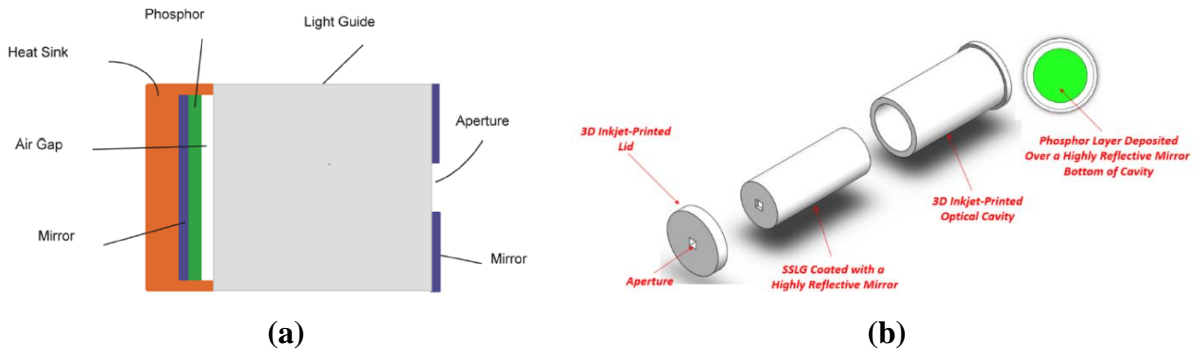


Figure 12 - (a) Cross-sectional view and (b) 3D design of the optical cavity
(Image (a) reproduced with permission from [70].)

The cavity will convert the violet/blue laser light that is received through the cavity slit into visible light through the deposited phosphor layer. As the SSLG directs the light toward the cavity slit, the phosphor layer will absorb some of the coherent laser light and allowing incoherent visible light transmission. The type of phosphor material that is used for deposition on the cavity walls will determine the converted light wavelength. The residual laser light exits the phosphor layer as violet/blue light. All light, whether it is converted or non-converted will be directed toward the top side of the cavity. As the light strikes the top side of the cavity, a small amount of that light will be sent through the slit and the rest will be reflected back toward the phosphor layer by the top

side's mirror. Carefully designed cavity will allow a large portion of violet/blue laser to be converted into visible light. This process endures until a large portion of the converted light leaves the cavity through its slit. As for the cavity optical efficiency and etendue of converted light, this depends totally on the aperture size relative to the cross-sectional area of the SSLG. The optical efficiency of the cavity and etendue of converted light depend on the size of the aperture relative to the cross-sectional area of the SSLG [70]. Figure 12(b) represents the 3D design of the optical cavity.

The 3D printed cavity was used in the system assembly shown in Figure 13(a), the assembly illustrates the light source prototype with a green cavity. The dichroic mirror reflects the green light and passes the focused blue beam from the laser array into the cavity [92]. Figure 13(b) demonstrates the light source assembly during operation [92].

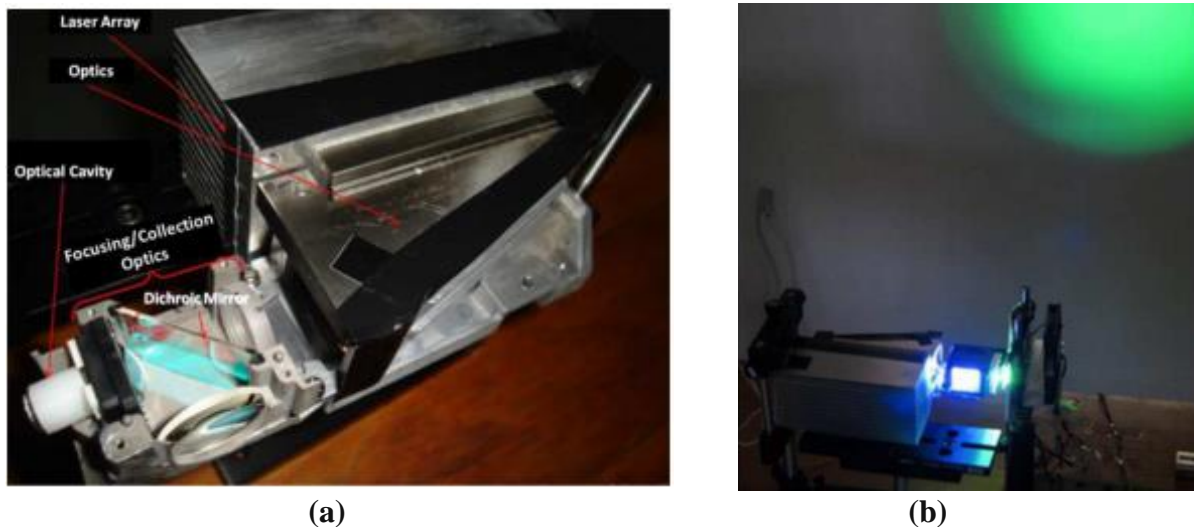


Figure 13 - Light source (a) prototype with a green light optical cavity and (b) assembly during operation

(Images reproduced with permission from [92].)

3.3.3 System Design using Collimating and Focusing Lenses

The suggested light source comprises a violet/blue laser, a collimating lens (Figure 14(a)) or focusing lens (Figure 14(b)) for the laser beam, a dichroic prism that reflects the laser beam and reflects back the converted light, a conical light guide to couple the input/output light and the

optical cavity. Silicone gel can be used between the slit of the SSLG and the conical light guide as an index matching material [70].

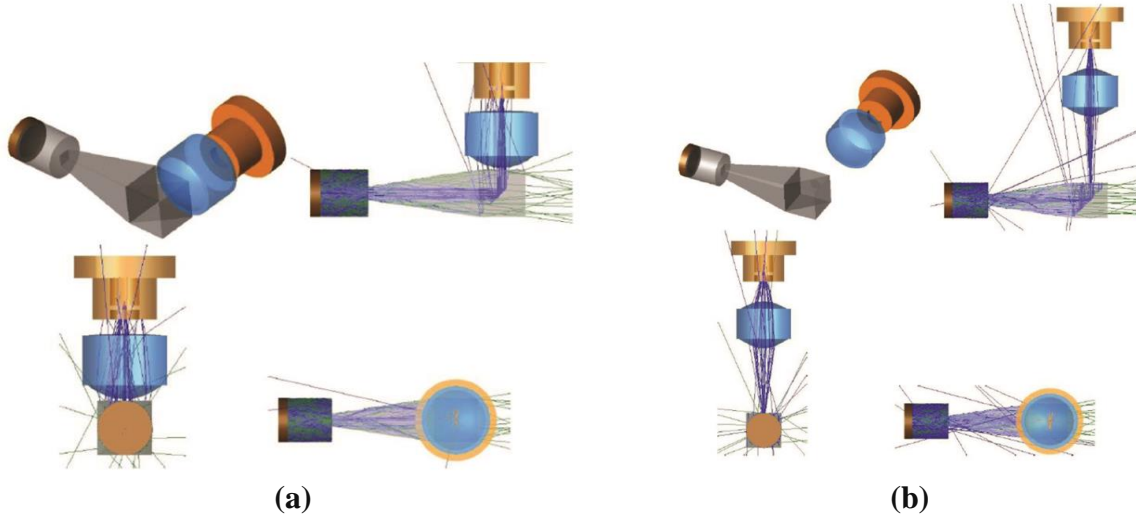


Figure 14 - Laser light coupling using (a) collimating and (b) focusing lenses.
(Images reproduced with permission from [70].)

Four optical design variations were selected in our design analysis. The design variations were studied based on the laser type coupling, whether it is collimated or focused and whether and index matching layer is deployed [70]. This results in four combinations: collimated light to air (CA), collimated light with index matching (CI), focused light to air (FA), and focused light with index matching (FI).

3.3.4 Performance Analysis

The resulting phosphor absorption for variation 1 (CA and CI) and Variation 2 (FA and FI) are shown in Figure 15 and Table 5 shows the following assumptions that were considered during the analysis [70]:

- Top coating reflectivity of SSLG is 99.5% broadband.
- Surface coating of heat sink is 99.5% broadband.
- Scattering of the green light from the phosphor is Lambertian.
- All components have no chips with ideal sharp edges.

- Absorbance percentages of phosphor are 25%, 50%, or 100% of UV light per pass, considering the rest is spread as Lambertian.

	Variation CA			Variation FA			Variation CI			Variation FI		
Phosphor Absorption	25%	50%	100%	25%	50%	100%	25%	50%	100%	25%	50%	100%
Laser Light Absorption	58%	70%	81%	61%	76%	89%	68%	78%	86%	68%	79%	89%
Phosphor Quantum Efficiency	90%			90%			90%			90%		
Stokes Shift	77%			77%			77%			77%		
Visible Light Extraction	86%			88%			86%			88%		
Total	35%	42%	48%	37%	46%	54%	41%	46%	51%	41%	48%	54%

Table 5 - Throughput analysis of the optical cavity for four design variations
(Table reproduced with permission from [70].)

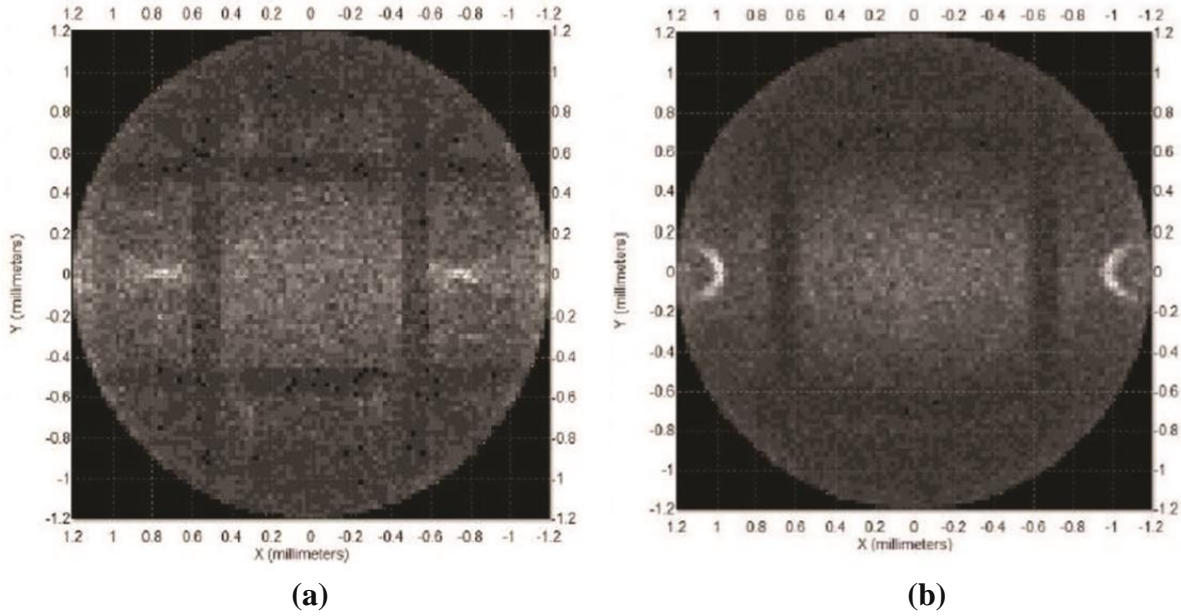


Figure 15 - Phosphor Absorption for (a) Version 1 and (b) Version 2
(Images reproduced with permission from [70].)

3.3.5 Discussion and Conclusion

Speckle in laser projection displays acts as a mask on the original image information which can severely degrade the image quality. So reducing the speckle in pico-projection applications is highly desirable [94] [95]. Pico-projector screen brightness technology can be enhanced using our proposed design as the light source is capable of providing speckle-free visible light at etendue

levels much lower than those provided by LED technology. The optical efficiency of the cavity was measured at 40%, this value agrees well with the analysis shown above. An efficacy of 20 lm/W for green light at an etendue of 3 mm².sr was measured using a 445nm laser. Eu doped silicates is the material that we used for the green phosphor, the material emission peak is 530nm and its excitation ranges from 200nm to 580nm [70]. For future work on enhancing the optical cavity performance, the plan will be to inkjet print the reflective mirror using aluminum NP ink on the inner walls of the cavity and characterize the projection system in terms of efficacy and etendue. This approach will be explored further in Chapter 6.

CHAPTER 4: METAL AEROSOL JET PRINTING

The research focus shifted from printed polymer components to printed metal electronics due to change of advisor. The new research focus demonstrates the versatility and value of metal 3D printing. This chapter is composed of two main areas. First, in Sections 4.1-4.7 a background investigation of whether using thermal curing for metallic structures on thermally intolerant materials is feasible was done by investigating printed silver cured for much shorter times. This investigation concluded that it is not practical to overcome thermal limitations through short thermal curing at high temperature similar to rapid thermal annealing in semiconductor processing. My work included all of the conductivity (DC and RF) measurements and test structures for the samples cured at short times. Based upon this result, optical curing becomes the main thrust of the thesis. The second part of the chapter starting with Section 4.8 provides the results for high conductivity printed silver with aggressive thermal curing, which was published with many co-authors [13]. I have included these results because they were done in parallel with the short curing study and I was actively printing and curing samples that resulted in that published work with another student, lead author Marvin Abt. The external corroboration of the conductivity results and RF measurements in that paper was the work of the other authors.

4.1 Motivation

The late 1990s is considered the beginning of new era in the world of 3D printing with the creation of metal 3D printers. Different metal 3D printing techniques using various energy sources and optimized materials have been developed for each printing technique in terms of flow rate, nozzle fouling, and substrate adhesion. [96]. It is equally important to develop curing techniques that work well with each optimized ink material and to recognize that curing imposes another set

of key constraints that differ from printing. In this work, we utilized the Optomec Aerosol Jet 5X for the 3D printing of silver ink on glass substrates. The concept is to:

- (1) Create CAD files using SolidWorks® that accurately describe the 3-types of transmission lines that were presented in [40].
- (2) Use the Optomec Aerosol Jet 5X for AJP fabrication of the 3-types of transmission lines from the CAD files.
- (3) Investigate the short-term cure condition of hot plate at 160°C for 10 minutes and at 200°C for another 10 minutes using measurements of transmission and reflection scattering coefficients. Material conductivity with thickness and size is also assessed.

4.2 Three Transmission Line Test Circuits

In 2014, Professor John Papapolymerou's group at Georgia Institute of Technology presented proof of concept that 3D printed interconnects fabricated using AJP technology can be used for multilayer passive microwave circuitry [97] [40]. We designed and printed three types of transmission lines similar to those in [40] using AJP at MSU. The goal of this work is to test the transmission lines that were cured using a hot plate (160-200°C) for short periods of time (10-20 minutes) and measure their performance in terms of material conductivity, thickness, feature size and the scattering parameters.

- Type-1a is a coplanar waveguide (CPWG) printed on 1mm glass substrate, and Type-1b is a conductor-backed coplanar waveguide (CB-CPW) structure printed on 1mm glass substrate.
- Type-2 is a CPWG printed on a 5x5 mm² single-crystalline diamond (SCD) wafer.
- Type-3a is a CPWG printed on a 1 Mil Polyimide Kapton Tape “25.4µm” attached to 1mm glass substrate. Type-3b has the same structure as Type-3a. The structure was printed on

DuPont Pyralux AC, product code AC182500EM; where the copper thickness is 18 μ m and polyimide thickness is 25 μ m. We utilized SolidWorks[®] as the CAD software to design the 2D model that is readable by the VMTools[™] as well as the 3D model that was used for simulation. We are one of the first groups at MSU to utilize SolidWorks[®] in this type of design due to its friendly user interface and ability to save the files in multiple formats that can be read by any 3D printer.

4.3 Design and AJP of Silver Ink Squares

In order to measure the silver ink conductivity after the curing process, 10mm x10mm squares were printed using Clariant EXPT Prelect TPS 5OG2 Ag ink. The silver ink viscosity is 15cP, solvents: Water, Ethylene glycol (CAS# 107-21-1), dilution: 1:1, Ink: DI Water, bath temperature: 25°C [53]. The square design was drawn using SolidWorks[®] by saving the sketch as DXF file. VMTools[™] was utilized to generate the PRG file that can be read by the Optomec Aerosol Jet 5X printer. VMTools[™] properties are set as follows: Serpentine Fill: Angle 0°, Enforce bounds. Perimeter Fill: Continuous. Trace Width: 25 μ m (0.025 Units). Min Overlap: 20, Max Overlap: 30, Join All Segments, Offset Outline. The nozzle size used was 150 μ m. Figure 16 shows silver ink square sketch (a), VMTools[™] properties (b), serpentine fill (c) and 3D printed model on glass substrate (d).

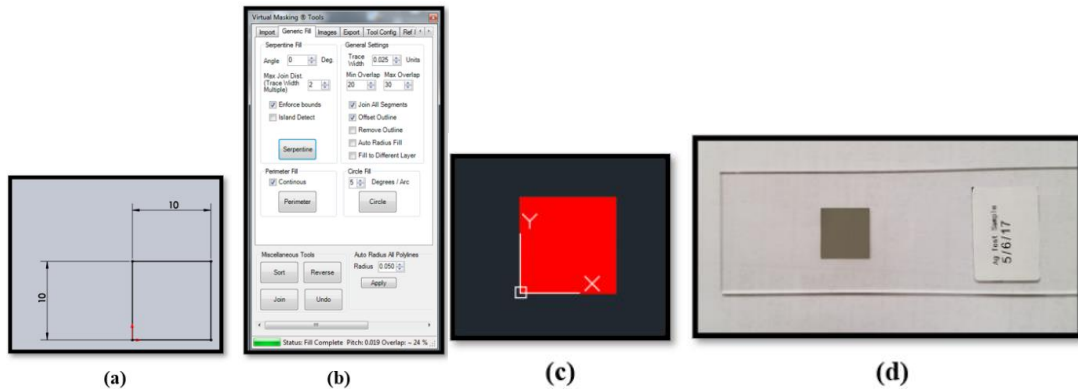


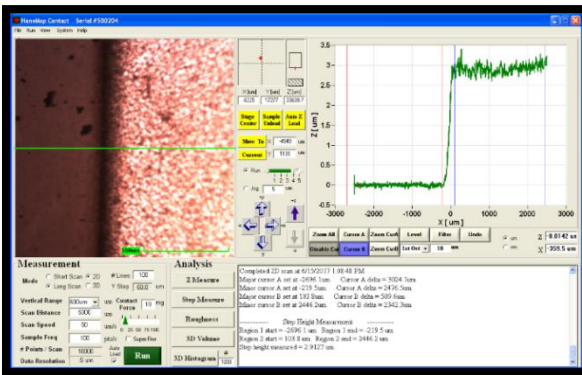
Figure 16 - (a) 10mm x 10mm silver ink square sketch (b) VMTools[™] properties(c) 10mm x 10mm serpentine fill (d) 3D printed model on glass substrate

The PRG file is then loaded to Aerosol Jet 5X printer using KEWA™ software; The Aerosol Jet hardware is controlled through the Knowledge Engineered Workstation Application or KEWA™, a group of graphical user interfaces (GUIs) that provide complete on-screen motion control, a vision system for alignment and process viewing, and many other tools useful for material printing and processing. KEWA™ consists of multiple independent applications, each of which can be initialized via the KEWA™ gadget [54].

The 10mm x 10mm silver ink square was printed in 1 pass with a 100µm nozzle on a glass substrate (25 x 75 x 1 mm³) from Globe Scientific Inc. Item # 1328. The distance from the nozzle to the substrate was between 2mm – 4mm. The printing stage speed was 2mm/s. The deposition was conducted with ultrasonic atomizer (UA); Sheath flow rate (S_MFC) @ 32 standard cubic centimeters per minute (sccm) and UA flow rate (UA_MFC) @ 24 sccm. The printing was conducted at room temperature. The substrate was sintered at 160°C for 10 min and at 200°C for another 10 min.

4.3.1 Material Thickness and Conductivity Measurements

The material thickness was measured using NanoMap 500LS System, the step height measurement (thickness of silver ink layer) and average roughness (R_a) were found to be 2.91µm and 0.0917µm respectively as shown in Figure 17 (a) and (b).



(a)



(b)

Figure 17 - Silver ink (a) step height and (b) average roughness (R_a) measurements

The material resistance [98] was measured using Pro-4 Four Point Resistivity System Figure 18, and it was found to be:

$$R = \frac{V}{I} = 15.94\Omega \quad (1)$$

where R is the resistance in Ω , V is the voltage in volts, and I is the current in Amperes. Power and voltage-current measurement were supplied through Keithley® 2400 sourcemeter. Material resistance can be calculated using formula (2):

$$R = \rho \frac{L}{A} = \rho \frac{L}{Wt} \quad (2)$$

where ρ is the resistivity in $\Omega\cdot\text{cm}$, A is the cross-sectional area in cm^2 , and L is the length in cm. The cross-sectional area can be divided into the width W in cm and the sheet thickness t in cm. By combining the resistivity with the thickness, the material resistance can then be calculated using formula (3):

$$R = \frac{\rho}{t} \frac{L}{W} = R_s \frac{L}{W} \quad (3)$$

where R_s is the sheet resistance in Ω/sq .

If the material thickness is identified, the bulk resistivity ρ ($\Omega\cdot\text{cm}$) can be calculated by multiplying the sheet resistance by the material thickness in cm units as shown in formula (4):

$$\rho = R_s \cdot t \quad (4)$$

and conductivity can be calculated using formula (5):

$$\sigma = \frac{1}{\rho} \quad (5)$$

where σ is the conductivity in S/cm and ρ is the resistivity in $\Omega\cdot\text{cm}$.

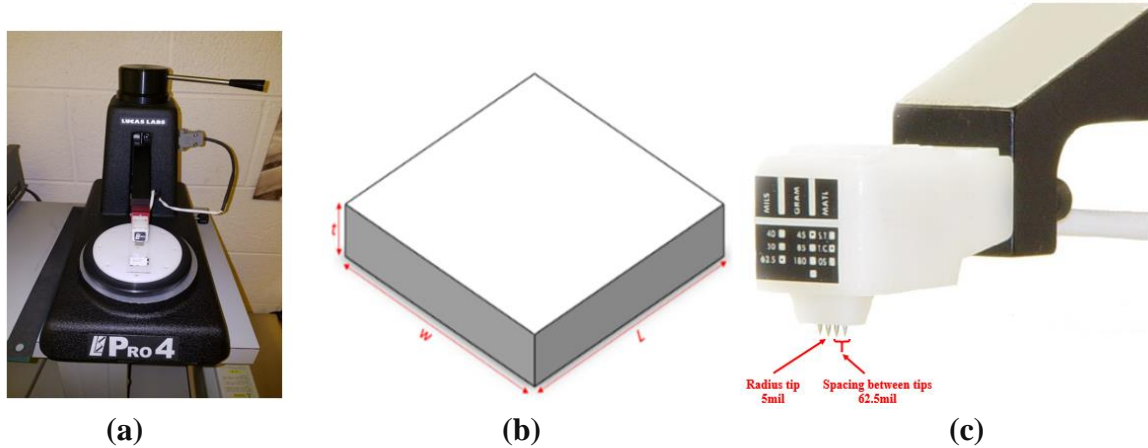


Figure 18 - (a) Pro4 setup, (b) Silver ink material geometry, and (c) SP4 4-point probe head
(Image (c) reproduced with permission from [58].)

Using the value of $\rho = 0.020068\Omega \cdot \text{cm}$ and $t = 2.91\mu\text{m}$, the calculated conductivity (σ) is 49.83S/cm . This value of conductivity is very small considering the sintering time of the sample was not long enough, i.e. 20 minutes.

4.4 Transmission Line (Type-1a)

Utilizing Clariant TP8 SOG2 Ag ink. A CPWG structure (Figure 19) was printed on 1mm glass substrate. VMTools™ properties are set as follows: Serpentine Fill: Angle 0° , Enforce Bounds. Perimeter Fill: Continuous. Trace Width: $25\mu\text{m}$ (0.025 Units). Min Overlap: 30, Max Overlap: 40, Join All Segments, Offset Outline. The nozzle size is $150\mu\text{m}$.

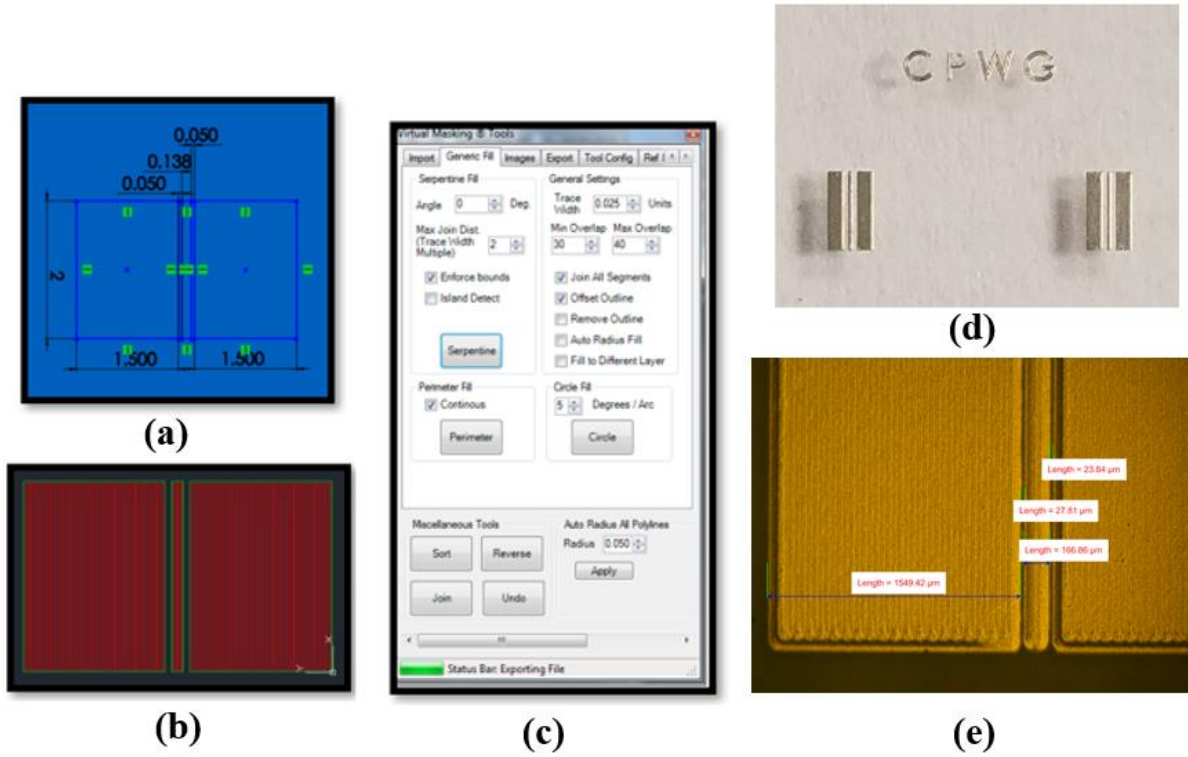
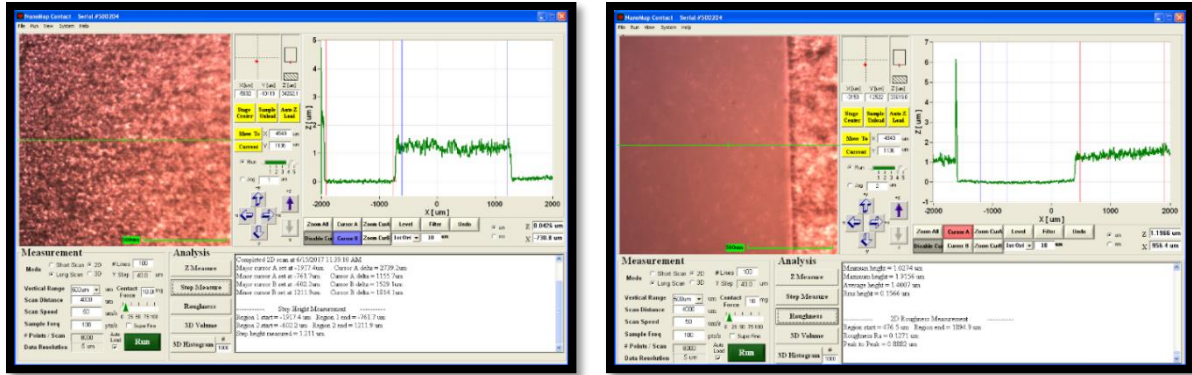


Figure 19 - (a) CPWG sketch (b) CPWG serpentine fill (c) VMTools™ properties (d) 3D printed model (e) Feature size measurement

The distance from the nozzle to the substrate was between 2mm – 4mm. The printing stage speed was 2mm/s. The deposition was conducted with UA; sheath flow rate (S_MFC) @ 32 sccm and UA flow rate (UA_MFC) @ 24 sccm. The printing was conducted at room temperature. The substrate was sintered at 160°C for 10 min and at 200°C for another 10 min.

4.4.1 Material Thickness Measurement (Type-1a)

The material thickness was measured using NanoMap 500LS system, the step height measurement (thickness of silver ink layer) and R_a were found to be 1.21μm and 0.127μm respectively as shown in Figure 20 (a) and (b).



(a)

(b)

Figure 20 - Type-1a Silver ink (a) step height measurement and (b) average roughness (R_a)

4.4.2 RF Data Measurement (Type-1a)

RF measurement were carried out using PNA Network Analyzer - N5227A; the frequency range was set from 100MHz to 67GHz.

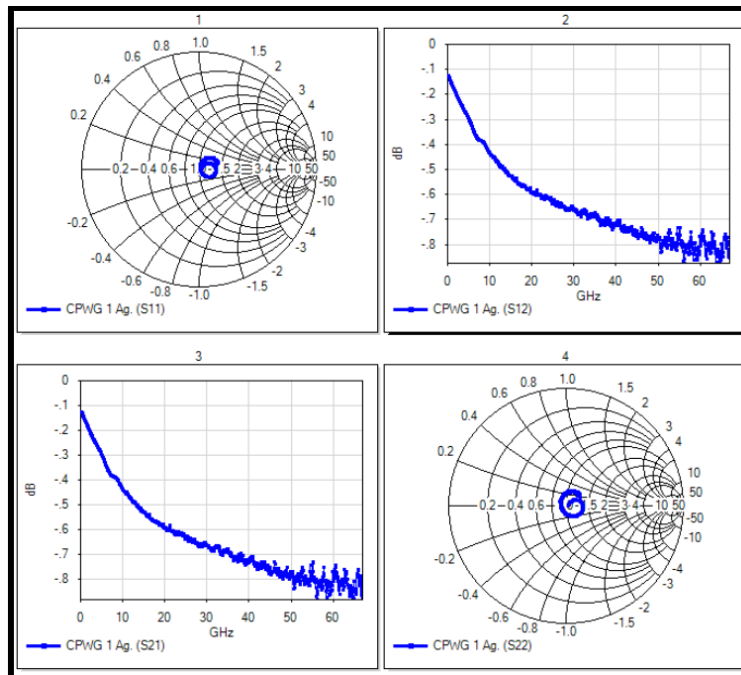


Figure 21 - Type-1a RF measurement

Figure 21 shows that the reflection coefficients S11 (input match) and S22 (output match) are in the resistive region. As for the transmission coefficients S21 (forward gain or insertion loss) and S12 (reverse gain or insertion loss), they are at -0.8dB at 60GHz. These results are due to the

high resistivity of the silver ink; i.e. material was not sintered long enough to give better conductivity.

4.5 Transmission Line (Type-1b)

Utilizing Clariant TP8 SOG2 Ag ink. A CB-CPW structure (Figure 22) was printed on 1mm glass substrate. CAD conversion utility (VM Tools) properties are set as follows: Serpentine Fill: Angle 90° , Enforce Bounds. Perimeter Fill: Continuous. Trace Width: $25\mu\text{m}$ (0.025 Units). Min Overlap: 30, Max Overlap: 40, Join All Segments, Offset Outline. The nozzle size is $150\mu\text{m}$.

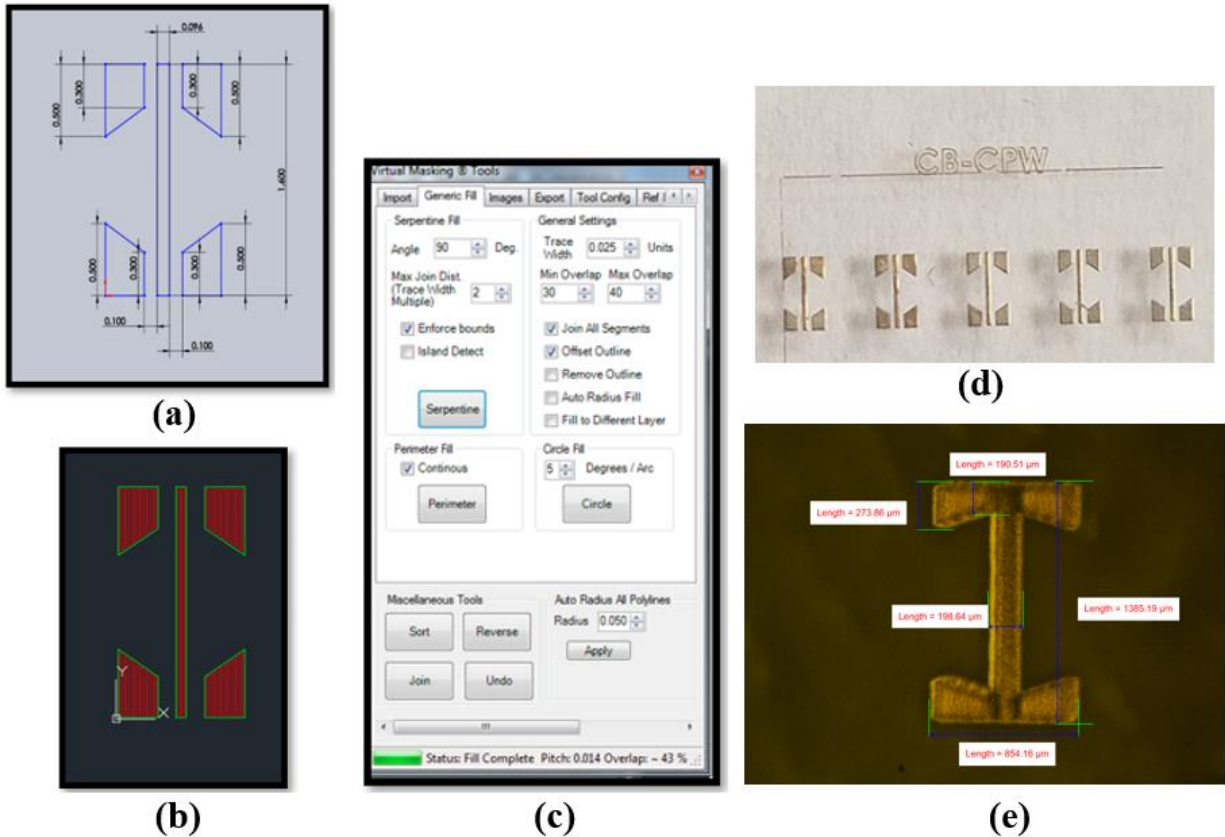


Figure 22 - (a) CB-CPW sketch (b) CB-CPW serpentine fill (c) VMTTools™ properties (d) 3D printed model (e) Feature size measurement

The distance from the nozzle to the substrate was between 2mm – 4mm. The printing stage speed was 2mm/s. The deposition was conducted with UA; sheath flow rate (S_MFC) @ 32 sccm and UA flow rate (UA_MFC) @ 24 sccm. The printing was conducted at room temperature. The substrate was sintered at 160°C for 10 min and at 200°C for another 10 min.

4.5.1 Material Thickness Measurement (Type-1b)

The material thickness was measured using NanoMap 500LS system, the step height measurement (thickness of silver ink layer) and R_a were found to be $1.21\mu\text{m}$ and $0.127\mu\text{m}$ respectively as shown in Figure 20.

4.5.2 RF Data Measurement (Type-1b)

RF measurement were carried out using PNA Network Analyzer - N5227A; the frequency range was set from 100MHz to 67GHz.

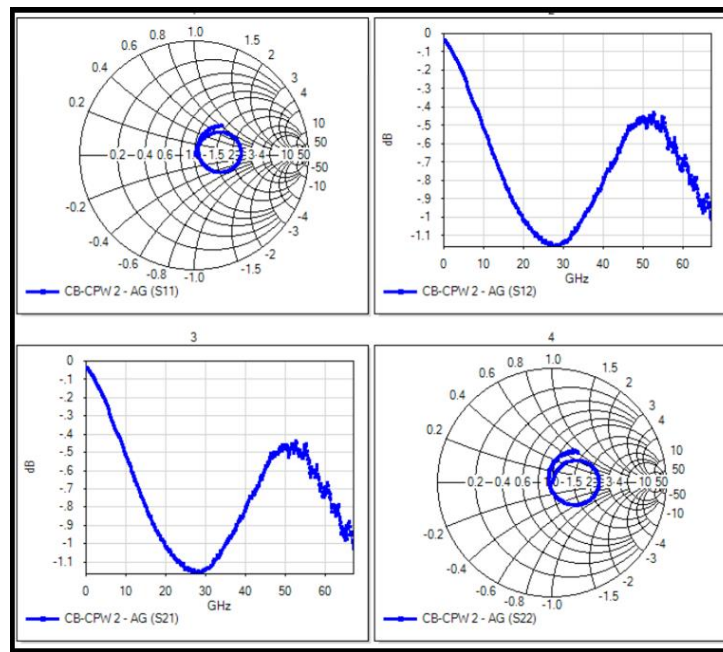


Figure 23 - Type-1b RF measurement

Figure 23 shows that the reflection coefficients S11 (input match) and S22 (output match) are in the resistive region. As for the transmission coefficients S21 (forward gain or insertion loss) and S12 (reverse gain or insertion loss), they are varying from -1.1dB to -0.5dB for frequencies between 30GHz to 60GHz. These results are due to the high resistivity of the silver ink; i.e. material was not sintered long enough to give better conductivity.

4.6 Transmission Line (Type-2)

In 2017, a combined effort between the Department of Electrical and Computer Engineering, Michigan State University and Fraunhofer USA-Center for Coatings and Diamond Technologies (CCD) extended this concept to fabrication of a coplanar waveguide (CPW) transmission line and monolithic Wilkinson power divider (WPD) printed on SCD substrate using AJP [99] [100]. A 3D printed trapezoidal configuration was printed on LCP and (CPW) were printed on top of the structure to imitate millimeter-wave packaging. Silver NP ink was used to print the CPW. After sintering for 1 hour at 200°C, 40% conductivity of the bulk silver was achieved. An Optomec Aerosol Jet 5X printer was used to print the CPW lines on LCP and VeroWhite substrates separately. The CPW interconnects generated insertion losses of as low as 0.49 dB/mm including the trapezoid, and with a loss of 0.38 dB/mm on LCP substrate at 110 GHz. The trapezoidal configuration was printed using Objet Connex350 3D printer on LCP [101].

4.7 Transmission Line (Type-3)

Utilizing Clariant TP8 SOG2 Ag ink. A CPWG structure (Figure 24) was printed on 1 Mil Polyimide Kapton Tape “25.4µm” attached to 1mm glass substrate and the same structure was printed on DuPont Pyralux AC, product code AC182500EM; where the copper thickness is 18µm and Polyimide thickness is 25µm. VMTools™ properties are set as follows: Serpentine Fill: Angle 0°, Enforce Bounds. Perimeter Fill: Continuous. Trace Width: 25µm (0.025 Units). Min Overlap: 30, Max Overlap: 40, Join All Segments, Offset Outline. The nozzle size is 100µm.

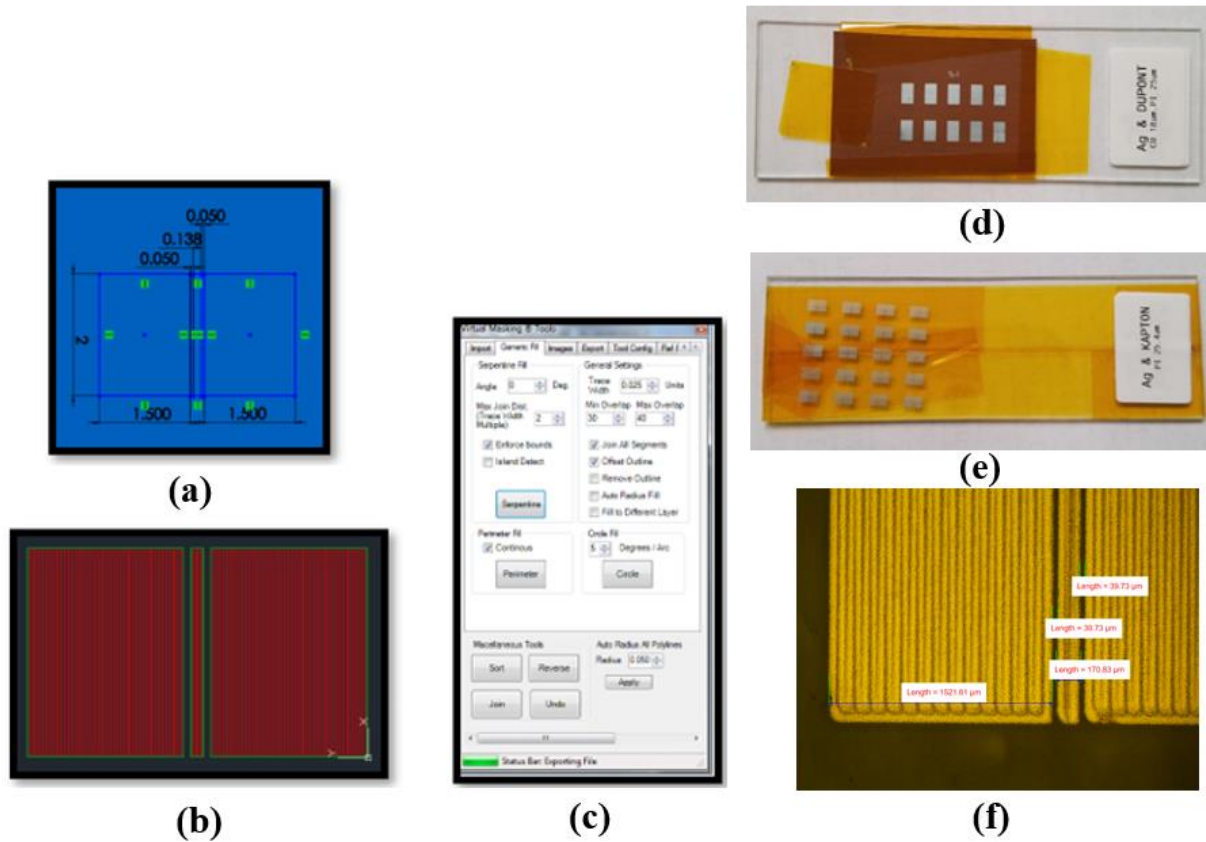


Figure 24 - (a) CPWG sketch (b) CPWG serpentine fill (c) VMTools™ properties (d) 3D printed model on DuPont AC182500EM (e) 3D printed model on 1mil Kapton tape (f) Feature size measurement

The distance from the nozzle to the substrate was between 2mm – 4mm. The printing stage speed was 2mm/s. The deposition was conducted with UA; sheath flow rate (S_MFC) @ 32 sccm and UA flow rate (UA_MFC) @ 24 sccm. The printing was conducted at room temperature. The two substrates were sintered at 160°C for 10 min and at 200°C for another 10 min.

4.7.1 Material Thickness Measurement (Type-3)

The material thickness was measured using NanoMap 500LS system, the step height measurement (thickness of silver ink layer) and R_a were found to be 1.21μm and 0.127μm respectively as shown in Figure 20.

4.7.2 RF Data Measurement (Type-3)

RF measurement were carried out using PNA Network Analyzer - N5227A; the frequency range was set from 100MHz to 67GHz.

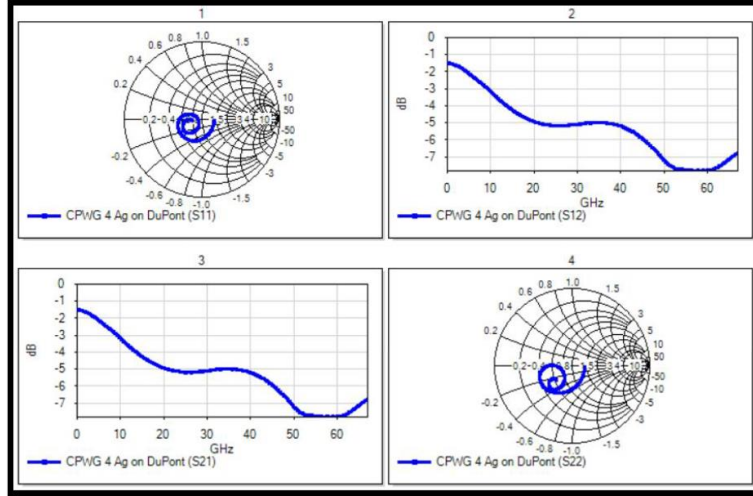


Figure 25 - Type-3 RF measurement

Figure 25 shows that the reflection coefficients S11 (input match) and S22 (output match) are in the resistive region. As for the transmission coefficients S21 (forward gain or insertion loss) and S12 (reverse gain or insertion loss), they are varying from -1.5dB to -75dB for frequencies between 0GHz to 60GHz. These results are due to the high resistivity of the silver ink; i.e. material was not sintered long enough to give better conductivity.

4.8 Highly Conductive Ink for Flexible Electronic Devices

In this section, we studied aerosol jet printing on flexible substrates for wearable and flexible electronic devices. My contribution included silver ink printing on glass substates and LCP / Kapton foils, curing the devices on hot plate, measuring scattering parameters, making a manual on how to print devices using Optomec Aerosol 5X Jet Printer utilizing ultrasonic and pneumatic atomizer as well as making a manual for PNA Network Analyzer - N5227A. This work led to a journal publication led by Professor Aljoscha Roch with IEEE Transactions on

Components, Packaging and Manufacturing Technology in October 2018 [13] which contained some of the results of this work.

4.8.1 Metal Organic Silver Ink

Utilizing inkjet printing to print organic metals such as silver ink showed conductivity of 30-75% of bulk silver. The material was sintered using muffle furnaces and hot plates. Ideal sintering temperatures were between 150°C and 200°C [102] [103]. In general, using AJP reported lower conductivity compared to inkjet printing. The conductivity was below 40% of bulk silver when the material was sintered at temperatures around 200°C [104] [105]. Other research groups reported conductivity of 20-40% of bulk Ag after 1 hour of sintering if the Clariant Ag NP ink was cured at 200°C in a furnace [104]. This low conductivity could be attributed to the material's uneven deposited surface using AJP [106]. Nonetheless, other inks such as ceramics, composites and dielectric polymers were tested using 3D printers [107] - [110]. On the other hand, a major problem with printed materials has to do with devices performance. In order to achieve better properties of the sintered material, the curing temperature should be within the heat tolerance of the flexible polymer substrates. Aerosol jet printers require material viscosity between 1 to 1000 mPa.s. Hence, a higher load can be printed comparing to inkjet printers as long as the particle diameter is below 100 nm. Many materials have been printed using AJP technology, conducting polymers such as Poly(3,4-Ethylenedioxythiophene) Polystyrene Sulfonate (PEDOT:PSS) [107] [111] as well as silver ink [112] and even materials for UV sensor applications like single-walled carbon nanotubes (CNT) [113]. AJP printers are better equipped for printing thin lines, favored by printed electronics manufacturers [13] [106].

In this work, we demonstrated the process of increasing silver ink conductivity. We also demonstrated the use of AJP for flexible electronic applications [13]. Lithographic techniques have

been always the approach for microwave and RF applications as they require thin lines and fine structures; however those techniques are complex and expensive. On the other hand, using a low-cost and environment-friendly AJP technology serves as an alternative for lithography process without sacrificing accuracy [97]. Printing parameters, such as line width, line thickness and viscosity can be adjusted using different nozzle sizes and changing material viscosity [106]. We printed silver ink on flexible substrates such as Kapton and LCP foils as well as glass slides. Glass slides were used to study silver ink conductivity. We investigated silver ink conductivity at low sintering temperatures. To achieve good conductivity, binder components have to be removed completely while increasing the sintering temperature gradually. Hence, binder components removal is a diffusion process which is time consuming and temperature dependent. Consequently, 16 hours of curing profile was reported. This method accurately demonstrates the potential of investigating silver ink conductivity. Lastly, the performance of AJP printed CPW lines were tested up to 110 GHz and the results were compared to the simulated ones. IJP techniques showed highly significant losses at the V- band [114]. The AJP lines offer lower losses at VHF that are comparable to copper lines [13].

4.8.2 Experimental Circuit Fabrication

Optomec Aerosol Jet 5X printer was utilized for printing the silver ink. The printer is capable of printing on 3D surfaces as it is equipped with 5 axes. Clariant type: TPS 50G2 silver ink was used as the printing material [104]. Dilution ratio was 1 mL of Clariant ink to 2 mL of deionized water. We used 25- μ m Kapton foil substrate from DuPont, 50- μ m LCP foil substrate from LCP Rogers Ultralam 3850HT and glass slides. The UA of the Aerosol printer was utilized for printing the silver ink. Pro4, the four-point probe from Lucas Labs was used to measure the silver ink conductivity. We used the UA of the AJP for printing the diluted ink. Figure 26 shows

flexible film (a), foldable film (b) and thin film resistivity measurement of 1.6Ω using FLUKE 115 True-RMS multimeter (c).

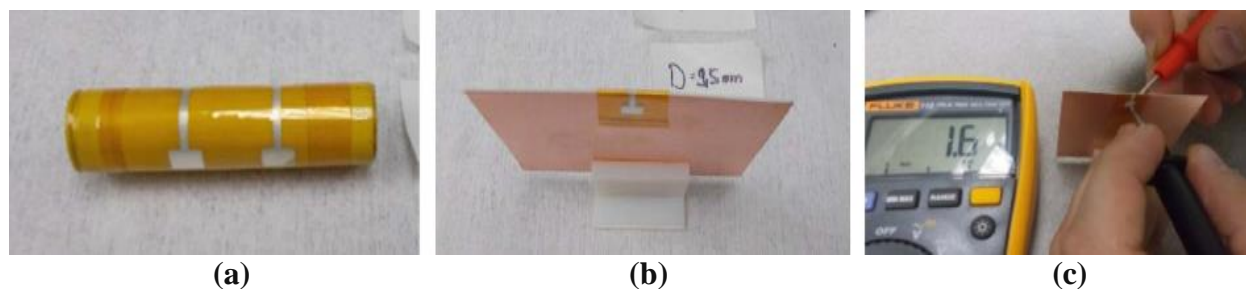


Figure 26 - (a) Flexible film (b) Foldable film (c) Resistivity measurement

(Images reproduced with permission from [13].)

Printed layer's flexibility was performed by printing the lines on Kapton foils and sintering them up to 200°C . There was no significant change to the resistivity value that is measured with the multimeter after bending the foil around the sharp edges. The resistance value remained at 1.6Ω . This shows that the sintered ink is highly flexible. Material deposited thickness was around $1\text{-}2\mu\text{m}$. A $10\text{ mm} \times 10\text{ mm}$ silver ink square was printed on glass substrate to measure the electrical conductivity as a function of curing time and temperature up to 200°C . Accurate thickness measurement was achieved using the profilometer "NanoMap 500LS" from AEP Technology as the material was printed on glass substrate. 30% to 50% material overlap of the printed transmission lines was applied to the tool path of AJP printer. This overlap assures dense connected lines. $150\text{ }\mu\text{m}$ nozzle head was used which guarantees line widths between $20\text{ }\mu\text{m}$ to $40\text{ }\mu\text{m}$ depending on the gas flow parameters. AJP maintained atomizer gas flow of 22 - 24 sccm and sheath flow of 32 - 34 sccm. The printed samples were cured using hot plate in ambient environment, the samples were covered with Petri dish so convection cooling will be reduced. LCP transmission lines were sintered up to 160°C while Kapton transmission lines were sintered up to 200°C . Agilent N5227A PNA Network Analyzer (for 10MHz - 67 GHz) and VDI WR10-VNAX

extension modules (for 75 - 110 GHz) were used to measure the transmission lines frequencies [13].

4.8.3 Results and Discussion

We used TGA measurements to determine Clariant silver ink content and at what temperature do the additional ink components evaporate. According to the TGA analysis, large amounts of water in the ink evaporated at 100°C as anticipated. A second inflection point was noticed between 120°C to 160°C. A third broadband appeared around 190°C. We didn't notice any major weight change in the material beyond 160°C. We concluded that the most of the additives evaporated using sintering temperatures between 120°C to 160°C. Lastly, we established that a mass content of 35 wt% of silver ink is in the diluted ink as shown in Figure 27 [13].

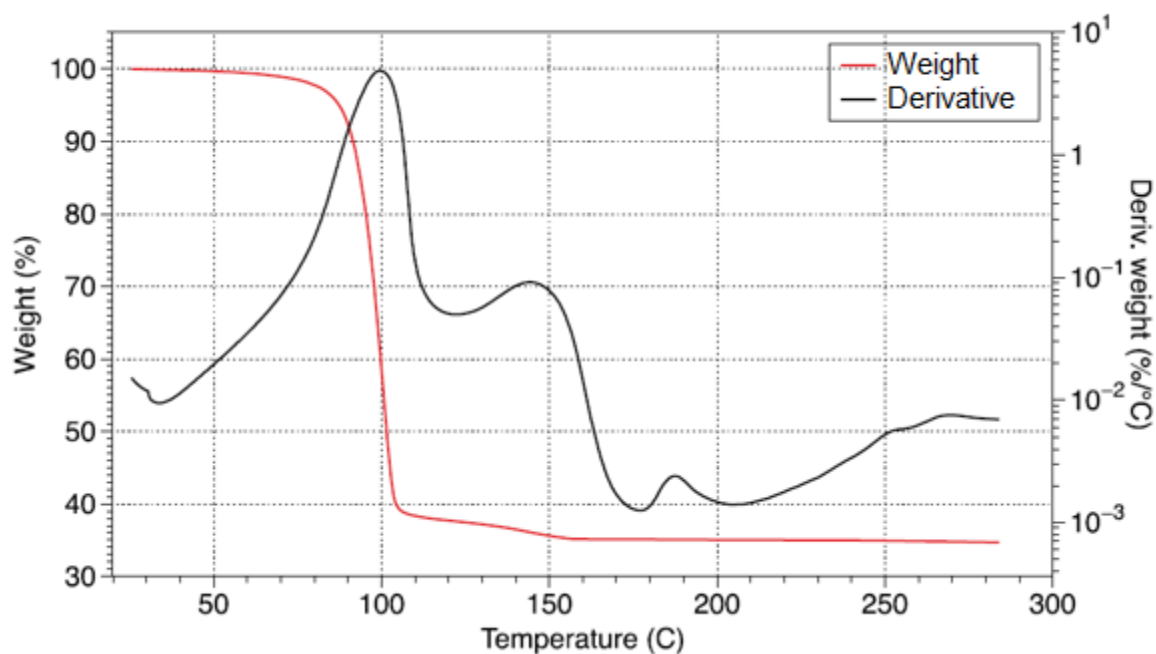


Figure 27 - TGA measurement of the Clariant ink diluted with deionized water in dry air
(Image reproduced with permission from [13].)

The results of temperature, sintering and conductivity of the printed Ag layers on glass slides are shown in Figure 28(a). The values were measured relatively to bulk Ag with 6.3×10^7

s/m [115] [116]. Sintering process with a sample on the hot plate, covered with a petri dish to reduce convective airflow over the sample surface is shown in Figure 28(b) [13].

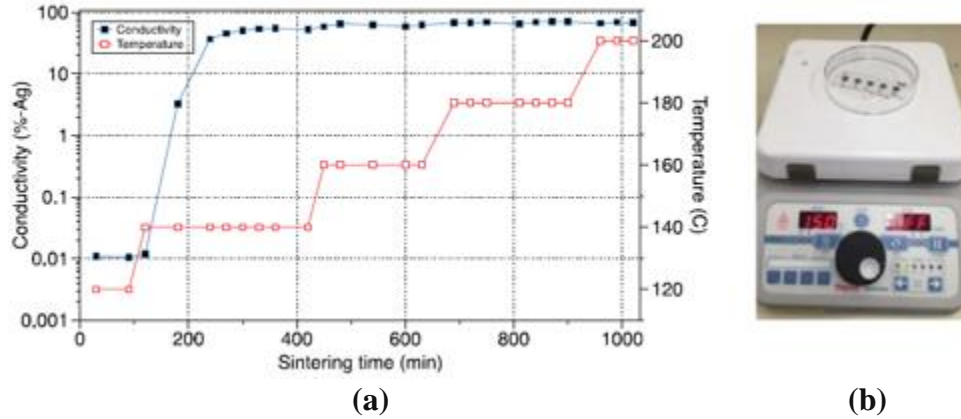


Figure 28 - (a) Electrical conductivity of printed and sintered Ag as a function of temperature and sintering time (b) 10 x 10 mm silver ink layers sintered on a hot plate.
(Images reproduced with permission from [13].)

Clearly, curing temperature and sintering time play major roles in ink conductivity. Increasing the temperature beyond 200°C didn't show any significant increase in conductivity. The thickness of the layer was measured every time to record the shrinking of the layer (Figure 29). The strong shrinking of the layer at 140°C indicates the starting of the sintering process. Almost 30% of the layer height was lost by the heat treatment at 140°C. However, the shrinkage was found just for the layer height [13].

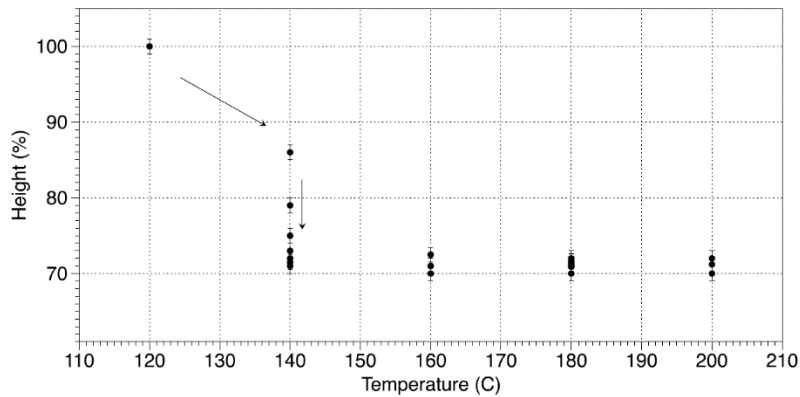


Figure 29 - Shrinking behavior of the printed Ag layer printed on glass substrate and sintered on a hot plate
(Image reproduced with permission from [13].)

Other research groups achieved 20-40% of bulk AG by sintering Clariant ink TPS 50G2 at 200°C [104]. 60% of electrical conductivity of bulk silver was measured after long hours of sintering the sample at 140°C. It was noted that the silver ink was still soft after 1 hour of sintering. Better electrical conductivity was measured after increasing the curing temperature slowly beyond 120°C. Using this technique and increasing the sintering temperature up to 200°C we obtained electrical conductivity of 70% of Ag. Nonetheless, the major increase in conductivity started at 140°C. The measuring experiments were repeated 3 times. We assumed 5%-10% total error of the electrical conductivity. Lastly, we printed transmission lines on LCP and Kapton foils. Height measurement of the deposited ink was 7µm for Kapton and 16µm for LCP. The printed CPW lines widths were selected so that they are well-suited with the RF probe pitch in the laboratory. 25µm-thick Kapton foil insertion loss for the 30µm and 50µm spacing were 0.55 and 0.94dB/mm at 110GHz. While the insertion losses for the 50µm on LCP were 0.37 and 0.63dB/mm. Those values are similar to 0.38dB/mm for the AJP printed lines on 175µm-thick LCP and they are also equivalent to CPW printed with copper traces with 0.088-0.25dB/mm losses on comparable substrates [116] [13]. Figure 30 shows the simulated and the measured insertion and return losses for the CPWs on LCP and Kapton foils [13].

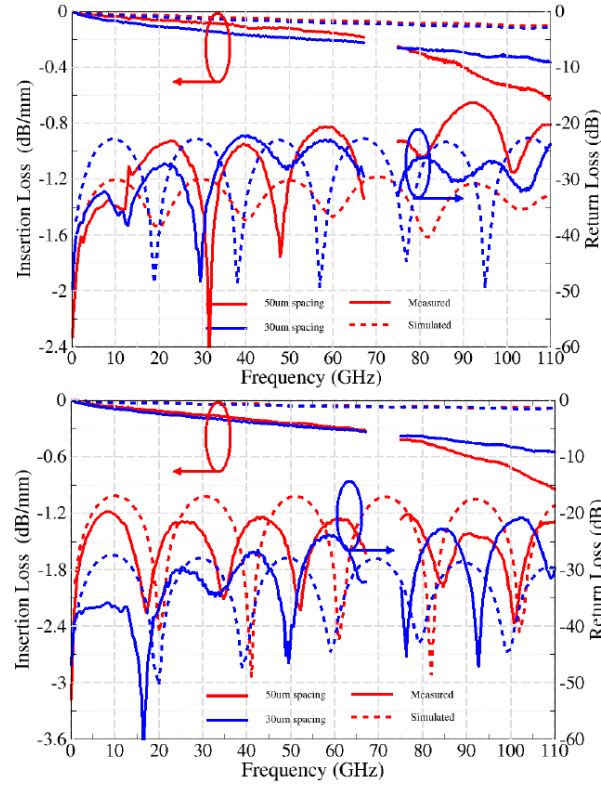


Figure 30 - Simulated and measured insertion loss per millimeter and return loss for different susbtrates: LCP (a) and Kapton (b)
(Images reproduced with permission from [13].)

4.9 Conclusion

CPWG and CB-CPW represent a type of transmission lines which have multiple applications. They are ideal candidates for transmission applications due to their small size, light weight and shape. Using Aerosol jet printer, we printed transmission lines using silver ink NPs and tested their scattering parameters up to 67GHz. It was demonstrated that three types of transmission lines were designed and fabricated using silver ink as the conductive material. Measurement of material thickness and sheet resistance of silver ink were carried out using 10mm x 10mm square printed on glass substrate, the two values were measured at $2.91\mu\text{m}$ and $68.96 \Omega/\text{sq}$ respectively. The calculated conductivity (σ) is 49.83S/cm . As for the three transmission lines, the material thickness was measured at $1.21\mu\text{m}$. we noticed for most of the frequency range for S11, S12, S21 and S22 that they were not well matched due to the high resistivity of the silver

ink, i.e. material was not sintered long enough to give better conductivity. It is noticed that temperature and sintering time play major roles to achieve a working 3D printed transmission line. We also investigated the AJP feature size and found out that the system delivered very fine features. The need for a different curing method that can sinter the inkjet printed material becomes obvious in terms of shorter periods of sintering times and low thermal budget.

As for the highly conductive ink sintered with a hot plate, the measured conductivity of 70% of bulk silver is the highest stated electrical conductivity for Aerosol printed electronics with sintering temperature of 200°C. This value was achieved with commercially available NP ink which is a promising path for printing electronics. Moreover, as this ink proves to be conductive at low sintering temperatures, it makes it a good candidate for future applications. Temperatures between 120°C and 140°C are good enough to sinter the material by increasing the time. Ink additives can be removed at temperatures lower than 140°C if sintered long enough. RF transmission lines were printed with silver ink and they showed comparable results relating to copper lines. Moreover, other electronic components such as antennas, inductors, resistors and sensors can be successfully produced using AJP. This makes AJP technology a promising path besides inkjet printing. The TGA analysis proved that ink additives can be removed if the sample was sintered at temperatures <140°C, but requires longer time to achieve that goal [13].

Clearly, using hot plate to cure the material works well with RF devices that are directly printed on glass substrate with no other material sandwiched in between. As for sensitive devices such as OLEDs and TPVs and due to the existing of organic materials deposited in between the substrate and the electrodes, a need for a different curing method is a must as high curing temperatures (200°C) for long period of time (16 hours) will damage the organic material. In

Chapter 5 we propose a novel optical curing system that can be used to cure the contacts of devices that are easily damaged by aggressive thermal processes.

CHAPTER 5: 3D PRINTED ELECTRONICS WITH OPTICAL CURING

The investigations of Chapter 4 clearly demonstrated that both thermal and high-power UV curing are not optimal for 3D printed Ag electronics on realistic substrates, especially flexible organic substrates. In this chapter, the results of a first-time investigation on the use of optical precision curing for 3D printed Ag electronics through the adaptation of a H3S. This instrument was made available through collaborative partnership with the University of South Carolina/Ronald E. McNAIR Center for Aerospace Innovation and Research.

My thesis work is a first-time investigation of its usefulness for 3D printed metal electronic conductors.

5.1 3D Printed Silver Ink Test Structures on Glass Substrates

In order to determine the effectiveness of the H3S for curing the 3D printed silver ink, 10 samples of 5mm x 5mm Silver Ink (Ag) 3D printed on glass substrates using Optomec Aerosol Jet 5X Printer composed of 1 layer, 3 layers, 5 layers, 10 layers and 15 layers then flashed using a H3S. We used the Ag ink from Clariant Type: TPS 50G2, it is also used in [104]. A 1 mL of the Clariant ink was mixed with 2-mL deionized water. As substrates, we used glass slides. We used the UA of the Optomec Aerosol 5X printer for printing the diluted ink. 1-printed layer thickness is measured to be 1.5 μ m. The nozzle size used during the print was 300 μ m.

5.2 Optical Pulse Heating Profile and Exposure Time

We printed 2 samples of each layer thickness and cured the samples using H3S at different temperatures and exposure times as shown in Table 6. Exact conditions were as follows:

- For the 1-layer sample that was cured at 35°C for 20 minutes, the system started at 101V then stabilized at ~124V during the curing process to maintain that temperature. For the 1-layer

sample that was cured at 100°C for 50 minutes, the system started at 150V then stabilized at ~138V during the curing process to maintain that temperature.

- For the 3-layer sample that was cured at 35°C for 20 minutes, the system started at 123V then stabilized at ~100V during the curing process to maintain that temperature. For the 3-layer sample that was cured at 100°C for 50 minutes, the system started at 160V then stabilized at ~138V during the curing process to maintain that temperature.
- For the 5-layer sample and the 10-layers sample that were cured together at 35°C for 30 minutes, the system started at 115V then stabilized at ~111V during the curing process to maintain that temperature. For the 5-layer sample that was cured at 100°C for 50 minutes, the system started at 170V then stabilized at ~136V during the curing process to maintain that temperature.
- For the 10-layer sample that was cured at 100°C for 50 minutes, the system started at 150V then stabilized at ~136V during the curing process to maintain that temperature.
- For the 15-layer sample that was cured at 35°C for 30 minutes, the system started at 111V then stabilized at ~110V during the curing process to maintain that temperature. For the 15 layers sample that was cured at 100°C for 50 minutes, the system started at 150V then stabilizes at ~135V during the curing process to maintain that temperature.

No.	Silver Ink Sample Layers	Temperature	Exposure Time
1	1 Layer – 1L	35°C	20 min
2	1 Layer – 1L	100°C	50 min
3	3 Layers – 3L	35°C	20 min
4	3 Layers – 3L	100°C	50 min
5	5 Layers – 5L	35°C	30 min
6	5 Layers – 5L	100°C	50 min
7	10 Layers – 10L	35°C	30 min
8	10 Layers – 10L	100°C	50 min
9	15 Layers – 15L	35°C	30 min
10	15 Layer5 – 15L	100°C	50 min

Table 6 - Desired temperature and exposure time for the samples

5.3 Sample Mounting for Optical Curing in the H3S

This run was performed with the sample taped to the steel tool. For all runs, a piece of cardboard was taped to the steel layup tool to serve as an insulator between the sample and the tool. This helps by keeping temperature more constant. Figure 31 demonstrates dual (a) and single (b) samples being cured at the same time, while Figure 32 shows the heater crystal is ready and in place (a) and heater is ON (b) during the curing process.

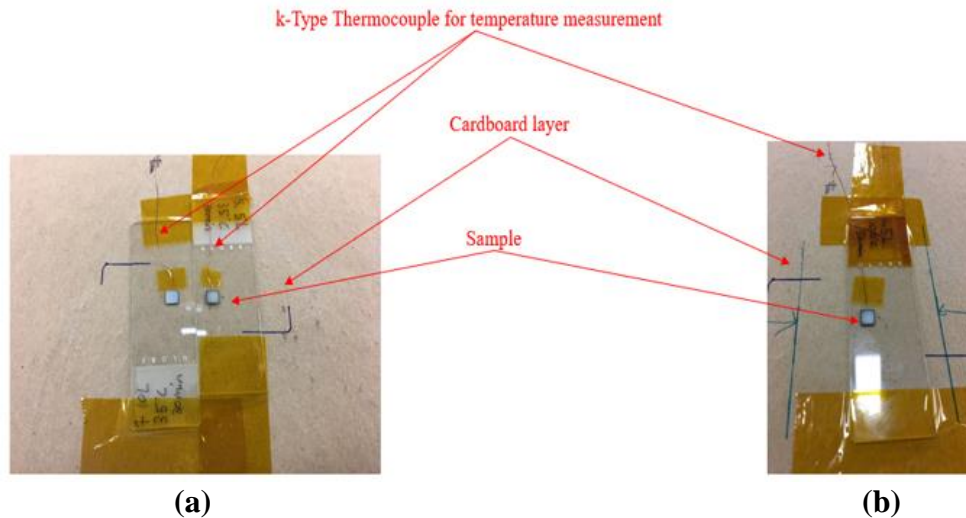


Figure 31 - (a) Dual samples (b) Single sample

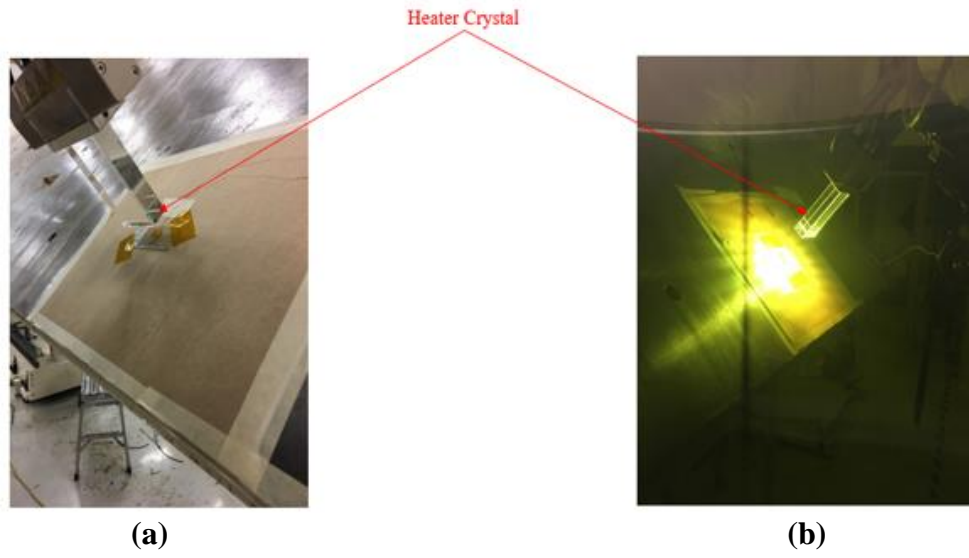


Figure 32 - (a) Heater crystal in place (b) Heater ON

Using the H3S control software, we vary the voltage to get the desired temperature while the frequency is set at 60Hz and the pulse duration is set at 2000 μ s. The sample is between 1inch and 2inch far from the crystal. Crystal height and voltage are adjusted to get the desired temperature for curing. A k-type thermocouple is used to monitor the temperature. Due to safety concerns the system has been tuned without a sample then the system is turned off and the sample is placed on stage then cured. There is a momentary ramp up (\sim 1s) to the desired temperature but it is almost instant.

5.4 Sintering Results

The 10 samples were cured at 35°C for 20-30 minutes (5 samples) and 100°C for 50 minutes (5 samples). Table 7 shows the time vs temperature for the cured samples at 35°C while Table 8 shows the time vs temperature for the cured samples at 100°C. The selection of low temperatures to cure the contacts is to investigate if those temperatures are good enough to make the silver ink contacts conductive and also to find low profile temperature to be used when curing OLED and TPV devices as they require low curing temperatures below 150°C.

Minute	No. of Layers				
	1 Layer	3 Layer	5 Layer	10 Layer	15 Layer
	Temperature (°C)	Temperature (°C)	Temperature (°C)	Temperature (°C)	Temperature (°C)
1	25.0	37.0	28.3	29.0	30.9
2	25.0	36.0	31.8	31.0	36.1
3	25.0	35.7	36.0	34.3	36.2
4	33.0	35.5	36.5	34.8	35.2
5	35.5	35.7	36.0	34.2	35.5
6	35.5	35.5	34.5	34.5	35.7
7	35.5	35.3	33.1	31.9	36.1
8	35.5	35.6	34.6	33.1	35.7
9	35.5	35.8	35.3	33.9	35.2
10	35.6	35.7	36.0	34.6	35.3
11	35.6	34.8	36.1	34.6	35.7
12	35.6	34.9	36.2	34.6	35.9
13	35.6	34.9	36.4	34.8	35.7
14	35.6	35.5	36.1	34.8	35.4
15	35.6	35.4	36.5	34.9	35.2
16	35.5	35.4	35.9	34.5	35.1
17	35.5	35.1	36.0	34.5	35.9
18	35.5	35.5	36.3	34.7	36.2
19	35.5	35.5	36.4	34.9	36.3
20	35.5	35.3	36.2	34.7	35.8
21			36.0	34.6	35.7
22			36.5	35.1	35.9
23			36.7	35.2	35.7
24			36.4	35.0	35.3
25			35.8	34.5	35.0
26			35.9	34.5	35.0
27			36.3	34.9	35.2
28			36.5	35.2	35.2
29			36.7	35.4	35.6
30			36.2	34.7	35.4
<i>Average Temp.</i>	33.8	35.5	35.6	34.2	35.4

Table 7 - Measured sample temperatures during sintering for 20-30 minutes at 35°C

Minute	No. of Layers				
	1 Layer	3 Layer	5 Layer	10 Layer	15 Layer
	Temperature (°C)	Temperature (°C)	Temperature (°C)	Temperature (°C)	Temperature (°C)
1	35.0	90.6	96.9	103.5	99.1
2	83.1	100.2	100.4	101.3	100.2
3	93.1	100.2	101.1	101.3	101.0
4	100.8	101.4	101.1	100.5	102.8
5	104.8	100.5	101.6	100.6	101.4
6	102.9	99.8	101.5	101.7	100.6
7	100.5	100.3	100.7	101.5	99.0
8	100.3	100.1	100.4	100.2	100.5
9	100.4	100.2	100.0	100.5	101.6
10	100.7	100.7	99.5	99.3	102.4
11	99.3	100.7	100.4	99.6	101.2
12	99.2	100.8	101.2	98.9	100.8
13	100.6	100.8	101.1	100.0	99.8
14	100.9	100.7	100.4	99.1	98.7
15	101.5	100.7	100.1	100.4	98.6
16	100.7	100.9	101.5	99.8	99.1
17	100.4	100.1	100.8	100.0	99.4
18	100.1	99.2	101.2	99.4	100.2
19	99.7	99.2	99.8	100.3	101.3
20	99.2	100.3	99.3	101.1	100.8
21	100.0	101.1	98.4	100.3	100.5
22	100.1	101.2	99.5	99.9	100.8
23	99.5	101.2	101.8	99.9	101.6
24	99.6	101.8	100.4	99.5	102.0
25	99.1	100.9	98.6	98.5	102.6
26	98.9	99.8	98.2	99.7	99.7
27	100.2	99.5	99.3	100.3	98.8
28	101.2	99.3	99.6	100.8	98.6
29	101.2	99.3	98.3	102.1	99.1
30	101.5	99.3	98.4	101.0	100.0
31	101.2	99.8	99.2	100.4	101.0
32	101.3	99.5	99.7	100.8	100.3
33	99.6	100.4	99.7	100.5	99.5
34	99.1	100.2	99.8	100.4	99.4
35	99.0	100.3	99.8	100.4	100.6
36	98.5	100.2	99.8	101.1	100.4
37	98.8	99.7	101.3	101.3	99.9
38	100.1	99.5	101.0	103.2	101.7
39	100.5	99.7	100.5	101.9	101.2
40	100.2	100.5	101.8	101.7	101.5
41	101.1	100.5	100.9	100.2	100.9
42	101.0	100.8	101.1	101.4	100.3
43	100.9	100.9	101.4	101.8	100.4
44	100.8	101.2	100.4	100.0	100.4
45	100.5	99.9	98.7	98.7	100.2
46	100.2	98.9	98.7	98.2	99.5
47	101.1	99.1	99.0	98.7	100.6
48	100.7	99.7	98.6	99.5	100.0
49	101.0	98.7	98.4	99.5	99.6
50	100.2	99.1	98.4	100.0	100.3
Average Temp.	98.6	100.0	100.0	100.4	100.4

Table 8 - Measured sample temperatures during sintering for 50 minutes at 100°C

Figure 33(a) shows the time vs temperature for the cured samples to reach 35°C. It is noticed that for 1 layer and 3 layers samples the curing time was only for 20 minutes. The time needed to activate the initial thermal ramp decreased as the number of layers increased, as indicated by the red dashed line in Figure 33(a). An early temperature spike was observed for the 3-layer sample. Figure 33(b) shows the time vs temperature for the cured samples to reach 100°C. An early temperature spike was observed for the 10-layer sample. A similar pattern of reduced thermal ramp activation time with increased number of layers was observed, although the time differences were less pronounced as indicated by the red dashed line in Figure 33(b).

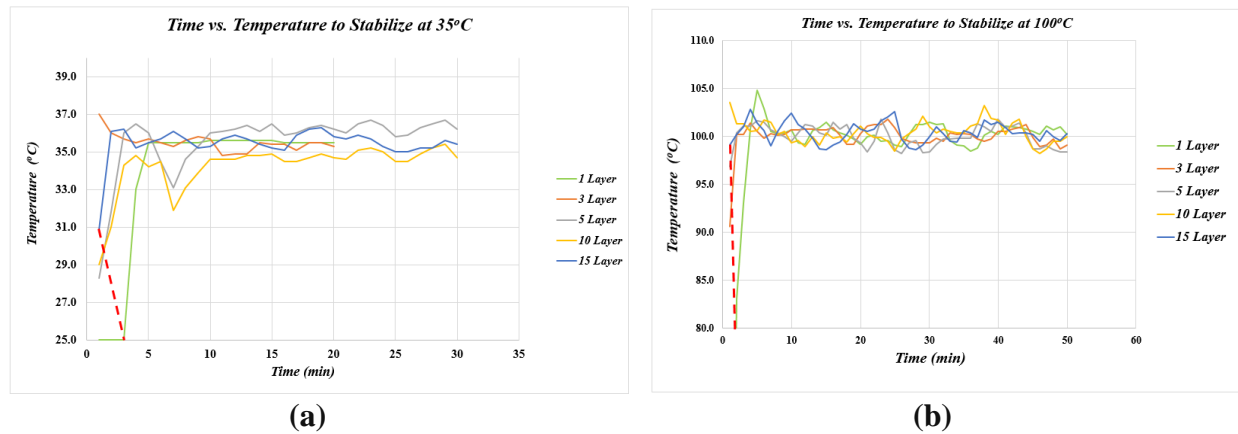


Figure 33 - Time vs. temperature to stabilize at (a) 35°C and (b) 100°C

Figure 33 shows that the H3S heating crystal maintained a sample heating profile that was approximately stable throughout the curing process after the initial ramp-up. A general trend of reduced time to achieve the desired sample temperature as a function of increasing number of sample layers was noted, which may reflect surface heat losses versus volume heating for the decreasing ratios of surface to volume as the number of layers increase.

These results demonstrated that the surface curing temperature was maintained to within a control window of $\pm 2^\circ\text{C}$ around 35°C. For our working distance and temperature the peak pulse energy of a nominal H3S system flash lamp is rated at 2000J and max average power of 6kW with a maximum supply voltage of 400V [117]. The control-stabilized supply voltages during the curing

cycles were in the range of 100-140V for all runs. In all cases, our curing process was carried out in ambient conditions without vacuum chambers or gas flows to provide a specific environment. The linear dependences of thickness and conductivity of the cured Ag provided a first indication that the sintered material is of common microstructure from sample to sample and over various thicknesses. This uniformity is highly desirable from the perspective of obtaining a repeatable process with reasonable yield. Figure 34 shows the cured samples stored in vacuum desiccator.

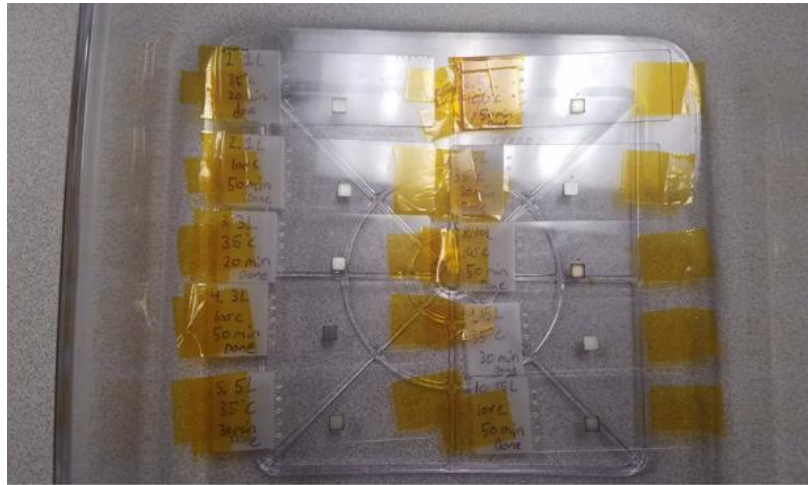


Figure 34 - Cured samples stored in vacuum desiccator

5.5 Layer Thickness Measurements

After sintering the samples, layer thickness measurements were carried out utilizing NanoMap 500LS from AEP technology. Figure 35 shows the system (a) and a sample measurement result for step height and R_a (b).

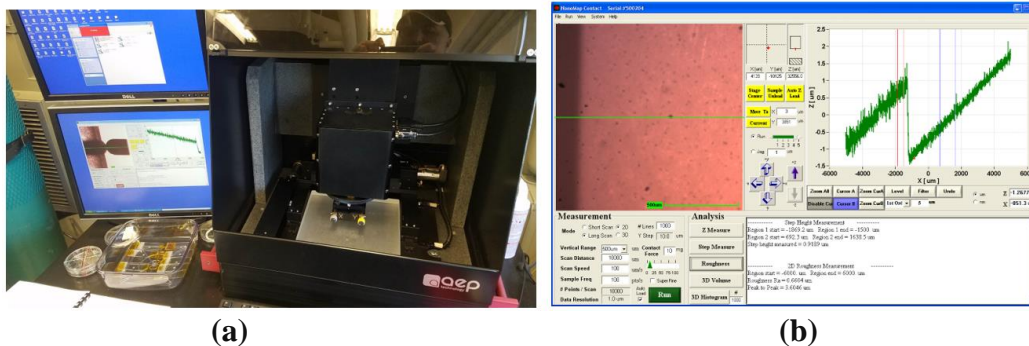


Figure 35 - (a) NanoMap 500LS from AEP Technology (b) Sample measurement result

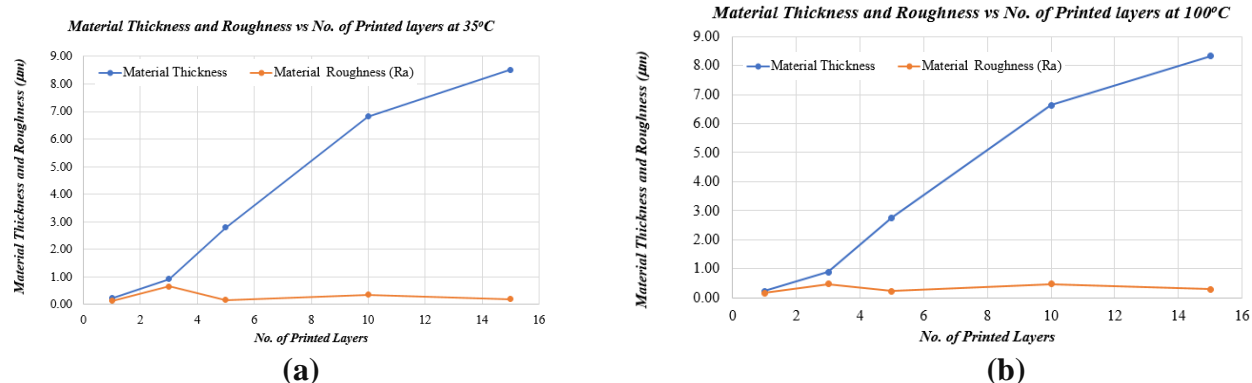


Figure 36 - Silver thickness and roughness vs No. of printed layers at (a) 35°C and (b) 100°C

Figure 36 shows material thickness and R_a vs number of printed layers, it is obvious that the more material added the thicker the layer will be. Also, it is clear that the material roughness is within the range of $0.13\mu\text{m}$ to $0.66\mu\text{m}$ which shows that the surface is smooth for all samples after sintering at 35°C when compared with the range of $0.16\mu\text{m}$ to $0.55\mu\text{m}$ after sintering at 100°C . The surface roughness uniformity was a first indication that the contact pads might have similar internal structures.

5.6 Conductivity Measurement

Following the process of finding the material thickness, the next step was to determine the silver ink conductivity. Resistivity measurements were carried out using the method described in Section 4.3.1 utilizing a 4-point probe. Results of the conductivity measurements and percentage of bulk silver conductivity at 35°C and 100°C are summarized as shown in Table 9 and Table 10 for the 10 samples.

<i>No. of Printed Layers</i>	<i>Material Thickness (t) (μm)</i>	<i>Material Roughness (Ra) (μm)</i>	<i>Conductivity (σ) (S/cm)</i>	<i>Percentage of Bulk Silver Conductivity (σ) (%)</i>
1	0.23	0.13	6.88×10^{-3}	1%
3	0.92	0.66	1.93×10^{-4}	3%
5	2.79	0.16	3.10×10^{-4}	5%
10	6.81	0.35	6.68×10^{-4}	11%
15	8.51	0.20	1.08×10^{-5}	17%

Table 9 - Conductivity and % of bulk silver conductivity measurement summary at 35°C

Figure 37 shows material resistivity (ρ) and conductivity (σ) vs number of printed layers at 35°C. The graph indicates that material conductivity increases with the increase of layers thickness. The best fit to the conductivity data was shown to be a linear equation. Resistivity showed a harmonic series behavior “power equation fit”($y = \frac{0.0002}{x^{1.012}}$).

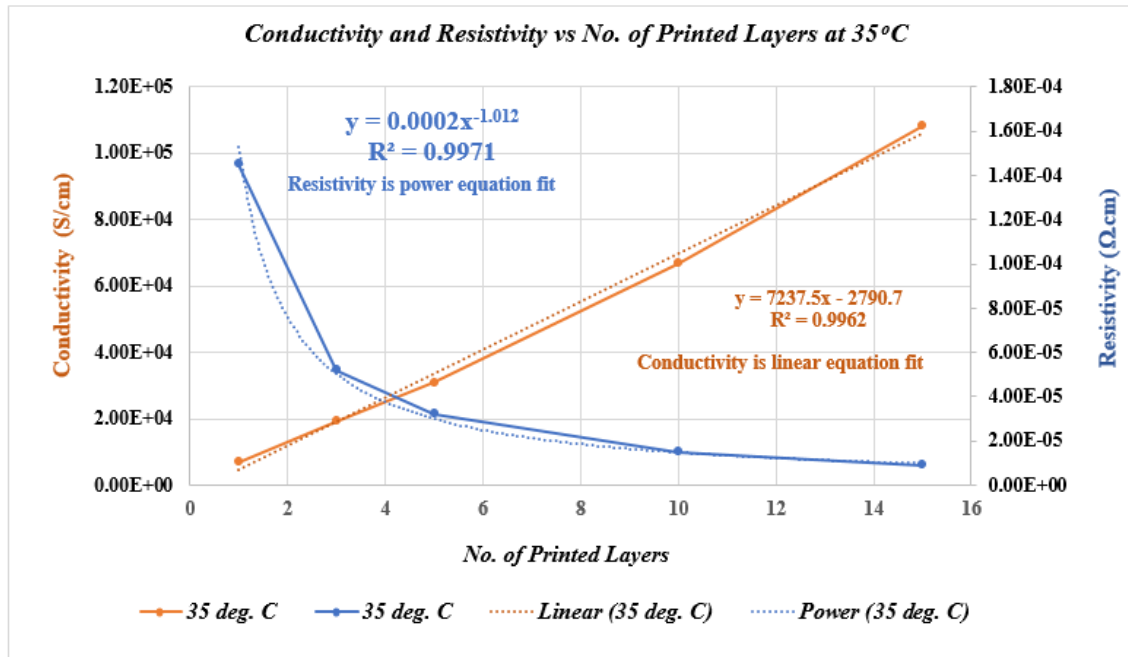


Figure 37 - Resistivity (ρ) and conductivity (σ) vs No. of printed layers at 35°C

No. of Printed Layers	Material Thickness (t) (μm)	Material Roughness (Ra) (μm)	Conductivity (σ) (S/cm)	Percentage of Bulk Silver Conductivity (σ) (%)
1	0.22	0.16	7.75×10^3	1%
3	0.88	0.47	2.02×10^4	3%
5	2.75	0.22	3.48×10^4	6%
10	6.64	0.47	7.58×10^4	12%
15	8.32	0.29	1.14×10^5	18%

Table 10 - Conductivity and % of bulk silver conductivity measurement summary at 100°C

Figure 38 shows material resistivity (ρ) and conductivity (σ) vs number of printed layers at 100°C, it is evident that the thicker the material the lower the resistivity becomes linearly as would be expected. Also, the graph proves that the material conductivity increases with the increase of layers thickness. Following the curve fitting results, it is clear that the conductivity follows a linear equation path while resistivity tends to be a harmonic series “power equation fit” ($y = \frac{0.0001}{x^{1.004}}$).

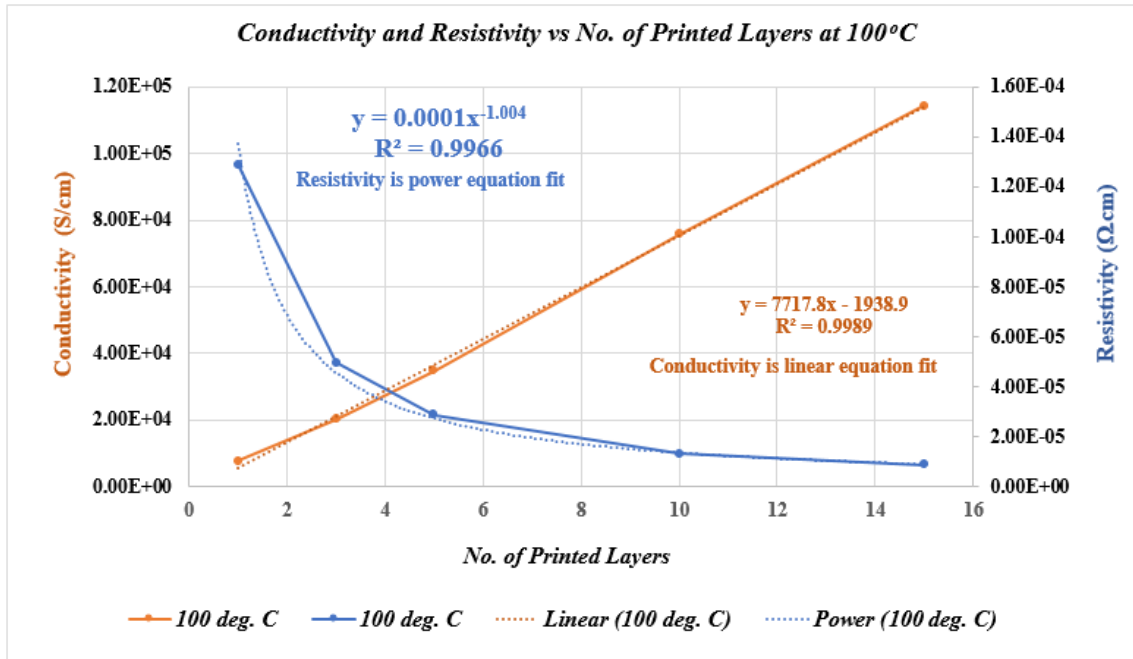


Figure 38 - Resistivity (ρ) and conductivity (σ) vs No. of printed layers at 100°C

5.7 Summary of Fabrication vs Conductivity

Table 9 and Table 10 confirm that the thicker the material the higher the conductivity. It also shows that the H3S optical curing system can be used with organic materials that cannot handle higher temperatures for longer periods of time. As noted from the results, we can achieve 17-18% of bulk silver conductivity with 50 minutes of curing time of 15 layer contact pads. This makes the pulsed optical curing method a good candidate for curing the contacts of OLED and TPV devices that can handle up to as much as 150°C for shorter periods of time without degrading the organic material. We also demonstrated that the conductivity is linear with a slight bow and the resistivity is a harmonic series of form $y = \frac{1}{x}$, where x is the conductivity.

Figure 39 (a) reproduces the graph of % of bulk silver conductivity for best-case thermally cured silver ink with ~70% of Ag bulk conductivity that was obtained under long-duration, high-temperature conditions (a) [13]. Figure 39 (b) shows the graph of % of bulk silver conductivity for optically cured samples at 35°C and 100°C with just under 20% of Ag bulk conductivity. Graph (b) clearly shows that the two temperature profiles have the same dependence on the material thickness. This suggests that low temperature optical curing at 35°C will produce results that are as good as those obtained using the 100°C condition. If this result can be further substantiated, it will strongly support OLED fabrication using low-temperature optical curing as the method of choice.

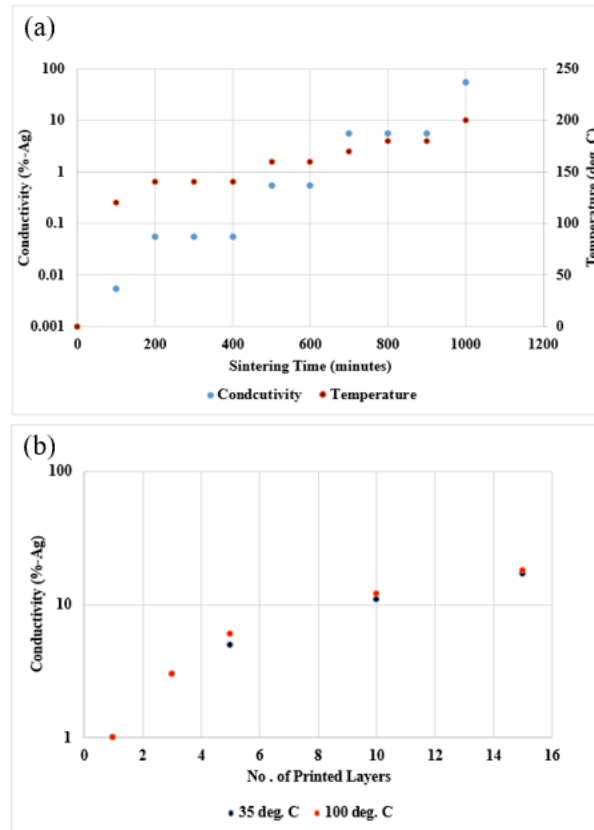


Figure 39 - Conductivity as %-Ag conductivity for (a) Thermally cured (b) Optically cured at 35°C and 100°C

(Image (a) reproduced with permission from [13].)

5.8 Silver Contact Uniformity Using SEM

The JEOL JSM-7500F SEM system at Michigan State University was utilized to investigate the material properties of the cured silver ink samples. The original goal was to accurately measure material thickness and check for material uniformity. A first series of investigations, performed in September 2019, demonstrated that all time, temperature and number of layers growth conditions produced similar films of nanocrystalline morphology. Subsequent to the electrical conductivity investigations, it was decided to perform a second series of SEM investigations that included composition analysis by EDS to examine whether residual ink binder could account for the lower conductivities observed for the optically versus thermally cured contact pads on identical glass substrates shown in Figure 39.

EDS was used to assess the film local chemistries by atomic percent in after extended storage. Between the first and second SEM investigations, the films were stored in a glass desiccator at the Center for Advanced Microscopy under non-vacuum conditions. The samples were thus exposed to the standard desiccant, W. A. Hammond Drierite™ (Thermo Fisher Scientific, Waltham, MA) for ~20 months. The chemical composition of Drierite™ is calcium sulfate with a cobalt chloride indicator. By accident, additional information was gained about required storage conditions for 3D printed silver ink electronics as well as first-time information about Ag film composition under optical curing, which influences its electrical conductivity. As shown in this chapter, EDS demonstrated that, initially, the films were almost certainly silver oxide without any residual binder. Silver oxide can be used as a powerful precipitating reagent for even trace amounts of chlorine [118]. After 20 months storage, silver chloride nanocrystallites also formed, although regions of silver oxide nanocrystalline film were still intact.

This chapter presents a quantitative investigation of film morphologies, grain sizes and silver oxide chemistries, concluding with an analysis of the correlation between allowed oxide chemistries and electrical conductivity.

5.9 Sample Preparation for SEM

The following steps were performed to prepare the silver ink samples for the SEM process:

- Using diamond scribe, score the middle of the silver ink square on the back side.
- Dip the substrate in liquid Nitrogen for 1 min to help break the sample smoothly.
- Fracture the sample.
- Using Aluminum stubs, mount the samples 90° on the stub using epoxy glue (Figure 40 (a)).
- Let the epoxy dry for 12 hours.

- Coat the samples with Osmium for 10 to 14 seconds (Figure 40 (b)).
- Load the samples to JEOL JSM-7500F SEM and check for material uniformity and measure material thickness (Figure 40 (c)).



(a)

(b)

(c)

Figure 40 - (a) Samples 2 and 4 mounted on aluminum stub (b) Pure osmium coater Neoc-AN (c) JEOL JSM-7500F SEM

5.10 Initial Material Uniformity Investigations with Film Thickness Measurements

Material uniformity investigations were carried out utilizing JEOL JSM-7500 SEM in 2019. Film thicknesses for individual images were evaluated at the same time and used to corroborate the NanoMap 500 LS profiler results. Figure 41 and Figure 42 show the SEM results for the samples sintered at 35°C and 100°C using the light-pulse system. Interestingly, freeze fracture using liquid nitrogen to obtain cross-sections proved difficult due to the films' mechanical strength. Artifacts where the films have stretched and curled after breaking may be observed in several of the SEM images.

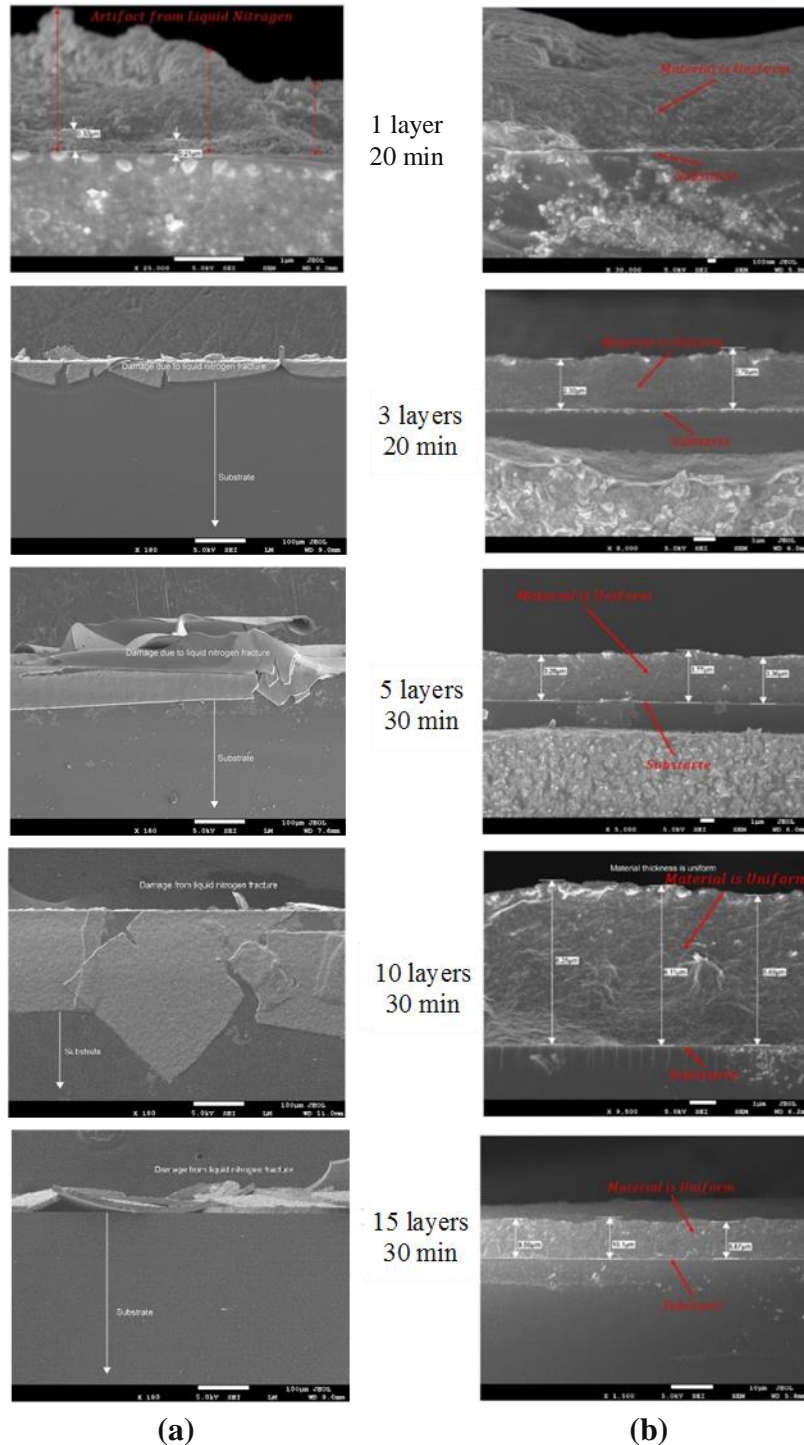


Figure 41 - SEM micrographs of cross-sections of printed silver regions after light-pulse sintering at 35°C with the number of printed layers and sintering times indicated for each row. Column (a) shows the broad scan of the cross-section samples, including the damage from the liquid nitrogen fracture process used for preparation. Column (b) shows that the regions of printed silver are uniform across the micron scale.

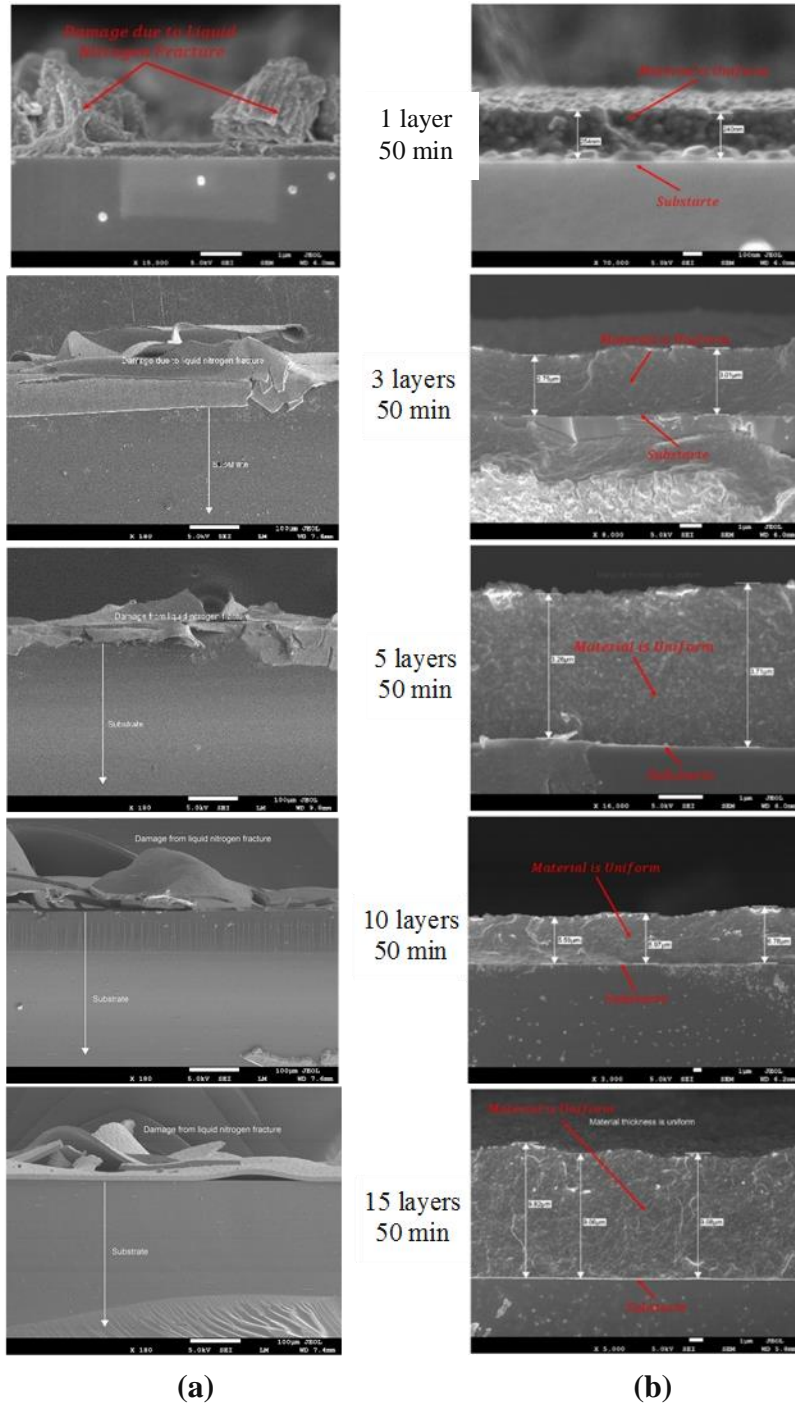


Figure 42 - SEM micrographs of cross-sections of printed silver regions after light-pulse sintering at 100°C with the number of printed layers and sintering times indicated for each row. Column (a) shows the broad scan of the cross-section samples, including the damage from the liquid nitrogen fracture process used for preparation. Column (b) shows that the regions of printed silver are uniform across the micron scale.

Comparisons between material thickness measured with the NanoMap 500LS and SEM are summarized in Table 11 and plotted together in Figure 43. The SEM results corroborated the profiler results.

No. of Printed Layers	Sintering Temperature (°C)	Sintering Time (Minutes)	Material Thickness (μm) Using NanoMap 500LS	Material Thickness (μm) Using SEM
1	35	20	0.23	0.27
1	100	50	0.22	0.25
3	35	20	0.92	2.55
3	100	50	0.88	2.88
5	35	30	2.79	3.46
5	100	50	2.75	3.49
10	35	30	6.81	6.02
10	100	50	6.64	6.11
15	35	30	8.51	9.51
15	100	50	8.32	9.32

Table 11 - Material thickness comparison between NanoMap 500LS and SEM

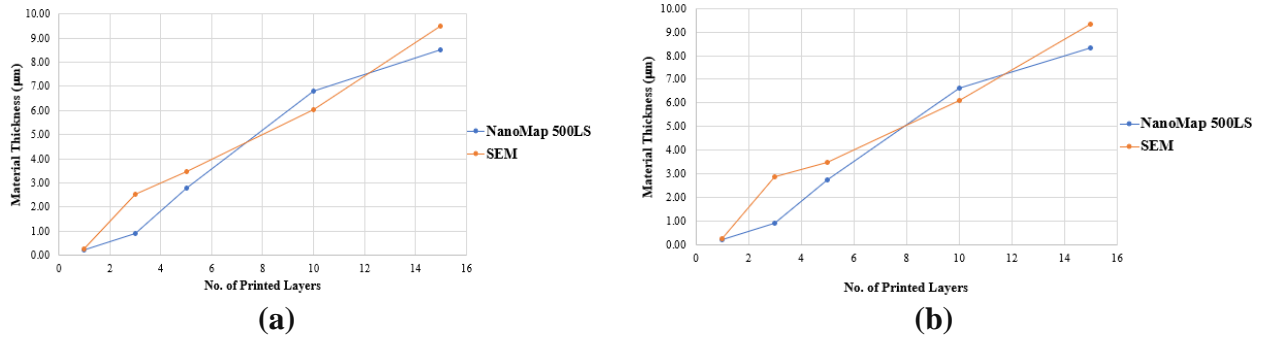


Figure 43 - Material thickness after (a) 35°C and (b) 100°C curing using NanoMap and SEM

5.11 Summary of Initial Thickness Investigations

In order to understand the uniformity of the cured Ag, we have performed cross-sectional SEM analysis. All sets of the micrographs are shown in Figure 41 and Figure 42. We see several features of importance from these. In all cases, there is no striation of the print after curing, which indicates that the curing process is happening throughout the thickness of the Ag ink to form a continuous layer. This is in contrast to layer by layer curing, for example laser curing in situ with printing, which frequently gives rise to clearly defined layers with interfaces between layer prints. We also see that the interface with the substrate is clean. This indicates that we are able to cure through our thickest layers without creating voids or blisters at the substrate from out-gassing of

the ink solvent. This is a direct result of heating from the top surface to maintain curing conditions. Long bake processes tend to cause severe issues for thick prints, which is one reason to cure layer by layer with either thermal cycles or lasers. The last feature we point out is that the morphology of the cured Ag is uniform for all thicknesses and shows no coarse features or visible inhomogeneities at this magnification. As part of the SEM study, we also checked specific locations for cured Ag thickness as measured during microscopy. Our finding was that our profilometer average thickness readings were representative of the thicknesses taken from our specific cross-sectional images.

5.12 Nanocrystalline Morphology and Grain Size Investigation

In addition to their uniformity, the films displayed an apparent nanocrystalline morphology for all curing time and temperature conditions. Using SEM images taken after curing and after 20 months in storage exposed to air, a grain size investigation was performed to quantify this observation. After storage, based on EDS data discussed in detail below, silver chloride nanocrystallites also formed although regions of silver oxide nanocrystalline film were still intact. The intact silver oxide film regions were used for grain size measurements and compared with those evaluated directly after curing.

Figure 44 shows the SEM measurements for the 1-layer sample sintered at 35°C for 20 minutes that were carried out for post curing (a) and (c) and for post storage (b) and (d). The yellow arrow in (b) marks an intact film region. This region is used for the grain size analysis in the next section of this chapter. The grain sizes were collected from the processed images of the other samples and that data is compiled in Appendix A.

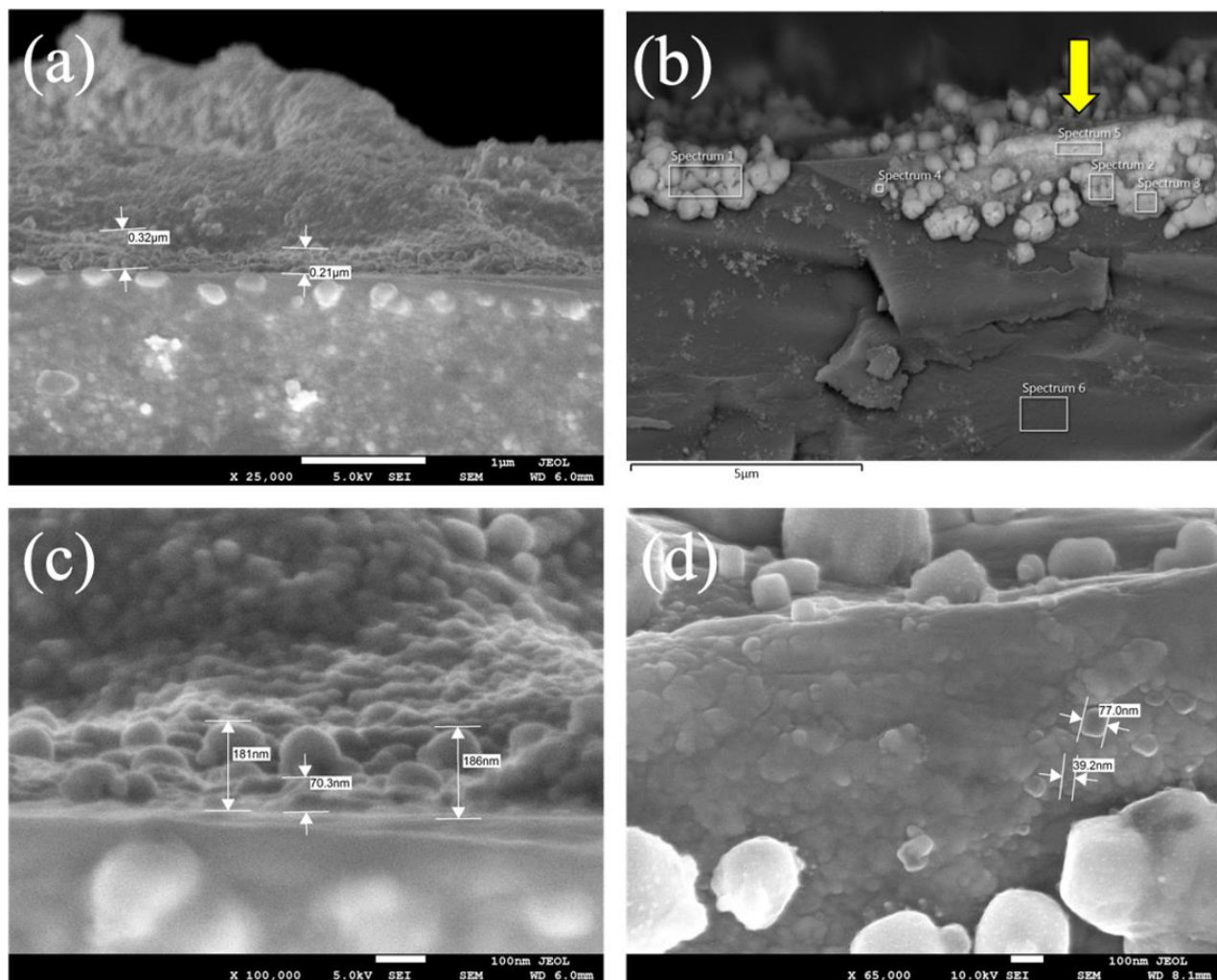


Figure 44 - Post curing SEM measurement for 1-layer sample sintered at: (a) and (c) 35°C for 20 minutes. (b) and (d): Post storage SEM measurement

Figure 45 shows the SEM measurements for the 1-layer sample sintered at 100°C for 50 minutes that were carried out for post curing (a) and (c) and for post storage (b) and (d). No intact silver oxide film regions were found during the post storage investigations as shown in (d).

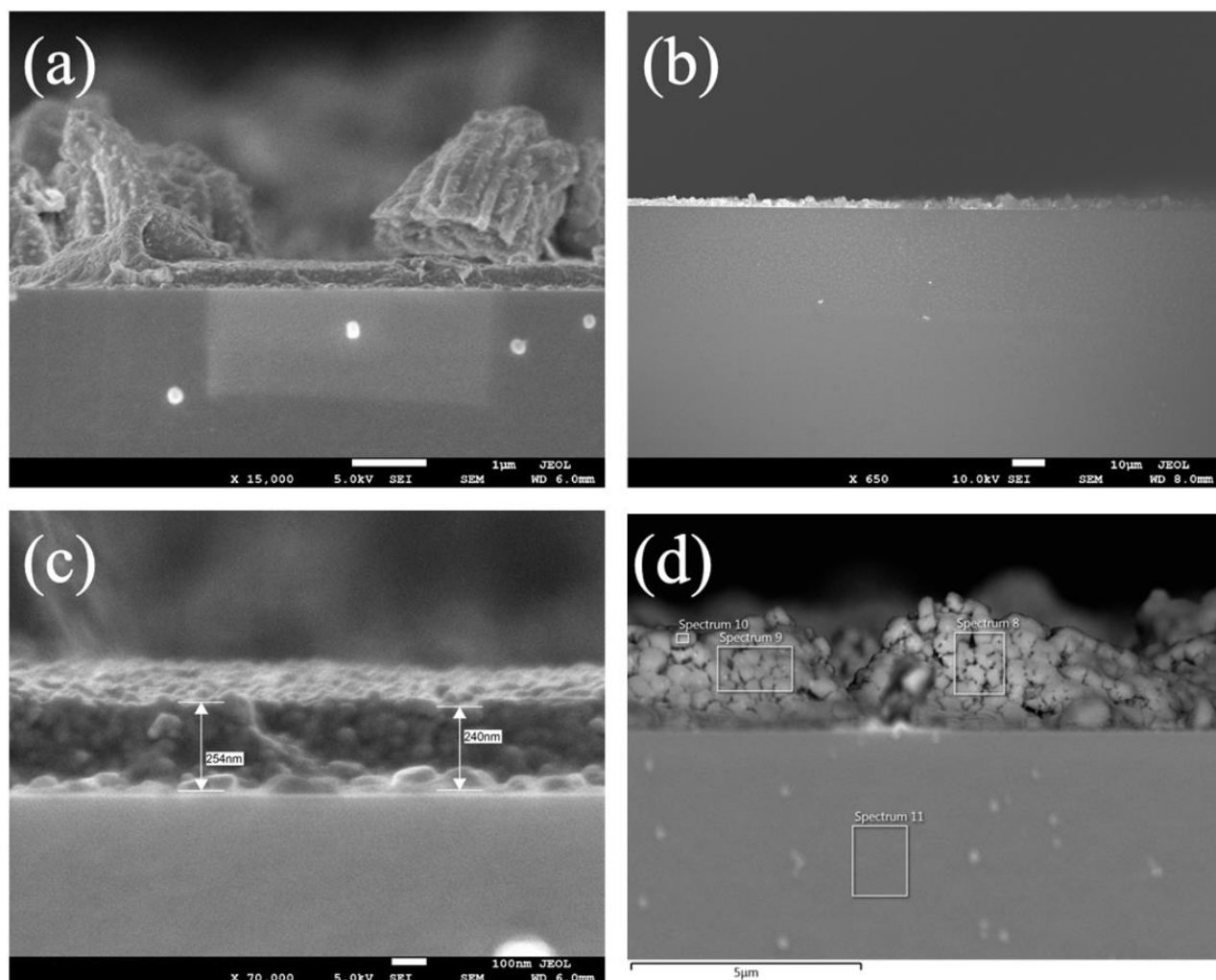


Figure 45 - Post curing SEM measurement for 1-layer sample sintered at: (a) and (c) 100°C for 50 minutes. (b) and (d): Post storage SEM measurement

Figure 46 shows the SEM measurements for the 3-layer sample sintered at 35°C for 30 minutes (a) and 3-layer sample sintered at 100°C for 50 minutes (c) that were carried out for post curing and for post storage (b), (d) and (e). The image in (e) is included as a good close-up that shows the silver oxide nanocrystalline film regions, the larger silver chloride nanocrystallites and the glass substrate clearly.

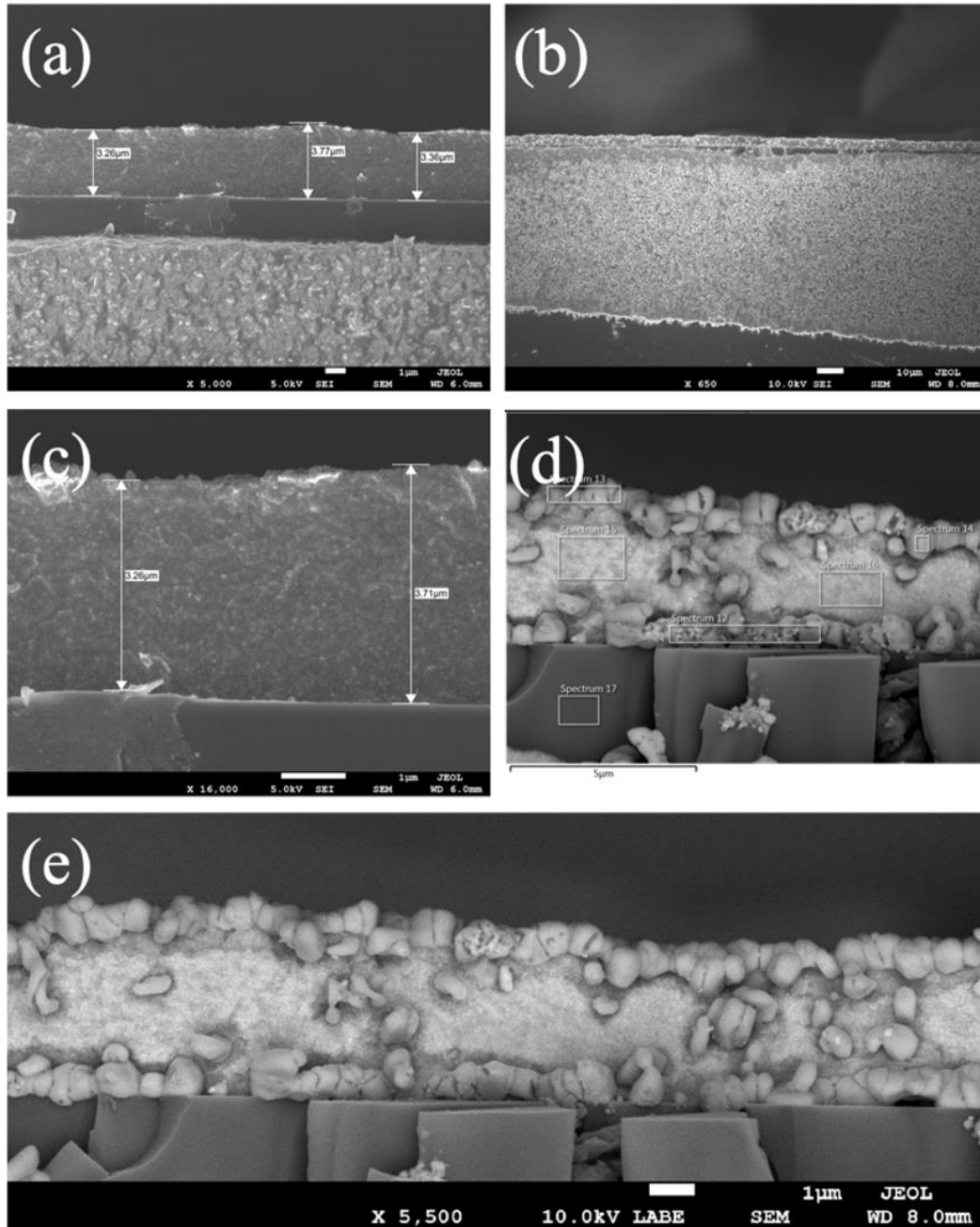


Figure 46 - Post curing SEM measurement for 3-layer sample sintered at: (a) 35°C for 30 minutes (c) 100°C for 50 minutes. (b), (d) and (e): Post storage SEM measurement

Figure 47 shows the SEM measurements for the 5-layer sample sintered at 35°C for 30 minutes that were carried out for post curing (a) and (c) and for post storage (b) and (d). Image (d) shows the damage to both the film and the substrate due to freeze fracture.

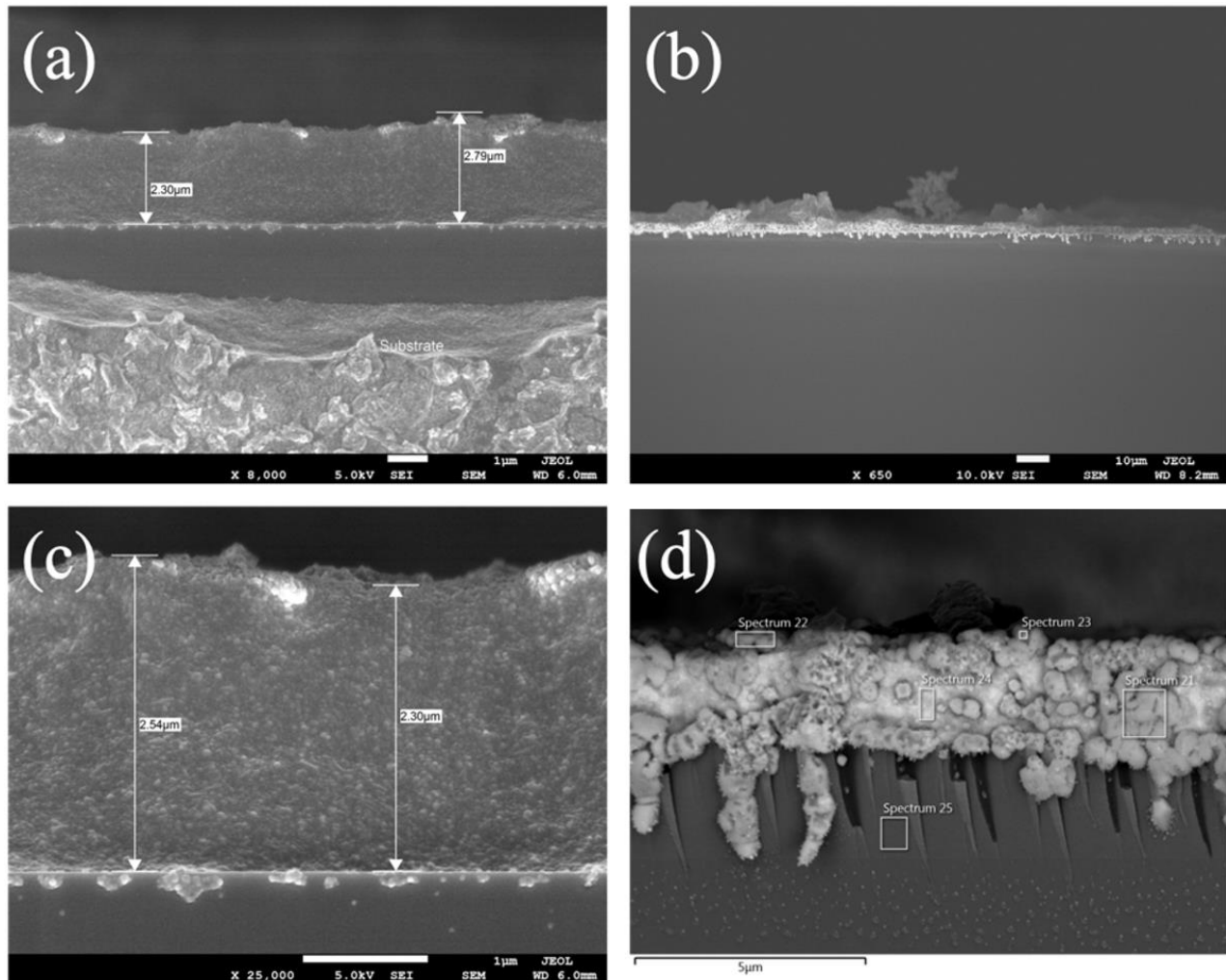


Figure 47 - Post curing SEM measurement for 5-layer sample sintered at: (a) and (c) 35°C for 30 minutes. (b) and (d): Post storage SEM measurement

Figure 48 shows the SEM measurements for the 5-layer sample sintered at 100°C for 50 minutes that were carried out for post curing (a) and (c) and for post storage (b) and (d). Although the film is thicker, no differences in morphologies are observed.

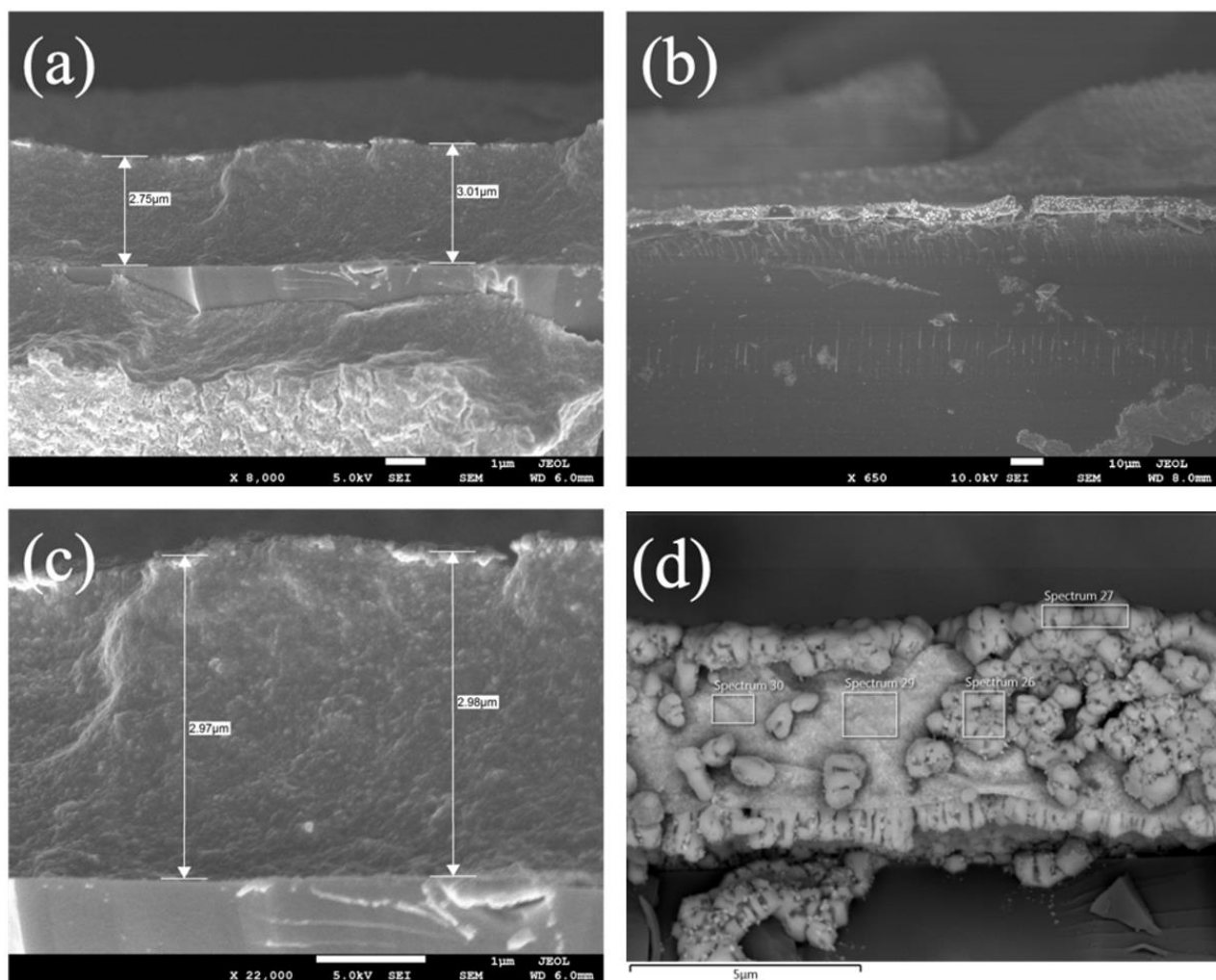


Figure 48 - Post curing SEM measurement for 5-Layer sample sintered at: (a) and (c) 100°C for 50 minutes. (b) and (d): Post storage SEM measurement

Figure 49 shows the SEM measurements for the 10-layer sample sintered at 35°C for 30 minutes (a) and 10-layer sample sintered at 100°C for 50 minutes (c) that were carried out for post curing and for post storage (b) and (d).

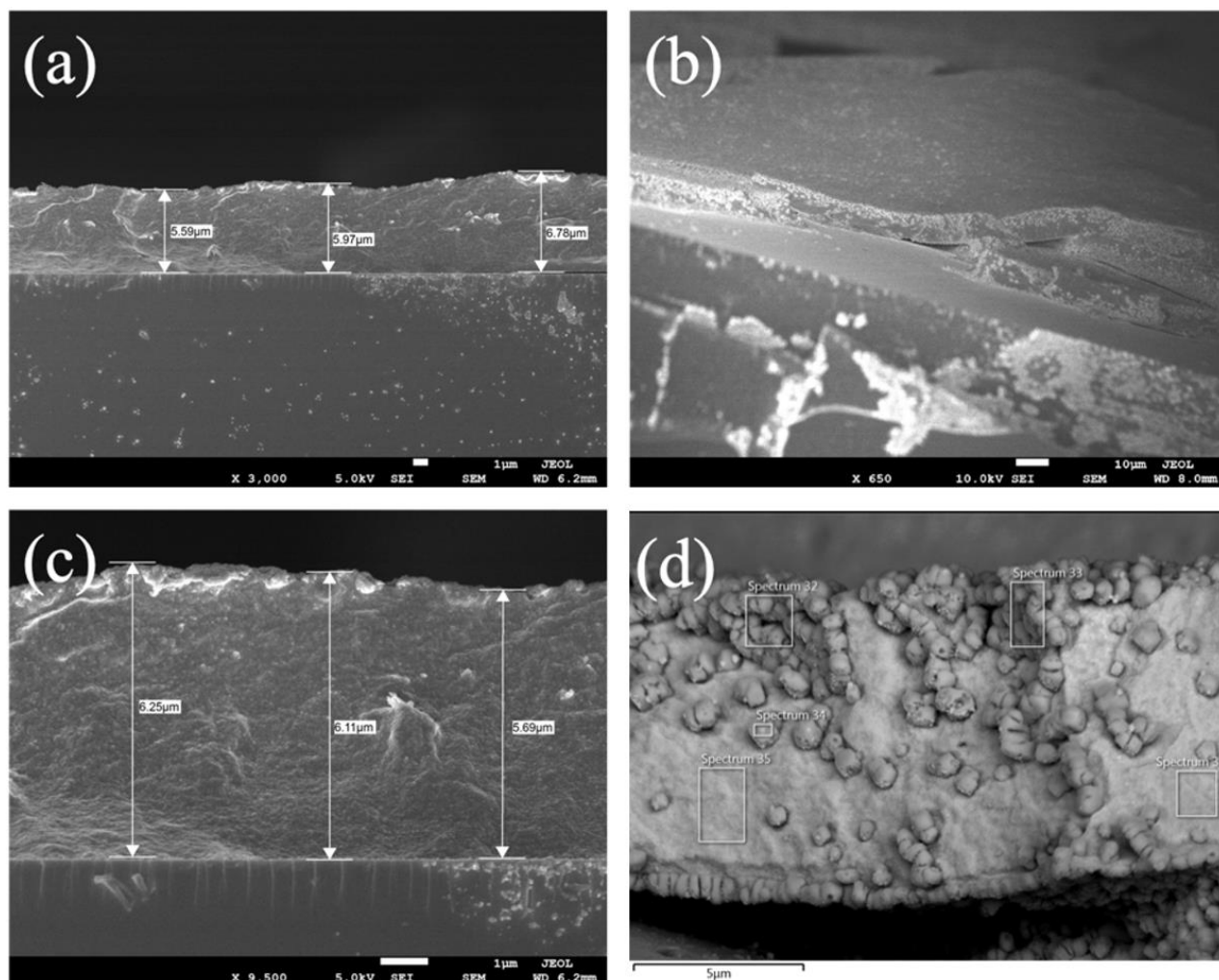


Figure 49 - Post curing SEM measurement for 10-layer sample sintered at: (a) 35°C for 30 minutes (c) 100°C for 50 minutes. (b) and (d): Post storage SEM measurement

Figure 50 shows the SEM measurements for the 15-layer sample: (a) damage due to liquid nitrogen fracture and sample sintered at 35°C for 30 minutes (c) that were carried out for post curing and for post storage (b) and (d). Film resistance to freeze fracture is again apparent.

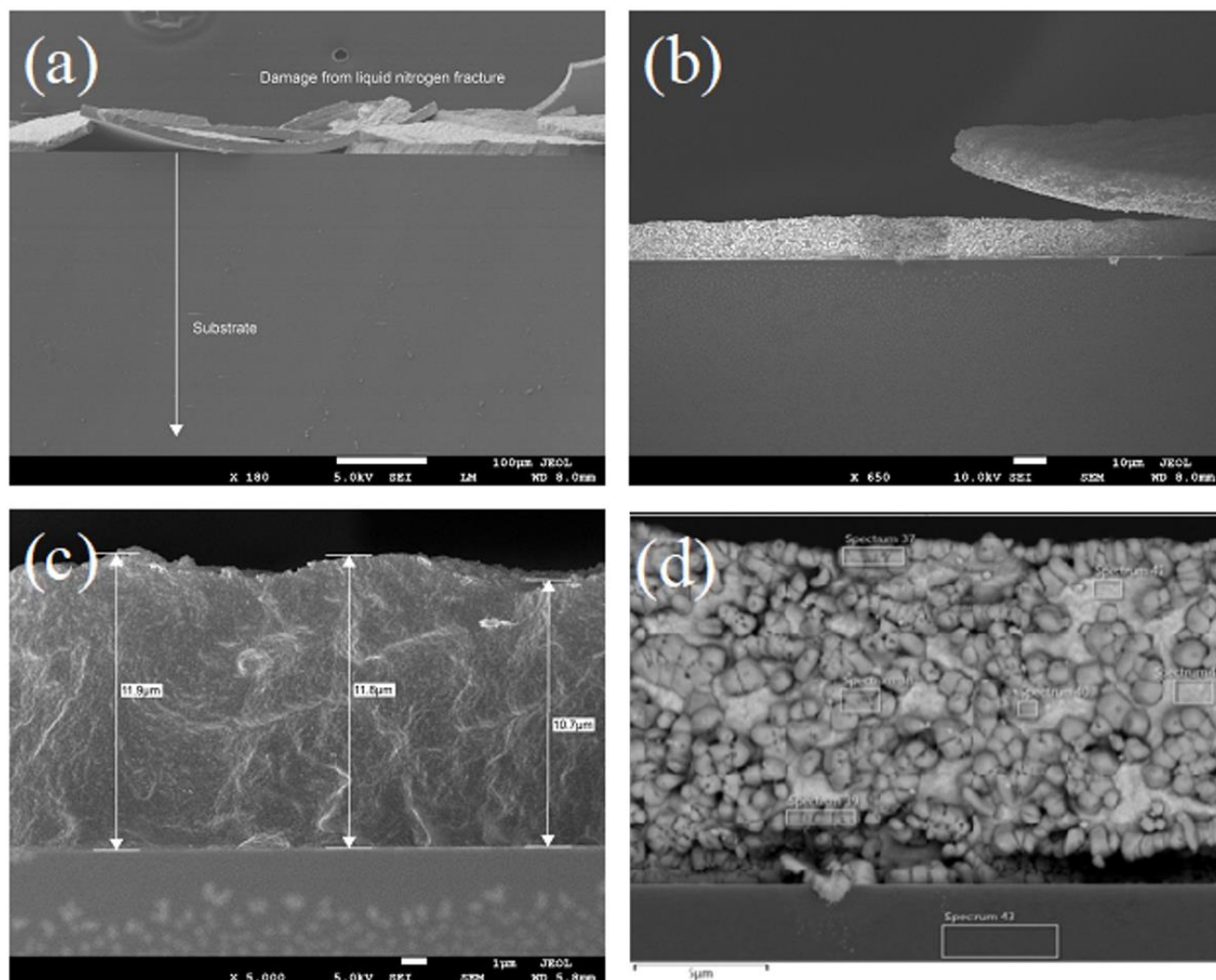


Figure 50 - Post curing SEM measurement for 15-layer sample: (a) Damage due to liquid nitrogen fracture (c) sample sintered at 35°C for 30 minutes. (b) and (d): Post storage SEM measurement

Figure 51 shows the SEM measurements for the 15-layer sample: (a) damage due to liquid nitrogen fracture and sample sintered at 100°C for 50 minutes (c) that were carried out for post curing and for post storage (b) and (d). Film resistance to freeze fracture is again apparent.

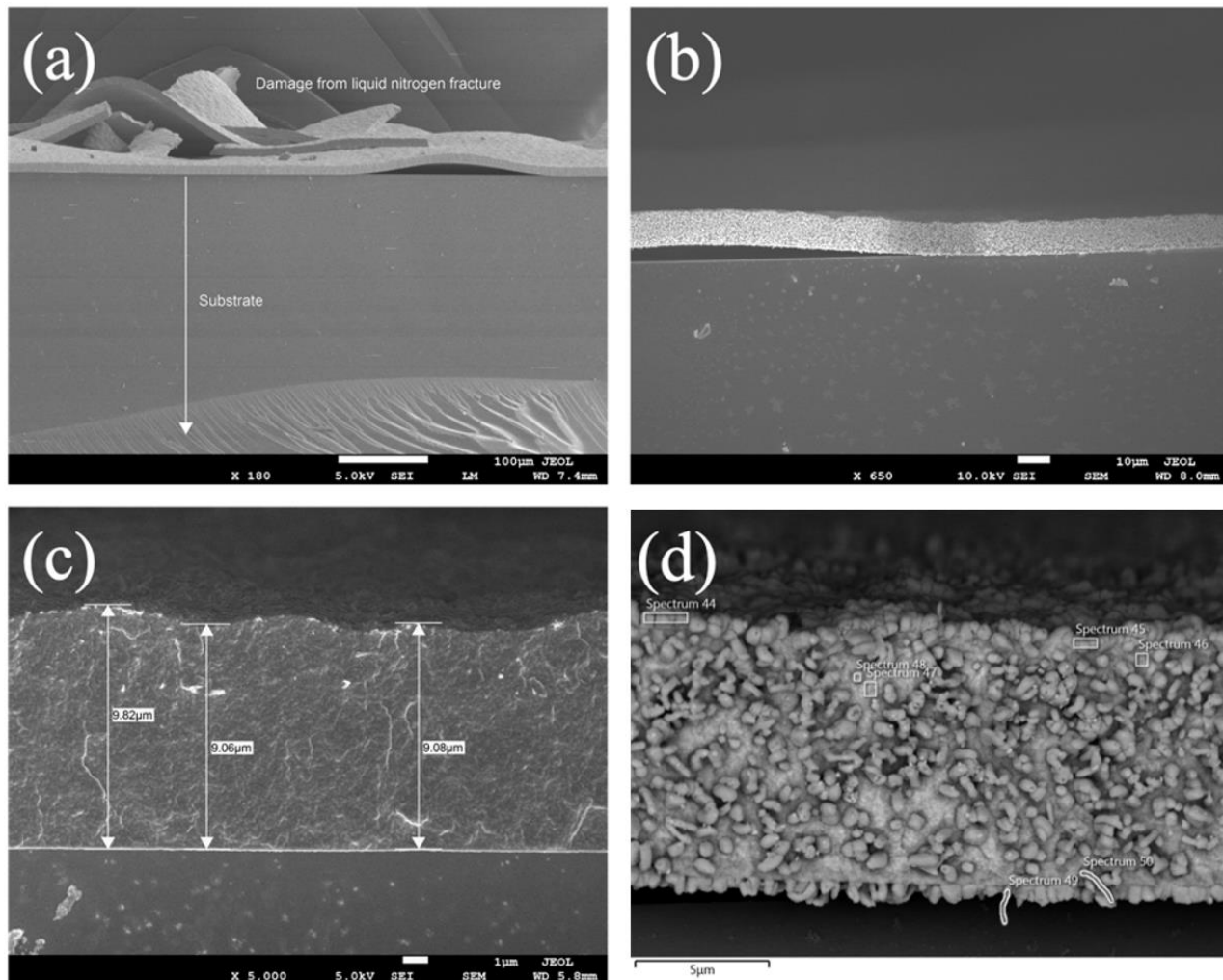


Figure 51 - Post curing SEM measurement for 15-layer sample: (a) Damage due to liquid nitrogen fracture (c) sample sintered at 100°C for 50 minutes. (b) and (d): Post storage SEM measurement

5.13 Grain Size Analysis

In this section we demonstrate that the silver oxide nanocrystalline film grain sizes remained comparable from post curing to post storage. We utilized NIH ImageJ software [68] to measure the grain size in each SEM image with sufficient resolution. This included almost all of the post storage images and many of the post curing images.

5.13.1 Sample Calculation

A detailed analysis for the 1-Layer sample that was cured at 35°C for 20 minutes is shown in this chapter with all other results given in Appendix A. Table 12 shows the results from 5 grain

samples that were measured on the 1-layer silver ink thin film post curing and another 5 grain structures as measured after storage. We calculated the average size, standard deviation, and standard error of the mean (S.E.M) using the processed images. Figure 52 shows the plotted grain dimension data and the processed images used for obtaining the measurements.

Grain	Length (nm)	Average	Standard Deviation	S.E.M
1	53.70	70.44	14.00	6.26
2	64.12			
3	67.84			
4	70.55			
5	96.01			
	352.22			

(a)

Grain	Length (nm)	Average	Standard Deviation	S.E.M
1	43.49	63.96	18.60	8.32
2	45.00			
3	61.29			
4	79.64			
5	90.39			
	319.81			

(b)

Table 12 - Average, standard deviation and S.E.M calculations for 5 imaged Ag grains in 1-layer printed Ag (a) post curing and (b) post storage.

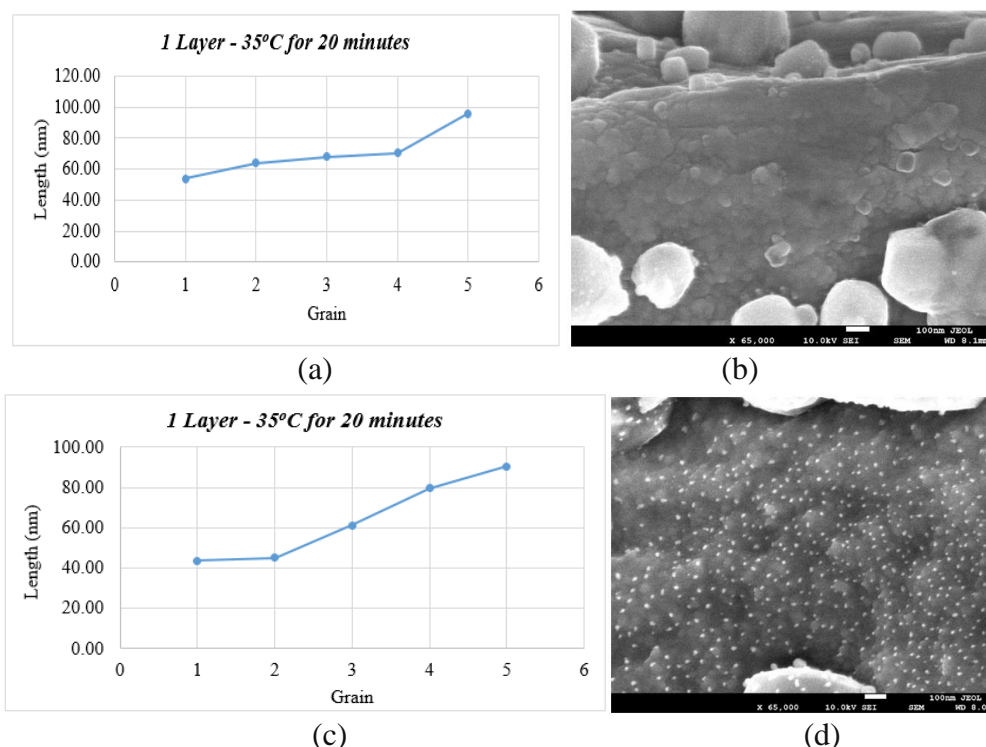


Figure 52 - Measured grain dimensions and the processed SEM images from which they were extracted for the 1-layer printed Ag (a,b) post curing and (c,d) after storage, respectively.

As we notice from the two measurements, the difference between the initial curing and after storage grain size is quite small (~6nm) which shows that the grain size didn't change during

the storage period of ~20 months. Based on this result, we assume that the film composition investigations performed after storage are representative.

5.13.2 Analysis of Grain Uniformity

Table 13 shows the conductive volume (Φ_{solid}) for the printed layers that were cured at 35°C and 100°C. The conductive volume calculations were based on Maxwell's effective medium theory (EMT) due to the high-density silver ink NPs, the conductive volume [119] can be written as shown in formula (6):

$$\Phi_{solid} = \frac{3\sigma_{eff,EMT}}{2\sigma_{metal} + \sigma_{eff,EMT}} \quad (6)$$

where $\sigma_{eff,EMT}$ is the effective conductivity silver ink in (S/cm) and σ_{metal} is the bulk conductivity of metallic Ag phase (6.3×10^5 S/cm for silver).

No. of Printed Layers	35 ^{deg} C				100 ^{deg} C			
	Resistivity (ρ) (Ω .cm)	Conductivity (σ) (S/cm)	Percentage of Bulk Silver Conductivity (σ) (%)	Conductive Volume Φ_{solid}	Resistivity (ρ) (Ω .cm)	Conductivity (σ) (S/cm)	Percentage of Bulk Silver Conductivity (σ) (%)	Conductive Volume Φ_{solid}
1	1.45E-04	6.88E+03	1	0.015	1.29E-04	7.75E+03	1	0.015
3	5.19E-05	1.93E+04	3	0.044	4.95E-05	2.02E+04	3	0.044
5	3.23E-05	3.10E+04	5	0.073	2.87E-05	3.48E+04	6	0.087
10	1.50E-05	6.68E+04	11	0.156	1.32E-05	7.58E+04	12	0.170
15	9.24E-06	1.08E+05	17	0.235	8.76E-06	1.14E+05	18	0.248

Table 13 - Conductive volume calculations.

Table 13 clearly shows that the thin films become more silver dense with print thickness. We conclude there is less oxidation in the volume for thicker films. Figure 53 shows a graphical representation of the grain size measurement for the post storage samples with S.E.M values depicted on the histogram.

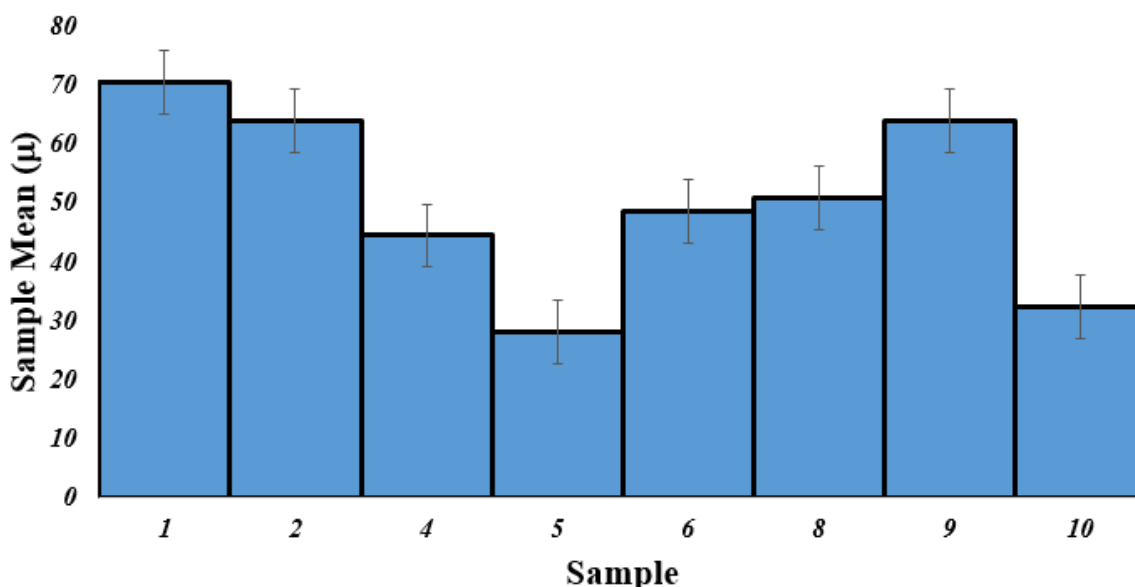


Figure 53 - Grain size measurement histogram for printed films post storage.

5.14 Film Composition by EDS Analysis

EDS was performed in the areas identified by the white boxes in the post storage SEM images shown in Figure 44 - Figure 51. The strategy was to take several measurements each of the nanocrystalline film regions, larger nanocrystallites, and substrate. These three features proved to have distinct chemical identities and stoichiometries. At the experimental accelerating voltages of 10 kV or above, x-ray penetration into the film cross sections extended $\sim 1\text{-}2\ \mu\text{m}$, and interrogated many unit cells' worth of material. Therefore, these were volume rather than surface measurements.

Figure 54 summarizes the atomic percentages of silver (Ag), oxygen (O), chlorine (Cl), silicon (Si) and other elements in the nanocrystalline film regions (a), larger nanocrystallites (b) and substrate (c). The nanocrystalline film regions were shown to be Ag-O with an $\sim 1:1$ stoichiometry. 'Other' was a mixture of trace elements that did not show any evidence of a strong organic (carbon) binder component. This was also the case for the larger nanocrystallites and the substrate. The larger nanocrystallites were shown to be Ag-O-Cl with an $\sim 3:2:1$ stoichiometry.

The substrate was shown to be unambiguously glass, as expected. The ~1:2 stoichiometry for Si: (Oxygen + Other) is consistent with amorphous SiO₂ glass plus trace elements. At this point, we can observe the following:

- (1) The morphologies of films and remnant films are nanocrystalline both before and after the exposure to chlorine and as a function of layer thickness even before the exposure to chlorine.
- (2) The grain size of nanocrystallites in the films have the same mean value both before and after the exposure to chlorine and as a function of layer thickness even before the exposure to chlorine.
- (3) Based on (1) and (2), we assume that EDS on the remnant films provides accurate stoichiometric information about the original as-deposited films, which implies that these films are Ag and O. Atomic % stoichiometry shown as average + S.E.M. is close to 1:1 for Ag:O.
- (4) We serendipitously gained information about required storage conditions and have investigated the formation of silver chloride nanocrystallites whose material composition is in an ~3:2:1 ratio of Ag:O:Cl.
- (5) We draw the conclusion that the original hypothesis, that the reduced conductivity observed for the optically cured films was caused by organic (carbon) binder retention, has been ruled out. We now investigate the hypothesis that the observed conductivity differences may be due to differences in boundaries.

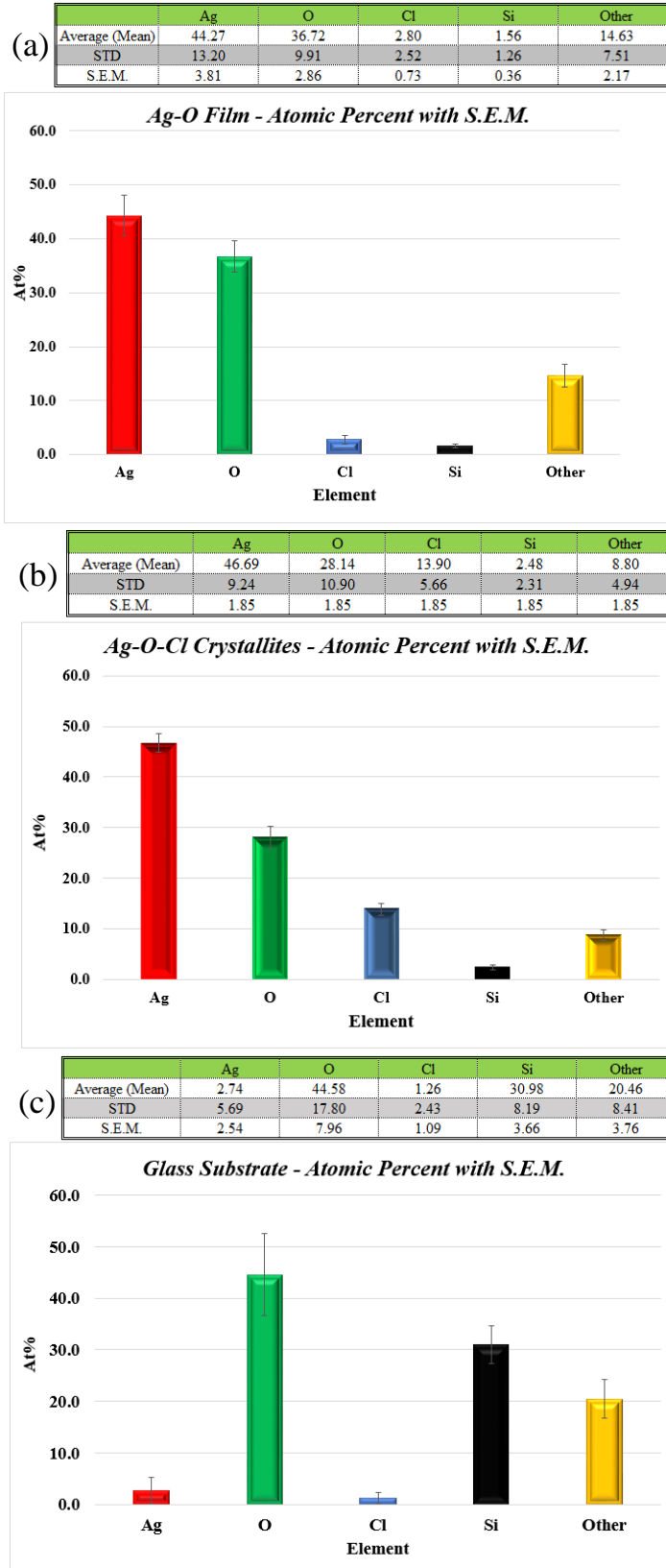


Figure 54 - (a) Ag-O film (b) Ag-O-Cl Crystallites (c) Glass substrate

5.15 Grain Boundary Analysis

Three key features of the optically cured films that were true for all growth conditions are: (1) nanocrystalline films with many grain boundaries, (2) densely packed films, and (3) films that contained a significant volumetric oxygen component. One could guess from the nearly equal Ag and O distribution in the EDS stoichiometry investigation of the remnant films that the films must be Silver(I,III) Oxide (known interchangeably in the literature as AgO and Ag₄O₄), which is moderately conductive. However, this hypothesis cannot reconcile a difference in conductivity per curing conditions with the persistently unchanged morphology observed during multiple types of investigations. Also, the Clariant product is described as a silver particle ink. If it was primarily a silver oxide ink, this would be widely known in the AJP community.

The ~1:1 Ag:O stoichiometry that was maintained for all layer thicknesses suggests that a substantial oxide component was located at the grain boundaries; otherwise the surface oxygen % would stay the same while the volume % of Ag increased. This is also consistent with exposure of the Ag nanoparticles to a uniform and largely aqueous suspension medium. We therefore investigate the consequences of assuming that the observed linear conductivity as a function of increasing number of layers results from nanocrystalline silver grains with an oxide at the grain boundaries.

Possible oxides include: Ag₂O, Ag₂O₃, AgO (Ag₄O₄), and AgO₂. All of these can have a cubic crystal structure compatible with the most common form of pure silver. The lattice mismatches compared to 2.942 Å for pure cubic Ag are shown in Table 14 [120].

	MaterialsProject.org ID	Lattice Constant (Å)	% Mismatch
Ag	mp-124	2.942	
Ag ₂ O	mp-353	4.841	0.65
Ag ₂ O ₃	mp-11872	5.107	0.74
AgO (Ag ₄ O ₄)	mp-8222	3.583	0.22
AgO ₂	mp-1214896	4.612	0.57

Table 14 - Lattice mismatch compared to 2.942 Å for pure cubic Ag.

Due to lattice mismatch, it is unlikely that any oxide forms a uniform coverage. It is impossible to say, without further investigation, whether one or multiple oxide forms were responsible for the observed Ag-O stoichiometry. Both Ag₂O [121] and AgO have appeared in silver NP literature. Ag₂O will be used in the following discussion.

From high-resolution SEMs such as the representative images shown in Figure 55, a rough estimate for the grain boundary width is given as 10nm.

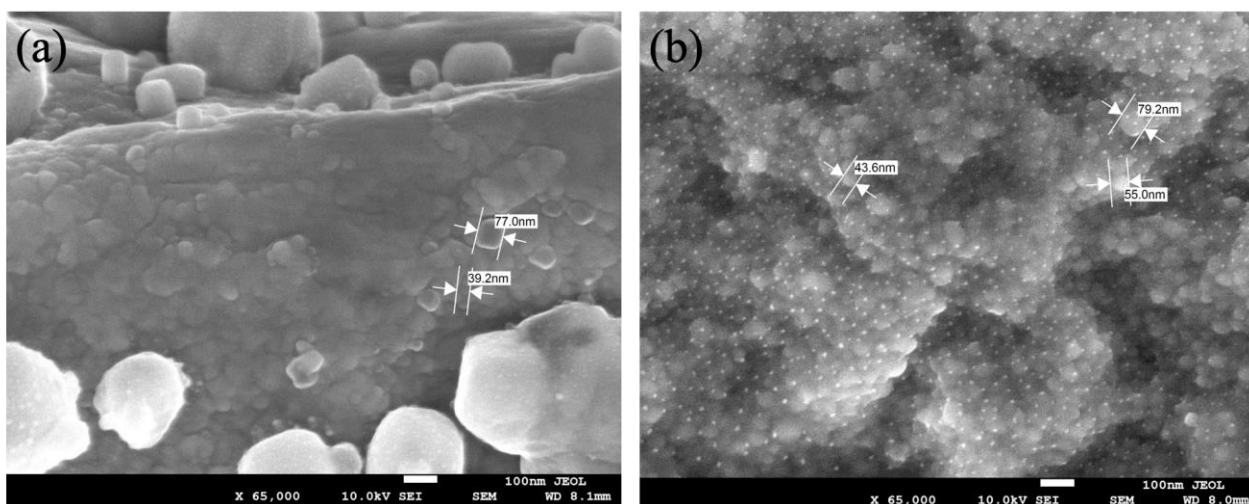


Figure 55 - Dense nanocrystalline films for growth conditions (a) 35°C for 20 min and (b) 100°C for 50 min.

Using a 55nm cube as an example Ag grain size, an electron would encounter a substantial change in resistance when moving across an entire Ag grain versus a grain boundary, as shown graphically in Figure 56 (a):

$$R_{Ag} = \frac{(\rho = 1.59 \times 10^{-8} \Omega)(55 \times 10^{-9} m)}{(55 \times 10^{-9} m)^2} = 0.289 \Omega$$

$$R_{gb} = \frac{(\rho = 5.2 \times 10^{-5} \Omega)(10 \times 10^{-9} m)}{(55 \times 10^{-9} m)^2} = 171.9 \Omega$$

The change in resistance suggests scattering at the grain boundaries. Whether Ag grain volume diffusion or diffusion along grain boundaries predominates depends on the diffusion lengths in the two materials as well as the physical path distances d and δ , shown graphically in Figure 56(b). The diffusion lengths in turn depend on the respective diffusion coefficients D and D_{gb} . However, the mean free path of an electron in Ag is 53nm which is comparable to the average grain size of 55nm. The films are densely packed and the space between Ag grains is small, $\delta \ll d$. From its much higher resistance, it is less likely that the criteria for diffusion along a grain boundary, $D_{gb} > D$, is obtained. We therefore conclude that the observed difference in conductivity may be due to grain boundary scattering but that conductivity is still likely to be dominated by volumetric Ag grain transport.

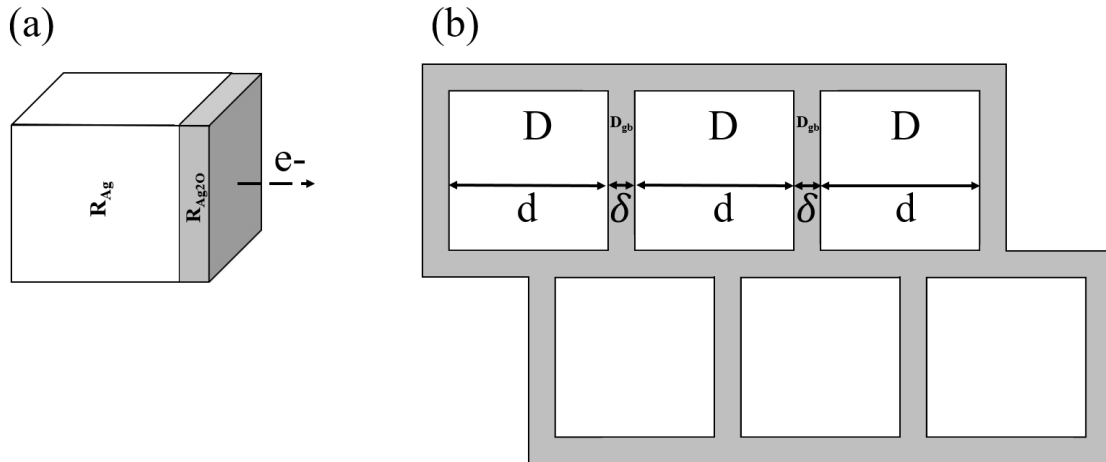


Figure 56 - (a) An electron traversing an Ag grain versus an Ag₂O grain boundary experiences an orders of magnitude difference in resistance. (b) Materials and geometric properties both influence whether transport is volumetric or along grain boundaries.

5.16 Conclusion

In summary, we have demonstrated that light-flash curing AJP deposited silver ink is a strong alternative method to develop a low temperature process that results in useful conductors for electronic applications. The uniformity of the material is consistent across the measurements from thickness variation and conductivity vs. number of printed layers and SEM cross-sectional analysis confirms that trend. Table 15 shows a comparison between the major technologies that are used for curing purposes. It is clear that the H3S has advantages over the other systems in terms of control and process parameters. The H3S also has low cost in terms of safety setup and ownership [125].

	Heat			Performance		Cost	
	Heat/Cool Speed	Uniformity	Energy Focus	Control *	Process Parameters **	Safety	Ownership
Humm3®	High	High	High	High	3	Low	Medium
Laser	High	High	High	Medium	1	High	High
Infrared	Low	Medium	Medium	Low	1	Low	Low
Hot Gas	Medium	Low	Low	Low	1	Medium	Low
* High level 3 parameter thermal control.							
** Humm3® controls the heat profile using 3 programmable pulse parameters: Energy, Duration and Frequency.							

Table 15 - Comparison of curing technologies

(Table reproduced with permission from [125].)

In conclusion, we consider this result an encouraging step toward process conditions suitable for obtaining silver ink conductive structures and contacts without long duration, high-temperature conditions. This approach should be a good candidate for printed OLED and TPV contacts or flexible electronics on soft substrates. We also conclude that utilizing SEM gives better

thickness measurement and also better characterization of the material uniformity after sintering. We also conducted an SEM study on the stored silver ink thin films and we concluded that the grain size stayed the same over a storage period of ~ 20 months. We also found through EDS analysis that the native surface oxide present on printed Ag is AgO that is consistent with common Silver(I,III) Oxide that forms on bulk Ag when exposed to air.

CHAPTER 6: CONCLUSION AND FUTURE WORK

6.1 Conclusion

The printing of precision high-conductivity metals has been a foundational technological breakthrough for realizing additively manufactured electronics integration from individual device contacts to circuits and packaged microsystems. For many applications, the quality of the printed metal is a result of a competition between the energetics of sintering metal nanoparticle inks and the tolerances of the active device and substrate materials to these sintering conditions. In this work, we present a study of pulsed-light curing of silver conductors that results in final conductivity values that are competitive with more common processes requiring temperatures of 150°C or higher. We focus on Aerosol-Jet Printed silver nanoparticle inks which have been studied extensively by curing with heat in ovens and hot plates, precision laser sintering, and UV flash methods. For low thermal-budget applications involving organic materials as active device structures or substrates, it is typical that sintering must reach ~150°C within the silver ink to obtain useful conductivity values. This is often done by precision means like laser annealing to protect the surrounding materials from the process. The results presented show that a pulsed-light system that is able to control the temperature profile through the basic parameters of pulse width, intensity, and repetition rate can be used to develop curing conditions at 35°C in less than one hour without the potential damage from UV light or the need for laser systems. The low temperature curing process results are compared to results from the same system at 100°C.

The objective of this investigation was to develop a low temperature silver ink curing process using a programmable controlled-dose pulsed-light source originally developed for automated fiber placement, the H3S system. The system uses flash lamp sources which are comparable to lasers in terms of power but allows better control of programmed energy delivery

profiles. Precise control can be achieved using energy, duration, and pulse repetition frequency. The apparatus is sufficiently agile for focusing heating on target areas which ensures proper material uniformity after annealing [36]. Compared with wave IR or laser illumination, the broadband (UV to IR) energy transfer results in better adhesion for the printed tracks as well as highly uniform films [37] and the H3S has performed favorably against both these methods for fiber placement as well. None of the previous studies have involved the curing of conductive layers, which has been developed here.

In this work, we demonstrate the light-pulse curing process on AJP deposited silver ink as a function of the thickness of the metal under curing conditions that achieve controlled temperatures of 35°C for time intervals from 20 to 30 minutes and 100°C for 50 minutes. The measured conductivity is compared to that of bulk silver and the material uniformity observed using cross-sectional SEM. This curing process demonstrates that the material can be cured at very low thermal budgets and result in conductive features practical for electronics. This method accurately demonstrates the potential of using H3S system as a new approach for fast, low temperature annealing for metal nanoparticle conductive inks.

This thesis demonstrated the progress of utilizing 3D printers in printing high frequency waveguides, contacts for OLED devices and meshes (grids) for TPVs using silver ink by printing the layers using Optomec Aerosol 5X inkjet printer. 3D printing method was deployed to print silver ink contacts that can be used with OLED and TPVs devices. We used a H3S precision optical heating system to cure the silver ink. As noted from the curing results, we can achieve 18% of bulk silver conductivity with 50 minutes of curing time at 100°C, this makes controlled optical pulse curing a good candidate for curing the contacts of OLED and TPV devices that can handle up to 150°C for shorter periods of time without degrading the organic material. To guarantee working

devices after optical pulse curing, the H3S or equivalent system has to be available locally as part of the device fabrication process flow in an uninterrupted fabrication cycle.

Our work involved an SEM study on the silver ink thin films after a storage period of 20 months, we concluded that the grain size did not change over time. We also conducted stoichiometry analysis using EDS methodology and found out that the native surface oxide present on printed silver ink is AgO which is consistent with common Silver(I,III) Oxide that forms on bulk Ag when exposed to air.

6.2 Future Work

Section 6.2.1 discusses the ability of manufacturing MRFs using fabrication processes by making different sizes that can be deployed into tornados. The small sizes of those fabricated MRFs are expected to endure the inner forces of the tornado and capable of providing sensory data for a better understanding of the tornado formation.

Section 6.2.2 presents an approach to 3D print the reflective mirror of an optical cavity using AJP which is expected to increase the efficiency of the optical cavity due to the uniformity of the deposited film after curing by the H3S system.

Section 6.2.3 shows a proposed method of printing the OLED device using AJP and curing the contacts using H3S. The proposed method is expected to cut cost as the whole process can be moved out of the cleanroom and carried out in a normal lab environment under ambient conditions.

Section 6.2.4 discusses different methods of curing silver ink; microwave radiation is one of those methods as it can be carried out under ambient conditions with temperatures below 110°C for shorter periods of time. Rapid thermal Process (RTP) is another approach as long as the system initial temperature is maintained below 150°C. As for the modified silver ink using poly vinyl acetate (PVAc) approach, it is noticed that adding PVAc as an additive to the Ag solution could

result in higher conductivity as the printed tracks can be cured using H3S at temperatures below 140°C which is compatible with most OLED devices.

6.2.1 MRF Microfabrication

The ability to mass produce MRFs is feasible utilizing microfabrication techniques so electronic circuit assembly time can be reduced and in turn the yield will be higher. Etching techniques to selectively remove silicon from substrates have been widely used in the fabrication of sensors and actuators [126], this approach can be used to build MRF with integrated microcontroller and sensors. Thickness and size of the MRF's rib and wing can be determined using chemical or electrochemical etch stop techniques [127] [128]. Surface micromachining on silicon-on-insulator (SOI) technique can be used to manufacture the MRF as well [129] [130].

6.2.2 Inkjet Printing of Optical Cavity Reflective Mirror

Recently, Yao *et al.* [131] presented printing technology of polymer suspended-mirror devices on a ferrule of optical fiber connector. Other groups presented micro lenses fabricated using inkjet printer [132]. Our suggested approach will be to cut the cylindrical mirror holder in two halves, print the aluminum NPs ink on each half using AJP and cure the material using pulsed optical curing. The two parts will be glued together to test the optical cavity performance.

6.2.3 Future Inkjet Printed OLED Structure

Cellphone industry using OLED technology dominated the market revenue in 2020 with 78% market share. On the other hand, TVs with OLED technology came second with 17% of the total market in the same year. Despite being 17% of the market revenue, OLED TVs are still having a big portion of the display area with 43% share. Wearable devices became third with 2% of the total OLED display market value and 0.3% by area in the year 2020. Other factors to be considered

when choosing a wearable device are: how thin, how flexible and its appearance comparing to liquid crystal display (LCD) technology [133].

In this section we highlight the process to fabricate OLED devices utilizing the inkjet printing process. The proposed process below shows the steps of fabricating OLED devices using the AJP. We suggest a flow for 3D printing of the structure as shown below (a-k):

- (a) The electron transport layer (ETL): Tris (8-hydroxyquinoline) aluminum (III) (Alq_3).
- (b) Solvent for ETL: Dimethylformamide (DMF).
- (c) Mixing process: 20mg of ETL in 1mL of DMF, mixed in a beaker using ultrasonic for 40 minutes at room temperature.
- (d) The hole transport layer (HTL): N,N'-Di(1-naphthyl)-N,N'-diphenyl-(1,1'-biphenyl)-4,4'-diamine (NPD).
- (e) Solvent for HTL: Chloroform (CHCl_3).
- (f) Mixing process: 20mg of HTL in 1mL of Chloroform, mixed in a beaker using ultrasonic for 1.5 - 2 hours at 30°C .
- (g) The ETL and HTL can be printed as one pass (layer $\sim 1\text{-}2\mu\text{m}$ thickness) using the UA of the AJP with the following print parameters:
- (h) Trace Width: $72\mu\text{m}$ (0.07 Units).
- (i) Min Overlap: 40, Max Overlap: 60 (Join All Segments, Offset Outline, Auto Radius Fill (Radius: 0.005)).
- (j) The nozzle size is $100\mu\text{m}$.
- (k) Sintering: After printing each layer, the substrate will be sintered on a hot plate, we anticipate that the HTL solvent will be evaporating at 60°C if sintered for 30 minutes and the ETL solvent will be evaporating at 80°C if sintered for 30 minutes.

Material Thicknesses Targets for Proposed Design:

- HTL = 60nm
- ETL = 60nm
- Al or Ag = 100nm

We expect the device efficiency for the 3D printed OLED to be lower than the regular OLEDs that are fabricated with vacuum thermal evaporation (VTE) process. One factor that could be responsible for this effect is that the devices are fabricated in air, thereby causing some degradation of the device performance. We anticipate Alq₃ which is the ETL material to emit light at 530nm wavelength, which is the green light visible spectrum. Figure 57 shows the proposed 3D printed OLED device structure.

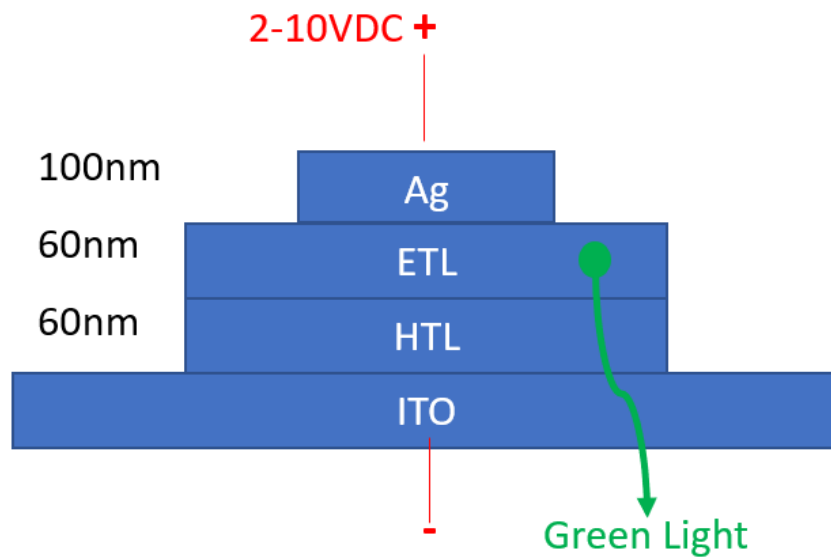


Figure 57 - Proposed 3D print OLED device structure

6.2.4 Other Methods of Curing Silver Ink

6.2.4.1 Flash Sintering using Microwave Radiation

OLED organic material cannot be sintered beyond 150°C; doing so will degrade the heterojunction material which could lead to a nonfunctional device. Therefore, other techniques

have to be used in order to facilitate fast and selective heating of materials. It has been shown that it is possible to create conductive printed features with microwave radiation within 3-4 minutes, with conductivity of 5% of the bulk silver value [134].

For the inkjet-printed silver ink to be conductive, a thermal process (sintering) is required to remove the organic binder that is present around the ink NPs. In 2009, Perelaer *et al.* demonstrated that flash microwave sintering of inkjet-printed devices is doable. The process depends on antenna total area, pre-curing time and line geometry. Metallic probes were used to print silver ink lines on top of them and directly cured in an oven for 1-5 minutes at 110°C. This short thermal curing evaporated the ink solvents. 1 W microwave power was used to sinter metal antenna for 1 second, this time was sufficient to obtain silver ink conductivity. Initial resistance of the pre-cured ink lines plays a major role in the degree of sintering for short exposure periods. Moreover, if the line width is increased, this will enhance the initial conductivity due to the enhancement in energy absorption because of the surface area increase. Tracks showed conductivities of 10% to 34% of theoretical bulk silver value after microwave flash curing. These conductivities are higher than the ones achieved using conventional methods [135].

Based on the work of Perelaer *et al.*, one possibility is to print multiple silver ink squares (15mm x 15mm) with 1 layer (1-2µm thickness) and sinter them using flash microwave concept with different time intervals and measure conductivity after each set interval, as a result, the interval that gives the best conductivity will be used for sintering the contacts of the OLED devices bearing in mind temperature of the device doesn't exceed the organic material temperature threshold. This would require a new system that MSU does not presently possess and cannot be achieved through adapting a commercial kitchen appliance microwave oven which operates at

~1000X the power level and does not have precision timing control to the sub-second level for adjustment.

6.2.4.2 Rapid Thermal Process

Another method to cure silver ink at temperatures between 200°C to 975°C can be accomplished using RTP. Jetfirst 100 and 150 RTP which are available at University of Michigan - Lurie Nanofabrication Facility (LNF) and they are capable of carrying out the curing process. The Jetfirst RTP 100 and RTP 150 are equipped with table-top, lamp-heated RTP tools used for annealing, dopant and silicide drive-in and general thermal processing tools. The tools are planned with very low thermal mass in a cold chamber so rapid heating and cooling are possible through the chamber walls. The tools are built for heating up temperatures starting from 200°C up to 975°C with rise times up to 15°C/sec with short dwell times (<10-15mins) at maximum temperature. The chamber interior consists of a bank of halogen lamps that are fixated at a 100mm wafer. The wafer is thermally isolated as its pins are mounted on glass to thermally isolate it from the walls of the chamber. Gas is introduced to the chamber through multiple small holes. Temperature is monitored using thermocouple that is connected to the wafer [136].

The main issue with this method is the initial temperature of 200°C, which is higher than what the organic material can tolerate without being damaged. Working with other RTP vendors that have systems with initial temperature of 150°C or below could be a solution to the sintering problem.

6.2.4.3 Modified Silver Ink using Poly Vinyl Acetate

In 2020, a team from Huazhong University of Science and Technology led by Junjie Li, proposed PVAc modified Ag complex ink that enhanced the foldability and conductivity of the

Ag patterns after quick sintering at low temperatures. The Ag-P complex ink was prepared by using the following materials [137]:

- Silver oxalate as Ag precursor.
- 1,2-Diaminopropane as complexing reagent.
- Methanol as organic solvent.
- Iso-propanol as organic solvent.
- A small amount of PVAc as binding agent.

Ag patterns were formed at low sintering temperatures of 140°C to 200°C within 2 minutes. Improvement in conductivity noticed after adding PVAc to the Ag patterns which resulted in better microstructure morphology, great density, higher smoothness and better uniformity. $5.17\mu\Omega\text{cm}$ resistivity of the sintered pattern (Ag-P complex ink) was reached at 180°C. This value of resistivity is about 3 times higher than that of bulk Ag. Folding test didn't affect the material conductivity which makes PVAc a good material for wearable devices. The measured conductivity of sintered Ag complex ink and sintered Ag-P complex ink at 200°C were $3.34 \times 10^4 \text{ S/cm}$ and $10.9 \times 10^4 \text{ S/cm}$, respectively [137]. Following the ink recipes explained in [137] to prepare the ink solution, the ink can be loaded to the UA on the AJP and printed on glass substrate as 15mm x 15mm square then sintered in a tubular furnace for 2 min in an ambient atmosphere. The tubular furnace needs to be preheated and stabilized to 150°C before sintering. This method can be applied to curing the silver ink contacts of OLED as well as the TPV contacts by maintaining a sintering temperature below 150°C.

APPENDIX

GRAIN SIZE IMAGE ANALYSIS MEASUREMENTS - RAW DATA

Data shown below represents the grain size measurements using NIH ImageJ software, average, standard deviation and S.E.M calculations for the 10 samples of silver ink that were inkjet-printed on glass substrate and cured using H3S system.

1. Sample 1:

Grain 1						
	Area (nm ²)	Mean	Min	Max	Angle	Length (nm)
1	216.942	123.931	100.934	183.982	-64.058	93.514
2	232.438	125.635	103.351	186.421	36.607	99.092
3	227.273	122.106	97.627	174.766	117.759	97.595
4	222.107	126.605	93.81	188.082	73.301	94.912
5	222.107	126.605	93.81	188.082	73.301	94.912
Average	224.1734					96.01
Grain 2						
1	180.785	140.456	122.059	172	8.366	78.104
2	170.455	148.167	128.229	211.898	102.724	72.228
3	149.793	145.059	123.268	180	40.601	62.861
4	185.95	148.281	123.2	214.714	88.363	79.578
5	139.463	141.302	122.751	201	-37.304	60.002
Average	165.2892					70.55
Grain 3						
1	175.62	116.265	102.253	160	-37.569	74.551
2	129.132	111.766	101.028	123.156	-135	54.64
3	201.446	116.769	97	136	0	86.364
4	154.959	124.233	104.761	195.891	-72.181	66.843
5	134.298	115.865	100	135	53.13	56.818
Average	159.091					67.84
Grain 4						
1	139.463	109.624	94	125.154	4.399	59.265
2	98.14	113.632	97	154.444	102.529	41.907
3	144.628	107.421	96.143	130	15.068	61.195
4	113.636	112.541	97.98	139	135	48.212
5	134.298	109.932	96.229	128.363	25.56	57.943
Average	126.033					53.70
Grain 5						
1	170.455	130.883	109.438	151.25	5.356	73.046
2	160.124	129.695	102	185.4	101.689	67.305
3	134.298	128.104	108.648	164.046	48.18	57.943
4	139.463	129.861	111.923	173.917	147.529	59.265
5	149.793	132.254	115.587	156.429	-154.36	63.025
Average	150.8266					64.12

Table 16 - Grain size measurement for 1-layer sintered at 35°C for 20 minutes - September 2019

2. Sample 2:

Grain 1						
	Area (nm ²)	Mean	Min	Max	Angle	Length (nm)
1	225.694	171.687	143.25	183.25	-140.19	48.814
2	190.972	175.042	166.5	182.953	45	41.248
3	208.333	173.393	162.667	183.506	39.472	45.881
4	208.333	176.73	159.667	197.584	-21.801	44.876
5	208.333	174.492	146.5	190.303	-45	44.194
Average	208.333					45.00
Grain 2						
1	364.583	119.055	94.333	143.639	-10.176	82.548
2	347.222	116.026	87.333	130.914	163.443	80.418
3	329.861	117.604	96	132.284	162.553	76.433
4	347.222	117.131	98	132.303	149.3	77.532
5	364.583	114.635	90.333	133.325	157.38	81.25
Average	350.6942					79.64
Grain 3						
1	190.972	110.942	95.333	124.038	-63.435	41.926
2	190.972	105.548	87.5	116.847	-20.225	42.184
3	208.333	106.99	88.5	115.405	39.472	45.881
4	208.333	108.895	88.5	114.091	62.241	44.731
5	190.972	108.052	88.5	115.4	43.025	42.746
Average	197.9164					43.49
Grain 4						
1	399.306	115.184	86.167	139.747	164.407	93.006
2	399.306	112.647	83.5	131.197	152.85	91.311
3	416.667	118.788	81.333	156.667	175.03	96.195
4	381.944	114.038	84.667	131	173.211	88.118
5	364.583	120.518	94.25	156.45	143.13	83.333
Average	392.3612					90.39
Grain 5						
1	277.778	98.021	86	106.253	164.055	60.668
2	277.778	108.992	80	156.453	-164.06	60.668
3	277.778	97.622	74.956	106.42	168.311	61.696
4	277.778	114.198	88.333	160.722	-149.04	60.739
5	277.778	112.1	82.333	169.406	-158.55	62.673
Average	277.778					61.29

Table 17 - Grain size measurement for 1-layer sintered at 35°C for 20 minutes - after storage

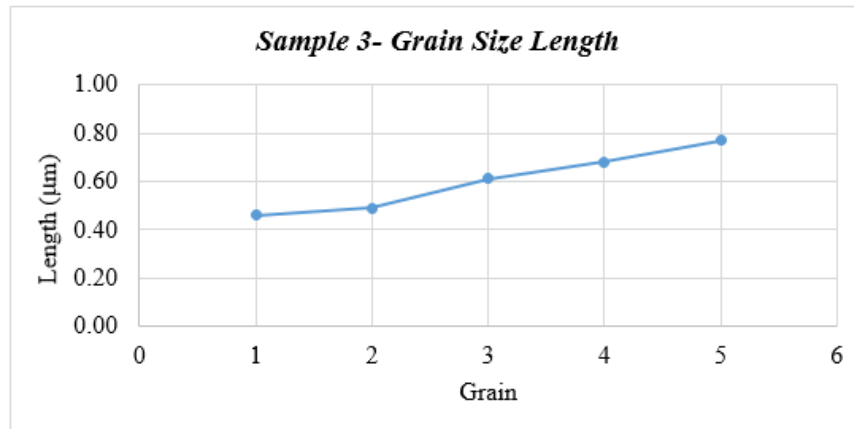
3. Sample 3:

Grain 1						
	Area (μm^2)	Mean	Min	Max	Angle	Length (μm)
1	0.019	188.872	175.086	236.183	48.013	0.492
2	0.019	193.582	174.899	232	136.548	0.479
3	0.019	191.73	178.444	231.87	-142.7	0.483
4	0.017	190.096	169.653	236.58	-85.03	0.422
5	0.017	194.946	180.278	221.927	177.51	0.421
Average	0.0182					0.46
Grain 2						
1	0.023	153.578	146.312	169.75	33.179	0.568
2	0.02	156.32	135	179	141.009	0.494
3	0.021	155.065	146.733	176	-144.25	0.564
4	0.016	159.877	151.568	177.727	-30.069	0.402
5	0.017	156.692	146	172.201	-65.556	0.442
Average	0.0194					0.49
Grain 3						
1	0.028	146.537	123.89	179	162.897	0.746
2	0.031	143.941	131.413	180	21.801	0.788
3	0.015	144.277	125.2	188	-87.138	0.366
4	0.028	136.735	123.841	161.2	-22.068	0.73
5	0.029	138.114	120.337	162	-163.69	0.781
Average	0.0262					0.68
Grain 4						
1	0.028	189.518	125	254.875	-97.125	0.737
2	0.024	186.025	108	254	-65.695	0.622
3	0.025	194.497	145	251.972	64.134	0.671
4	0.017	196.128	169.5	237.833	-4.764	0.441
5	0.023	204.242	177.812	246.259	49.97	0.597
Average	0.0234					0.61
Grain 5						
1	0.035	157.838	136.5	213	-11.31	0.933
2	0.017	164.593	141.333	207	-92.386	0.439
3	0.031	154.53	135.695	210.25	-34.778	0.802
4	0.028	156.287	135.88	193.065	1.469	0.714
5	0.036	157.989	134.415	226	-17.021	0.937
Average	0.0294					0.77

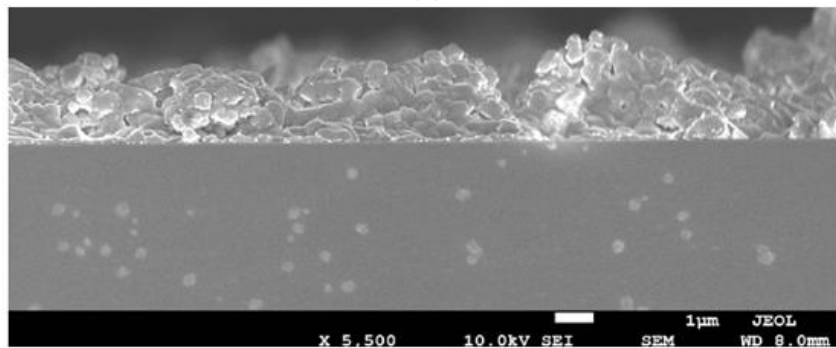
Table 18 - Grain size measurement for sample 3 - after storage

Grain	Length (μm)	Average	Standard Deviation	S.E.M
1	0.46			
2	0.49			
3	0.61			
4	0.68			
5	0.77			
	3.01	0.60	0.12	0.05

Table 19 - Average, standard deviation and S.E.M calculations for sample 3



(a)



(b)

Figure 58 - Sample 3 (a) Grain vs length (nm) (b) Processed image

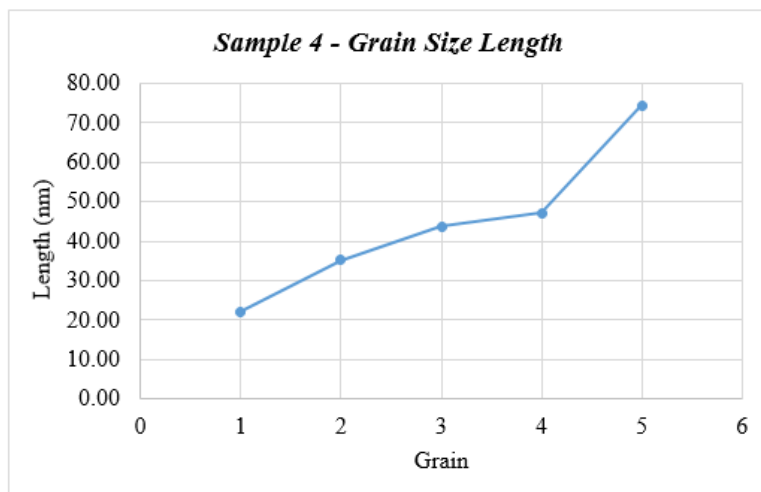
4. Sample 4:

Grain 1						
	Area (nm ²)	Mean	Min	Max	Angle	Length (nm)
1	170.367	173.355	133	206.062	5.356	73.027
2	180.692	178.44	148.638	243.263	106.858	78.348
3	185.854	173.277	149.608	202.087	50.826	79.134
4	165.204	175.806	143	189.777	150.945	70.179
5	165.204	176.103	141	204.392	-142.77	71.347
Average	173.4642					74.41
Grain 2						
1	113.578	215.379	167.333	245.603	95.44	47.931
2	118.74	214.919	183	239.97	21.801	48.943
3	113.578	207.961	147	242	84.56	47.931
4	108.415	213.484	152.667	246.626	-20.225	46.007
5	108.415	219.528	196.2	237.05	104.744	44.64
Average	112.5452					47.09
Grain 3						
1	103.252	163.862	140.548	187.967	16.557	43.853
2	113.578	158.217	128.102	189.626	35.218	47.28
3	113.578	154.291	100.333	183.81	75.964	46.841
4	98.09	169.807	119.667	188.111	141.843	40.454
5	98.09	157.873	129	192.469	-132.71	40.198
Average	105.3176					43.73
Grain 4						
1	92.927	166.755	128.333	194.513	57.265	37.816
2	72.277	177.274	122.333	219.998	-41.987	30.569
3	87.765	173.814	152.948	195.333	50.194	35.492
4	87.765	171.23	125.042	225.708	-10.62	36.988
5	87.765	176.061	136.167	223.318	-26.565	35.565
Average	85.6998					35.29
Grain 5						
1	61.951	68.838	53.636	80.455	-79.695	25.403
2	56.789	64.045	30.333	83.7	-163.3	23.722
3	51.626	62.379	39.671	75	122.005	21.435
4	51.626	71.233	63.103	81	-122.01	21.435
5	46.464	73.231	67	84	150.255	18.319
Average	53.6912					22.06

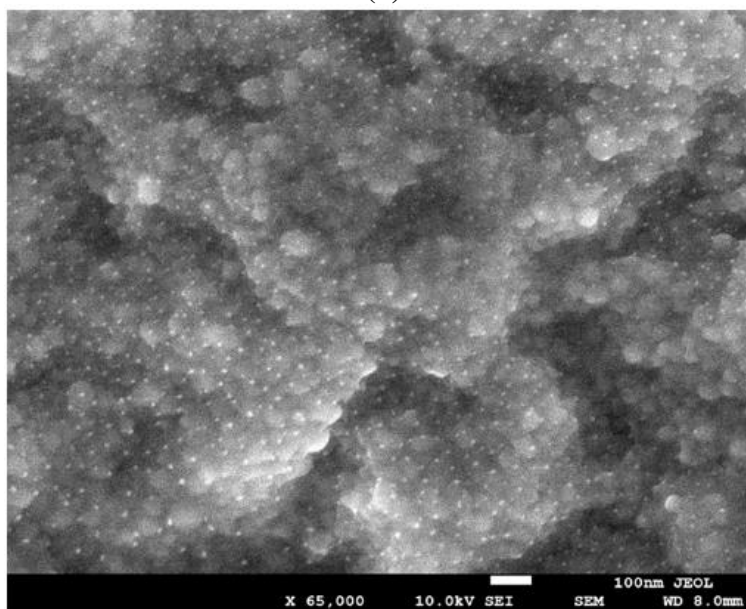
Table 20 - Grain size measurement for sample 4 - after storage

Grain	Length (nm)	Average	Standard Deviation	S.E.M
1	22.06			
2	35.29			
3	43.73			
4	47.09			
5	74.41			
	222.58	44.52	17.26	7.72

Table 21 - Average, standard deviation and S.E.M calculations for sample 4



(a)



(b)

Figure 59 - Sample 4 (a) Grain vs length (nm) (b) Processed image

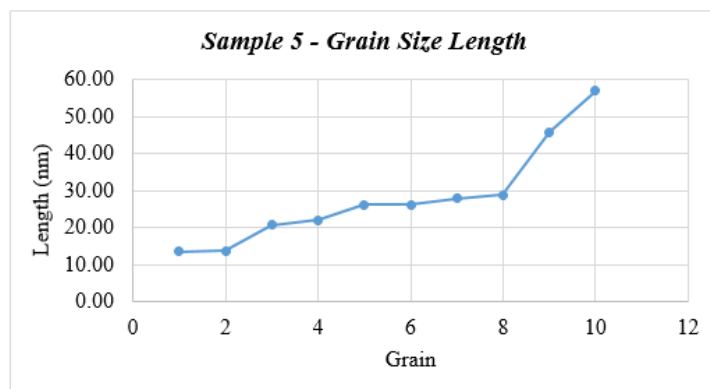
5. Sample 5:

Grain 1						
	Area (nm ²)	Mean	Min	Max	Angle	Length (nm)
1	111.769	123.167	115.562	136.125	-52.431	42.054
2	124.918	124.218	105	146.333	77.471	47.28
3	131.492	130.349	118.843	147.667	15.524	47.901
4	124.918	126.94	116.465	136.5	-106.39	45.436
5	124.918	127.541	111	140	-170.54	46.79
Average	123.603					45.89
Grain 2						
1	170.94	138.598	125	152.227	-36.87	64.103
2	105.194	138.461	123.333	147.573	-126.87	38.462
3	164.366	138.576	117	154	-34.992	62.598
4	170.94	139.638	122	161.8	-11.31	65.372
5	144.642	139.812	121	150.905	-58.57	54.09
Average	151.2164					56.93
Grain 3						
1	92.045	248.948	217.667	254.979	-151.39	32.128
2	78.895	250.299	241.667	254.926	-127.41	27.437
3	52.597	247.969	237	253	151.699	18.929
4	85.47	249.545	222.667	254.769	-145.01	31.299
5	85.47	246.269	218.333	255	-120.96	29.902
Average	78.8954					27.94
Grain 4						
1	78.895	245.975	228	253.718	-105.95	28
2	65.746	248.792	240.556	254.63	-26.565	22.934
3	72.321	249.339	232.75	254.79	39.094	26.43
4	78.895	246.358	218.75	254.694	98.13	27.196
5	72.321	244.117	206.333	254.05	8.531	25.928
Average	73.6356					26.10
Grain 5						
1	61.951	68.838	53.636	80.455	-79.695	25.403
2	56.789	64.045	30.333	83.7	-163.3	23.722
3	51.626	62.379	39.671	75	122.005	21.435
4	51.626	71.233	63.103	81	-122.01	21.435
5	46.464	73.231	67	84	150.255	18.319
Average	53.6912					22.06
Grain 6						
1	39.448	222.934	202	235.64	40.601	11.82
2	39.448	229.438	211	242.68	146.31	13.868
3	46.022	226.381	210.685	243.056	128.157	15.218
4	39.448	222.228	203.167	237.166	-137.49	13.914
5	39.448	227.459	201.648	240.579	-47.49	13.914
Average	40.7628					13.75
Grain 7						
1	78.895	131.095	122.75	137.977	5.194	28.321
2	78.895	134.895	109.5	164.748	98.13	27.196
3	78.895	132.396	122.517	148.376	20.854	28.811
4	78.895	133.462	112	166.545	-102.8	28.924
5	85.47	131.731	123	146.667	175.236	30.876
Average	80.21					28.83
Grain 8						
1	78.895	247.412	224.5	255	-123.69	27.735
2	65.746	252.407	241.667	255	140.389	24.13
3	72.321	251.191	242.667	255	70.145	24.535
4	78.895	247.623	214.625	255	-164.98	27.212
5	78.895	245.575	201.208	255	-94.086	26.992
Average	74.9504					26.12
Grain 9						
1	52.597	250.18	242.639	253.743	-120.07	18.765
2	59.172	248.684	240.5	254.618	-46.736	19.953
3	65.746	248.676	227.139	254.882	40.365	22.435
4	52.597	249.656	243.139	253.169	-78.69	17.433
5	72.321	244.034	197.722	254.056	180	24.786
Average	60.4866					20.67
Grain 10						
1	39.448	249.042	237.167	254.139	-140.19	13.351
2	39.448	242.006	207.5	254.603	-42.51	13.914
3	39.448	248.884	238.917	254.742	-140.71	12.148
4	39.448	244.639	231.167	253.3	-90	13.675
5	46.022	244.418	224.5	253.944	-166.76	14.927
Average	40.7628					13.60

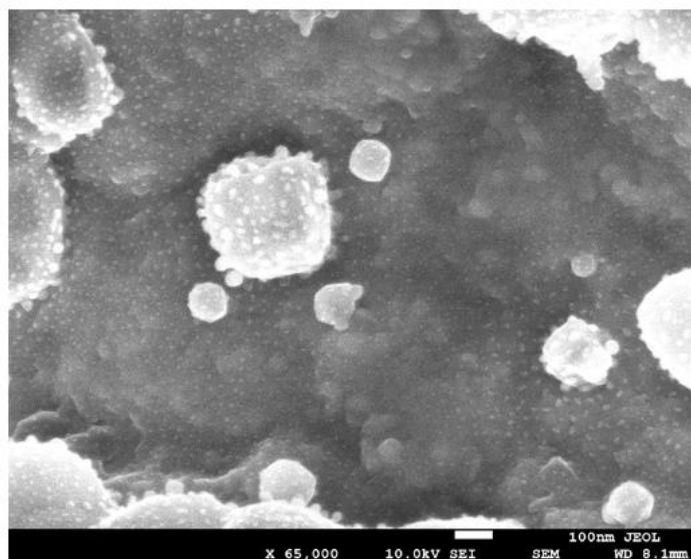
Table 22 - Grain size measurement for sample 5 - after storage

Grain	Length (nm)	Average	Standard Deviation	S.E.M
1	13.60			
2	13.75			
3	20.67			
4	22.06			
5	26.10			
6	26.12			
7	27.94			
8	28.83			
9	45.89			
10	56.93			
	281.89	28.19	12.90	4.08

Table 23 - Average, standard deviation and S.E.M calculations for sample 5



(a)



(b)

Figure 60 - Sample 5 (a) Grain vs length (nm) (b) Processed image

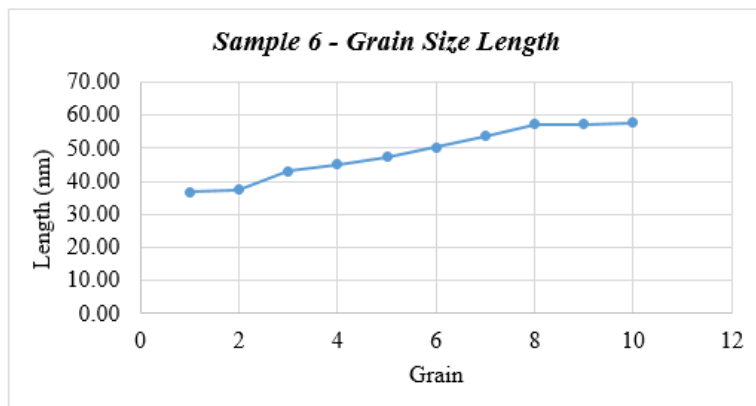
6. Sample 6:

Grain 1						
	Area (nm ²)	Mean	Min	Max	Angle	Length (nm)
1	140.617	133.495	118.898	149.507	48.18	59.291
2	129.8	135.641	111.333	152.919	129.806	54.49
3	140.617	127.704	111.738	144.832	40.101	57.766
4	146.025	131.859	111.308	158	171.254	61.176
5	135.208	132.655	115	149.042	-87.614	55.862
Average	138.4534					57.72
Grain 2						
1	113.575	98.319	75	116.333	-135	46.044
2	108.167	97.383	86.679	115.956	147.995	43.879
3	108.167	98.322	75	112	-126.25	43.258
4	108.167	97.098	77	109.723	145.491	45.155
5	113.575	97.33	82.5	110.16	57.095	47.089
Average	110.3302					45.09
Grain 3						
1	113.575	140.855	100.217	160.417	149.534	45.868
2	113.575	138.712	122.4	160.747	-36.87	46.512
3	108.167	139.354	103.861	160.172	147.995	43.879
4	118.983	145.663	127.732	165.333	27.759	49.932
5	124.392	134.819	111	155.479	-164.06	50.791
Average	115.7384					47.40
Grain 4						
1	129.8	121.908	100.417	134.735	-135	52.622
2	124.392	116.658	86.975	141.079	-54.162	51.636
3	124.392	126.139	101.609	141.129	-161.57	51.479
4	113.575	124.466	106.338	142.913	-49.086	46.161
5	124.392	119.447	93.86	135.626	166.608	50.202
Average	123.3102					50.42
Grain 5						
1	91.942	138.261	123	151	-119.75	37.499
2	91.942	139.145	121	152.875	-50.194	36.327
3	97.35	133.964	120.678	142.443	-139.76	39.603
4	91.942	135.733	120	146.348	-124.7	36.771
5	86.533	140.379	116	155.2	-61.699	34.337
Average	91.9418					36.91
Grain 6						
1	108.167	114.827	103.667	123.477	-117.9	44.733
2	102.758	115.545	97	126.745	-45	41.111
3	102.758	115.005	100	135.889	-42.709	41.144
4	108.167	112.668	90.25	124.791	126.573	44.884
5	108.167	112.528	99	123.914	-148	43.879
Average	106.0034					43.15
Grain 7						
1	129.8	119.276	100.832	140.259	-72.35	53.69
2	124.392	115.991	88.069	137.08	35.838	51.636
3	135.208	118.825	91	141.583	-75.379	55.278
4	129.8	119.045	101.667	139.043	-170.13	54.291
5	129.8	117.278	88	141	90	53.488
Average	129.8					53.68
Grain 8						
1	91.942	137.84	112	160	-140.19	36.327
2	86.533	140.23	110	152.36	-53.13	34.884
3	97.35	138.608	123.27	151.318	-25.017	38.495
4	97.35	136.712	118.737	146.249	-147.27	38.705
5	97.35	139.389	120	163	-90	39.535
Average	94.105					37.59
Grain 9						
1	140.617	141.29	127	159.027	-138.18	59.291
2	135.208	138.435	103.406	159.891	-47.49	56.787
3	140.617	136.914	119.588	161.967	-154.98	57.743
4	140.617	136.788	111	149.853	-113.96	57.261
5	135.208	139.319	108	166.852	-55.305	55.156
Average	138.4534					57.25
Grain 10						
1	140.617	123.278	102.5	138.13	-173.16	58.557
2	135.208	124.331	99.628	144.385	-3.918	56.722
3	135.208	117.416	89.481	139.194	-53.616	54.886
4	135.208	117.003	92.5	136.5	-20.925	56.435
5	146.025	118.356	92.222	137.206	177.026	59.77
Average	138.4532					57.27

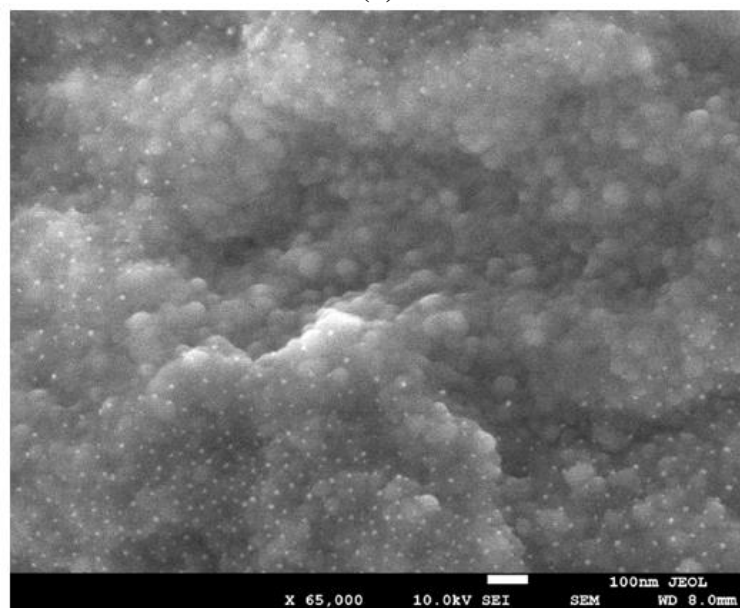
Table 24 - Grain size measurement for sample 6 - after storage

Grain	Length (nm)	Average	Standard Deviation	S.E.M
1	36.91	48.65	7.51	2.37
2	37.59			
3	43.15			
4	45.09			
5	47.40			
6	50.42			
7	53.68			
8	57.25			
9	57.27			
10	57.72			
	486.48			

Table 25 - Average, standard deviation and S.E.M calculations for sample 6



(a)



(b)

Figure 61 - Sample 6 (a) Grain vs length (nm) (b) Processed image

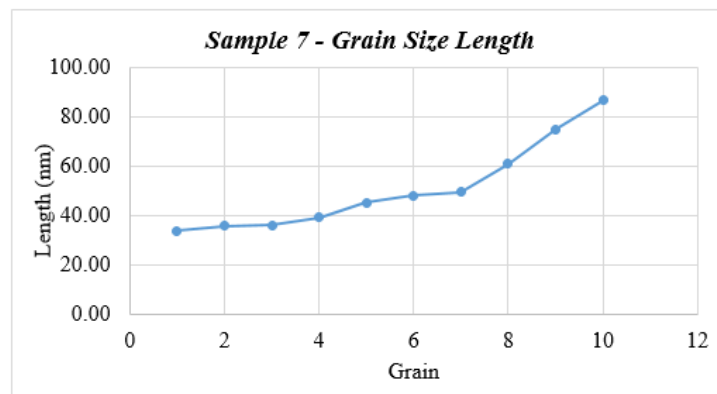
7. Sample 7:

Grain 1						
	Area (nm ²)	Mean	Min	Max	Angle	Length (nm)
1	199.917	188.746	156.25	202.045	-151.19	46.582
2	266.556	181.136	131	194.72	-174.09	59.5
3	249.896	184.362	147	200.357	-167.91	58.44
4	233.236	188.003	171	195.317	-173.16	51.386
5	216.576	189.536	163.5	206.979	-163.07	49.065
Average	233.2362					52.99
Grain 2						
1	166.597	162.257	133	192.827	-166.76	35.641
2	149.938	150.708	123.5	161.75	-124.7	32.268
3	149.938	166.671	145	194.617	158.199	32.97
4	149.938	168.141	145	195.438	172.405	30.883
5	149.938	168.014	126.5	204	-165.96	33.658
Average	153.2698					33.08
Grain 3						
1	99.958	174	134.972	191.144	-90	19.048
2	99.958	157.591	134.167	178.498	-93.576	21.811
3	116.618	134.74	121.028	144.111	-86.634	23.169
4	99.958	175.394	143.25	195.3	-82.405	20.589
5	99.958	155.384	130	180.717	-97.125	21.938
Average	103.29					21.31
Grain 4						
1	83.299	159.303	128.75	179.125	-85.601	17.739
2	99.958	158.94	128.75	175.446	-105.95	19.81
3	99.958	143.254	123.994	165.811	-78.69	20.812
4	99.958	152.087	130.833	169.433	-82.405	20.589
5	83.299	163.469	135.417	181.931	-109.98	15.925
Average	93.2944					18.98
Grain 5						
1	183.257	177.052	139.722	210.691	-128.05	39.736
2	149.938	152.41	137.056	163.306	-82.875	32.907
3	149.938	174.06	137.056	190.167	-36.87	34.014
4	166.597	170.597	141.083	191.016	-117.55	35.296
5	166.597	178.131	139.722	207.806	-132.14	38.53
Average	163.2654					36.10

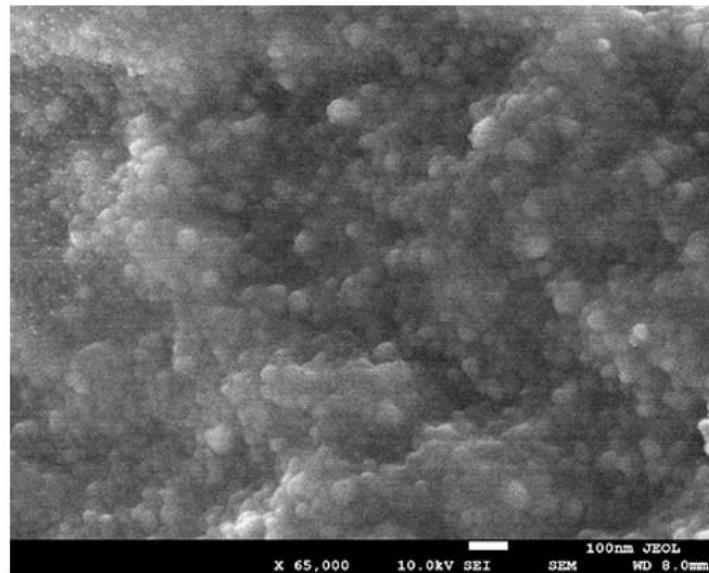
Table 26 - Grain size measurement for sample 7 - after storage

Grain	Length (nm)	Average	Standard Deviation	S.E.M
1	33.52	50.88	17.02	5.38
2	35.66			
3	35.86			
4	38.99			
5	45.21			
6	47.94			
7	49.28			
8	60.87			
9	74.93			
10	86.57			
	508.83			

Table 27 - Average, standard deviation and S.E.M calculations for sample 7



(a)



(b)

Figure 62 - Sample 7 (a) Grain vs length (nm) (b) Processed image

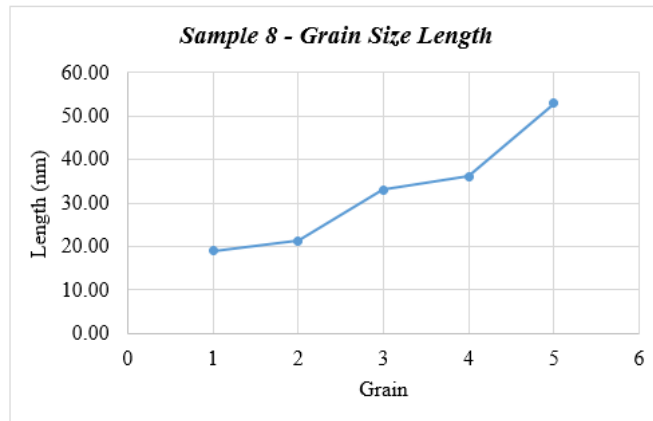
8. Sample 8:

Grain 1						
	Area (nm ²)	Mean	Min	Max	Angle	Length (nm)
1	199.917	188.746	156.25	202.045	-151.19	46.582
2	266.556	181.136	131	194.72	-174.09	59.5
3	249.896	184.362	147	200.357	-167.91	58.44
4	233.236	188.003	171	195.317	-173.16	51.386
5	216.576	189.536	163.5	206.979	-163.07	49.065
Average	233.2362					52.99
Grain 2						
1	166.597	162.257	133	192.827	-166.76	35.641
2	149.938	150.708	123.5	161.75	-124.7	32.268
3	149.938	166.671	145	194.617	158.199	32.97
4	149.938	168.141	145	195.438	172.405	30.883
5	149.938	168.014	126.5	204	-165.96	33.658
Average	153.2698					33.08
Grain 3						
1	99.958	174	134.972	191.144	-90	19.048
2	99.958	157.591	134.167	178.498	-93.576	21.811
3	116.618	134.74	121.028	144.111	-86.634	23.169
4	99.958	175.394	143.25	195.3	-82.405	20.589
5	99.958	155.384	130	180.717	-97.125	21.938
Average	103.29					21.31
Grain 4						
1	83.299	159.303	128.75	179.125	-85.601	17.739
2	99.958	158.94	128.75	175.446	-105.95	19.81
3	99.958	143.254	123.994	165.811	-78.69	20.812
4	99.958	152.087	130.833	169.433	-82.405	20.589
5	83.299	163.469	135.417	181.931	-109.98	15.925
Average	93.2944					18.98
Grain 5						
1	183.257	177.052	139.722	210.691	-128.05	39.736
2	149.938	152.41	137.056	163.306	-82.875	32.907
3	149.938	174.06	137.056	190.167	-36.87	34.014
4	166.597	170.597	141.083	191.016	-117.55	35.296
5	166.597	178.131	139.722	207.806	-132.14	38.53
Average	163.2654					36.10

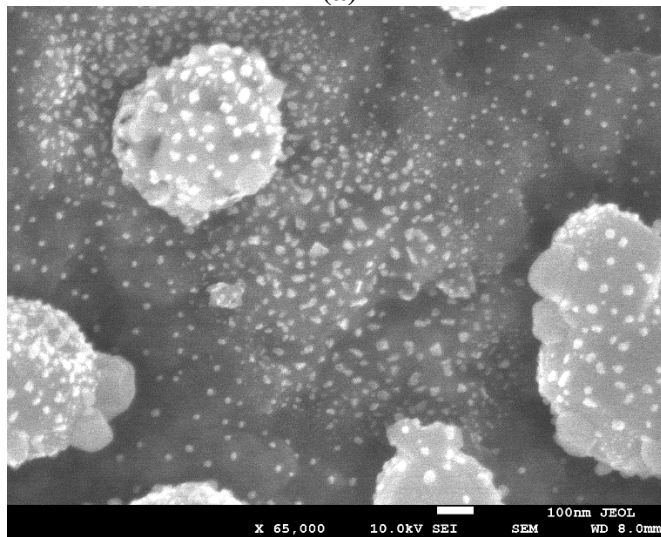
Table 28 - Grain size measurement for sample 8 - after storage

Grain	Length (nm)	Average	Standard Deviation	S.E.M
1	18.98			
2	21.31			
3	33.08			
4	36.10			
5	52.99			
	162.46	32.49	12.17	5.44

Table 29 - Average, standard deviation and S.E.M calculations for sample 8



(a)



(b)

Figure 63 - Sample 8 (a) Grain vs length (nm) (b) Processed image

9. Post Curing and Post Storage Samples Summary:

2021 Samples	μ	S.E.M	N
1	70.44	6.26	5
2	63.96	8.32	5
3	44.52	7.72	5
4	28.19	4.08	10
5	48.65	2.37	10
6	50.88	5.38	10
7	63.96	8.32	5
8	32.49	5.44	5
Average (nm)	50.39		
2019 Samples	μ	S.E.M	N
1	37.93	2.82	5
2	32.21	0.33	5
Average (nm)	35.07		

Table 30 - Samples post curing and post storage summary

BIBLIOGRAPHY

BIBLIOGRAPHY

- [1] S. K. Garlapati, M. Divya, B. Breitung, R. Kruk, H. Hahn and S. Dasgupta, "Printed Electronics Based on Inorganic Semiconductors: From Processes and Materials to Devices," *Advanced Materials*, vol. 30, no. 40, p. 1707600, 27 June 2018.
- [2] A. Efimov, P. Arsenov, D. Korniyushin, A. Lizunova, I. Volkov and V. Ivanov, "Aerosol Jet Printing of Silver Lines with A High Aspect Ratio on A Heated Silicon Substrate," *MDPI - Materials*, vol. 13, no. 3, p. 730, 5 February 2020.
- [3] M. Hengge, K. Livanov, N. Zamoshchik, F. Hermerschmidt and E. J. W. List-Kratochvil, "ITO-free OLEDs utilizing inkjet-printed and low temperature plasma-sintered Ag electrodes," *Flexible and Printed Electronics*, vol. 6, no. 1, p. 015009, 12 February 2021.
- [4] P. Calvert, "Inkjet Printing for Materials and Devices," *Chemistry of Materials*, vol. 13, no. 10, pp. 3299-3305, 12 September 2001.
- [5] T. H. J. v. Osch, J. Perelaer, A. W. M. d. Laat and U. S. Schubert, "Inkjet Printing of Narrow Conductive Tracks on Untreated Polymeric Substrates," *Advanced Materials*, vol. 20, no. 2, pp. 343-345, 20 December 2007.
- [6] H. Kodama, "Automatic method for fabricating a three-dimensional plastic model with photo-hardening polymer," *Review of Scientific Instruments*, vol. 52, no. 11, pp. 1770-1773, November 1981.
- [7] E. Sachs, M. Cima, P. Williams, D. Brancazio and J. Cornie, "Three Dimensional Printing: Rapid Tooling and Prototypes Directly from a CAD Model," *Journal of Manufacturing Science and Engineering*, vol. 114, no. 4, pp. 481-488, 1 November 1992.
- [8] T. Mikolajczyk, T. Malinowski, L. Moldovan, H. Fuwen, T. Paczkowski and I. Ciobanu, "CAD CAM System for Manufacturing Innovative Hybrid Design Using 3D Printing," *Procedia Manufacturing*, vol. 32, pp. 22-28, 2019.
- [9] D. Jang, D. Kim, B. Lee, S. Kim, M. Kang, D. Min and J. Moon, "Nanosized Glass Frit as an Adhesion Promoter for Ink-Jet Printed Conductive Patterns on Glass Substrates Annealed at High Temperatures," *Advanced Functional Materials*, vol. 18, no. 19, pp. 2862-2868, 2008.
- [10] B. K. Park, D. Kim, S. Jeong, J. Moon and J. S. Kim, "Direct writing of copper conductive patterns by ink-jet printing," *Thin Solid Films*, vol. 515, no. 19, pp. 7706-7711, 16 July 2007.

- [11] A. Khan, K. Rahman, D. S. Kim and K. H. Choi, "Direct printing of copper conductive micro-tracks by multi-nozzle electrohydrodynamic inkjet printing process," *Journal of Materials Processing Technology*, vol. 212, no. 3, pp. 700-706, March 2012.
- [12] N. J. Wilkinson, M. A. A. Smith, R. W. Kay and R. A. Harris, "A review of aerosol jet printing - a non-traditional hybrid process for micro-manufacturing," *The International Journal of Advanced Manufacturing Technology*, vol. 105, p. 4599–4619, 9 May 2019.
- [13] M. Abt, A. Roch, J. A. Qayyum, S. Pestotnik, L. Stepien, A. Abu-Ageel, B. Wright, A. Ulusoy, J. Albrecht, L. Harle, J. Papapolymerou and T. Schuelke, "Aerosol-Printed Highly Conductive Ag Transmission Lines for Flexible Electronic Devices," *IEEE Transactions on Components, Packaging and Manufacturing Technology*, vol. 8, no. 10, pp. 1838-1844, 24 September 2018.
- [14] C. Crump, V. Gjokaj, B. Wright, J. Papapolymerou, J. D. Albrecht and P. Chahal, "UV Flash Sintering of Aerosol Jet Printed Silver Conductors for Microwave Circuit Applications," *IEEE Transactions on Components, Packaging, and Manufacturing Technology*, vol. 11, no. 2, pp. 342-350, 24 December 2020.
- [15] S. H. Ko, H. Pan, C. P. Grigoropoulos, C. K. Luscombe, J. M. J. Fréchet and D. Poulikakos, "All-inkjet-printed flexible electronics fabrication on a polymer substrate by low-temperature high-resolution selective laser sintering of metal nanoparticles," *Nanotechnology*, vol. 18, no. 34, p. 345202, 1 August 2007.
- [16] W. Wan, C.-e. Huang, J. Yang, J. Zeng and T. Qiu, "Effect of Sintering Temperature on the Properties of Fused Silica Ceramics Prepared by Gelcasting," *Journal of Electronic Materials*, vol. 43, p. 2566–2572, 1 April 2014.
- [17] J. S. Kang, J. Ryu, H. S. Kim and H. T. Hahn, "Sintering of Inkjet-Printed Silver Nanoparticles at Room Temperature Using Intense Pulsed Light," *Journal of Electronic Materials*, vol. 40, pp. 2268-2277, 12 August 2011.
- [18] "Filament Properties Table," Simplify3D, 2021. [Online]. Available: <https://www.simplify3d.com/support/materials-guide/properties-table/>. [Accessed 23 April 2021].
- [19] Sandeep and D. Chhabra, "Comaprison and analysis of different 3D printing techniques," *International Journal of Latest Trends in Engineering and Technology*, vol. 8, no. 4-1, pp. 264-272.
- [20] R. E. Williams, S.N.Komaragiri, V. L. Melton and R. R. Bishu, "Investigation of the effect of various build methods on the performance of rapid prototyping (stereolithography)," *Journal of Materials Processing Technology*, vol. 61, pp. 173-178, 1996.

- [21] X. Wang, M. Jiang, Z. Zhou, J. Gou and D. Hui, "3D printing of polymer matrix composites: A review and prospective," *Composites Part B*, vol. 110, pp. 442-458, February 2017.
- [22] X. Yan and P. Gu, "A review of rapid prototyping technologies and systems," *Computer-Aided Design*, vol. 26, no. 4, pp. 307-316, 1996.
- [23] N. Alharbi, R. Osman and D. Wismeijer, "Effects of build direction on the mechanical properties of 3D-printed complete coverage interim dental restorations," *The Journal of Prosthetic Dentistry*, 21 January 2016.
- [24] "The Resolution, Printing Size and Accuracy in Resin 3D Printer," Chitubox, 2021. [Online]. Available: <https://www.chitubox.com/en/article/support/indepth/technology/26>. [Accessed 3 May 2021].
- [25] "What Are the Advantages and Disadvantages of SLA and DLP Printers?," Home3DPrints, 2021. [Online]. Available: <https://home3dprints.com/what-are-the-ads-and-disads-of-sla-and-dlp-printers/>. [Accessed 3 May 2021].
- [26] "The Complete Digital Light Processing (DLP) 3D Printing Guide," 3DSourced, 2021. [Online]. Available: https://www.3dsourced.com/3d-printing-technologies/digital-light-processing-dlp/#Advantages_of_DLP. [Accessed 3 May 2021].
- [27] Alkaios Bournias Varotsis, "Introduction to SLS 3D printing," 3D Hubs, [Online]. Available: <https://www.3dhubs.com/knowledge-base/introduction-sls-3d-printing/#:~:text=SLS%20can%20produce%20functional%20parts,x%20300%20x%20300%20mm..> [Accessed 3 May 2021].
- [28] P. Hanzl, M. Zetek, T. Baksa and T. Kroupa, "The Influence of Processing Parameters on the Mechanical Properties of SLM Parts," *Procedia Engineering*, vol. 100, pp. 1405-1413, 2015.
- [29] J. Mueller, K. Shea and C. Daraio, "Mechanical properties of parts fabricated with inkjet 3D printing through efficient experimental design," *ScienceDirect - Materials & Design*, vol. 86, no. 5, pp. 902-912, December 2015.
- [30] H. Miyajima, S. Zhang, A. Lassell, A. A. Zandinejad and L. Yang, "Optimal Process Parameters for 3D Printing of Porcelain Structures," *Procedia Manufacturing*, vol. 5, pp. 870-887, 2016.
- [31] "What is Selective Deposition Lamination (SDL)?," 13 April 2016. [Online]. Available: <https://www.additive-x.com/blog/selective-deposition-lamination-sdl/>. [Accessed 3 May 2021].

- [32] Joseph Flynt, "What is Electron Beam Melting? Properties, Pros and Cons, and Applications," 3D Insider, 22 April 2020. [Online]. Available: <https://3dinsider.com/electron-beam-melting/>. [Accessed 3 May 2021].
- [33] "Electron Beam Melting (EBM)," Engineering Product Design, [Online]. Available: <https://engineeringproductdesign.com/knowledge-base/electron-beam-melting/>. [Accessed 3 May 2021].
- [34] Carlota V., "The Complete Guide to Electron Beam Melting (EBM) in 3D Printing," 3D Natives, 7 October 2019. [Online]. Available: <https://www.3dnatives.com/en/electron-beam-melting100420174/#!>. [Accessed 3 May 2021].
- [35] J. T. Huh, J. J. Yoo, A. Atala and S. J. Lee, "Digital light processing," in *Three-dimensional bioprinting for tissue engineering*, Elsevier, 2020, p. 1395.
- [36] G. Rousseau, R. Wehbe, J. Halbritter and R. Harik, "Automated Fiber Placement Path Planning: A state-of-the-art review," *Computer-Aided Design & Applications*, vol. 16, no. 2, pp. 172-203, 2019.
- [37] D. Deden, F. Bruckner, L. Brandt and F. Fischer, "Comparison of heat sources for automated dry fibre placement: Xenon flashlamp vs. infrared heating," in *Twenty-Second International Conference on Composite Materials (ICCM22)*, Melbourne, Australia, 2019.
- [38] E. Balliu, H. Andersson, M. Engholm, T. Öhlund, H.-E. Nilsson and H. Olin, "Selective laser sintering of inkjet-printed silver nanoparticle inks on paper substrates to achieve highly conductive patterns," *Nature - Scientific Reports*, vol. 8, p. 10408, 10 July 2018.
- [39] S. H. Ko, H. Pan, C. P. Grigoropoulos, C. K. Luscombe, J. M. J. Fréchet and D. Poulikakos, "All-inkjet-printed flexible electronics fabrication on a polymer substrate by low-temperature high resolution selective laser sintering of metal nanoparticles," *Nanotechnology*, vol. 18, no. 34, p. 345202, 1 August 2007.
- [40] F. Cai, S. Pavlidis, J. Papapolymerou, Y. Chang, K. Wang, C. Zhang and B. Wang, "Aerosol jet printing for 3-D multilayer passive microwave circuitry," *44th European Microwave Conference*, pp. 512-515, 2014.
- [41] "Durometer Shore Hardness Scale," Smooth-On, 2021. [Online]. Available: <https://www.smooth-on.com/page/durometer-shore-hardness-scale/>. [Accessed 18 June 2021].
- [42] "Connex350™- Multi-Material 3D Printers," 3D Printers Canada, 2021. [Online]. Available: <http://www.3dprinterscanada.com/connex-3d-printer-family-connex350.php>. [Accessed 18 June 2021].
- [43] "Objet350 Connex," SMG3D, 2021. [Online]. Available: https://www.smg3d.co.uk/commercial/objet350_connex_3d_printer_from_stratasys. [Accessed 18 June 2021].

- [44] "VeroWhite Material Guide," Sculpteo - A brand of BASF, 2021. [Online]. Available: <https://www.sculpteo.com/en/materials/polyjet-resin-material/verowhite-polyjet-resin-material/>. [Accessed 18 June 2021].
- [45] "VeroWhitePlus - Polyjet Technology Material Specifications," Stratasys Direct, Inc., 2021.
- [46] "OBJDF Files: Overview," Stratasys, 2021. [Online]. Available: https://my.stratasys.com/SupportCenter/HTML5UserGuides/Objet1000_UG_Feb_2019/Content/5_Topics_Using%20OS/objet-studio_OBJDF.htm. [Accessed 18 June 2021].
- [47] "What is an STL file?," Sculpteo - A brand of BASF, 2021. [Online]. Available: <https://www.sculpteo.com/en/3d-learning-hub/create-3d-file/what-is-an-stl-file/>. [Accessed 18 June 2021].
- [48] M. Burns, Automated Fabrication, 1st ed., Prentice Hall, 1993 , p. 369.
- [49] "Aerosol Jet Technology," Optomec, 2020. [Online]. Available: <https://optomec.com/printed-electronics/aerosol-jet-technology/>. [Accessed 08 October 2020].
- [50] M. Molitch-Hou, "Aerosol Jet 5X 3D Printer," Optomec, 28 April 2016. [Online]. Available: <https://optomec.com/aerosol-jet-5x-3d-printer/>. [Accessed 18 June 2021].
- [51] "ECE Testing Facility - Optomec 5X Aerosol Jet 3D Printing System," Michigan State University, 2021. [Online]. Available: <https://www.egr.msu.edu/eceshop/testingfacility/optomec/>. [Accessed 18 June 2021].
- [52] "Prelect TPS 50 G2 CI0005 Safety Data Sheet," Clariant, 2021.
- [53] "Ink Starter Recipe Sheet," Optomec, 7 April 2016. [Online]. Available: <https://www.optomec.com/wp-content/uploads/2014/02/Silver-Clariant-EXPT-Prelect-TPS-50G2-040716.pdf>. [Accessed 09 October 2020].
- [54] Optomec, *Aerosol Jet KEWA™ User Guide (for version 2.0 or newer), OPTOMECC Production Grade 3D Printers...with a Material Difference*, OPTOMECC.
- [55] "Humm3 - Intelligent heat for Automated Fibre Placement (AFP)," Heraeus, 19 October 2020. [Online]. Available: https://www.heraeus.com/en/hng/products_and_solutions/arc_and_flash_lamps/humm3/humm3.html#tabs-115105-1.
- [56] Ginger Gardiner, "Innovating energy delivery for more efficient composites manufacturing," CW Composites World, 11 9 2019. [Online]. Available: <https://www.compositesworld.com/articles/innovating-energy-delivery-for-more-efficient-composites-manufacturing>. [Accessed 19 JUNE 2021].

- [57] "Pro-4 Four Point Resistivity Systems," Lucas Labs - Division of Lucas/Signatone, 2021. [Online]. Available: <https://www.signatone.com/lucaslabs.com/pro4.html>. [Accessed 19 June 2021].
- [58] "Lucas/Signatone Four Point Probe - Standard Head (Derlin)," Lucas / Signatone Corporation, 2021. [Online]. Available: <https://www.signatone.com/pdf/SP4-2018.pdf>. [Accessed 19 June 2021].
- [59] "Keysight 2-Port and 4-Port PNA Network Analyzer," Keysight Technologies, 11 April 2019. [Online]. Available: <https://www.keysight.com/us/en/assets/9018-04206/technical-specifications/9018-04206.pdf>. [Accessed 19 June 2021].
- [60] "NA Extender - VDI Model: WR10-VNAX," Virginia Diodes, [Online]. Available: <https://vadiodes.com/en/wr10-vnax>. [Accessed 19 June 2021].
- [61] "NanoMap 500LS: Scanning 3D Surface Profilometer," AEP Technology, 28 12 2010. [Online]. Available: <http://www.ihanmi.com/image1/image-aep/Catalogue-NanoMap%20500LS.pdf>. [Accessed 19 June 2021].
- [62] "TA Instruments TGA 500," Michigan State University - Composite Materials and Structures Center, 2021. [Online]. Available: <https://www.egr.msu.edu/cmsc/equipments/ta-instruments-tga-500>. [Accessed 19 June 2021].
- [63] "TGA Thermogravimetric Analyzer," TA Instruments, June 2006. [Online]. Available: <https://www.usf.edu/research-innovation/rf/usf-connect/documents/tga-q500.pdf>. [Accessed 19 June 2021].
- [64] "TA Instruments Thermal Analysis Brochure," TA Instruments, [Online]. Available: <http://www.tainstruments.com/pdf/TGA%20Brochure.pdf>. [Accessed 19 June 2021].
- [65] "JSM-7500F Field Emission Scanning Electron Microscope," JEOL, 2021. [Online]. Available: <https://www.jeol.co.jp/en/products/detail/JSM-7500F.html>. [Accessed 19 June 2021].
- [66] S. Swapp, "Scanning Electron Microscopy (SEM)," Geochemical Instrumentation and Analysis, [Online]. Available: https://serc.carleton.edu/research_education/geochemsheets/techniques/SEM.html. [Accessed 21 October 2020].
- [67] "Ultra High Resolution FE SEM JSM-7500F/JSM-7500FA Field Emission SEM/Analytical Field Emission SEM," JEOL Ltd., [Online]. Available: <https://documents.uow.edu.au/content/groups/public/@web/@aiim/documents/doc/uow154681.pdf>. [Accessed 27 June 2021].

- [68] Tiago Ferreira and Wayne Rasband, "ImageJ User Guide," NIH.gov, 02 10 2012. [Online]. Available: <https://imagej.nih.gov/ij/docs/guide/user-guide.pdf>. [Accessed 22 June 2021].
- [69] D. Aslam, A. Abu-Ageel, M. Alfatlawi, M. Varney, C. Thompson and S. Aslam, "Passive Maple-seed Robotic Fliers for Education, Research and Entrepreneurship," *Journal of Education and Training Studies*, vol. 2, no. 2, pp. 206-216, April 2014.
- [70] N. Abu-Ageel and A. Abu-Ageel, "A Miniature Laser-Driven Visible Light Source," *The Society for Information Display (SID)*, vol. 46, no. 1, pp. 365-367, 29 July 2015.
- [71] T. Nomura and N. Tejima, "Critical consideration of applications of affective robots to mental therapy from psychological and sociological perspectives," in *Proceedings. 11th IEEE International Workshop on Robot and Human Interactive Communication*, Berlin, Germany, 2002.
- [72] K. Kosuge, T. Daigaku, Sendai, Miyagi and JP, "Human-robot interaction - What we learned from robot helpers and dance partner robots," *RO-MAN 2008 - The 17th IEEE International Symposium on Robot and Human Interactive Communication*, 15 August 2008.
- [73] J. Yuh, "Design and Control of Autonomous Underwater Robots: A Survey," *Autonomous Robots*, vol. 8, pp. 7-24, January 2000.
- [74] G. T. Anderson, E. W. Tunstel and E. W. Wilson, "Robot System to Search for Signs of Life on Mars," *IEEE Aerospace and Electronic Systems Magazine*, vol. 22, no. 12, pp. 23-30, 26 December 2007.
- [75] F. Klassner, "A case study of LEGO Mindstorms™ suitability for artificial intelligence and robotics courses at the college level," in *SIGCSE '02: Proceedings of the 33rd SIGCSE technical symposium on Computer science education*, 2002.
- [76] S. K. H. Win, L. S. T. Win, D. Sufiyan, G. S. Soh and S. Foong, "Concurrent Optimization of Mechanical Design and Control for Flapless Samara-Inspired Autorotating Aerial Robot," in *2020 IEEE/ASME International Conference on Advanced Intelligent Mechatronics (AIM)*, Boston, MA, USA, 2020.
- [77] S. Thakoor, "Bio-Inspired Engineering of Exploration," in *Journal of Space Mission Architecture*, 2000.
- [78] E. Ulrich, I. Faruque, J. Grauer, D. Pines, J. Humbert and J. Hubbard, "Control Model for Robotic Samara: Dynamics About a Coordinated Helical Turn," *Journal of Guidance, Control and Dynamics*, vol. 33, no. 6, 23 May 2012.
- [79] W. Harned, "Maple-seed Simulating Auto-rotating Toy and Associated Game". Patent 5,505,650 , 9 April 1996.

- [80] D. Aslam, Z. Cao, M. Varney and S. Gur, "Outreach and Workforce Training using Maple-Seed Robotic," in *Proc. of IEEE SEM Fall Conf*, Dearborn, MI, 2010.
- [81] D. Aslam, A. Abu-Ageel, M. Alfatlawi, M. Varney, C. Thompson and S. Aslam, "Passive Maple-seed Robotic Fliers (MRF) with On-board Accelerometer & Microcontroller," in *2012 Proc. of IEEE SEM Fall Conf.*, Dearborn, MI, 2012.
- [82] F. Sullivan, "Robotics and Science Literacy: Thinking Skills, Science Process Skills and Systems Understanding," *Journal of Research in Science Teaching*, vol. 45, no. 3, pp. 373-394, 04 February 2005.
- [83] M. Jojoa Jimenez, C. Bravo and B. Bacca Cortes, "Tool for Experimenting With Concepts of Mobile Robotics as Applied to Children's Education," *IEEE Transactions on Education*, vol. 53, no. 1, pp. 88-95, 04 September 2009.
- [84] S. Singh, R. Fitch and S. Williams, "A research-driven approach to undergraduate robotics education," *Computers in Education Journal*, no. 4, pp. 21-27, 2010.
- [85] L. Feisel and A. Rosa, "The Role of the Laboratory in Undergraduate Engineering Education," *American Society for Engineering Education - JEE*, vol. 94, no. 1, pp. 121-130, 02 January 2013.
- [86] "VeroWhite Plus PolyJet," CIDEAS Inc., 2014. [Online]. Available: <https://www.buildparts.com/materials/verowhiteplus>. [Accessed 6 October 2020].
- [87] K. Li, "25.3: LED Array with Recycling for High-Power Projector Applications," *Society for Information Display (SID)*, vol. 42, no. 1, pp. 323-325, 16 August 2012.
- [88] U. Steegmülle, M. Kühnelt, H. Unold, T. Schwarz, R. Schulz, K. Auen, C. Walter and M. Schmitt, "Visible lasers for mobile projection," *Photonics in Multimedia II*, vol. 7001, 2008.
- [89] W. O. Davis, R. Sprague and J. Miller, "MEMS-based pico projector display," in *2008 IEEE/LEOS International Conference on Optical MEMs and Nanophotonics*, Freiburg, Germany, 2008.
- [90] S. An, A. Lapchuk, V. Yurlov, J. Song, H. Park, J. Jang, W. Shin, S. Kargapolstev and S. K. Yun, "Speckle suppression in laser display using several partially coherent beams," *Optics Express*, vol. 17, no. 1, pp. 92-103, 22 December 2008.
- [91] F. Romeo, "Casio Projectors with Hybrid LED/Laser/Phosphor Illumination," *Society for Information Display*, vol. 41, no. 1, pp. 979-981, 05 July 2012.
- [92] N. Abu-Ageel and D. Aslam, "Laser-Driven Visible Solid-State Light Source for Etendue-Limited Applications," *Journal of Display Technology*, vol. 10, no. 8, pp. 700-703, 10 April 2014.

- [93] K. Morimoto, H. Kasugai, T. Takizawa, S. Yoshida, K. Yamanaka, T. Katayama, K. Okuyama, S. Shiraishi and Y. Mizuyama, "A 30 W Pure Blue Emission with NUV Laser-Diode-Pumped Phosphor for High-Brightness Projectors," *SID Symposium Digest of Technical Papers*, vol. 44, no. 1, pp. 832-835, 01 July 2013.
- [94] J. I. Trisnadi, "Speckle contrast reduction in laser projection displays," in *Proc. SPIE 4657, Projection Displays VIII*, San Jose, California, USA, 2002.
- [95] F. Fournier and J. Rolland, "Design Methodology for High Brightness Projectors," *Journal of Display Technology*, vol. 4, no. 1, pp. 86-91, March 2008.
- [96] S. Das, D. L. Bourell and S. Babu, "Metallic materials for 3D printing," *MRS Bulletin*, vol. 41, no. 10, pp. 729-741, 10 October 2016.
- [97] F. Cai, Y.-H. Chang, K. Wang, C. Zhang and J. Papapolymerou, "Low-Loss 3-D Multilayer Transmission Lines and Interconnects Fabricated by Additive Manufacturing Technologies," *IEEE Transactions on Microwave Theory and Techniques*, vol. 64, no. 10, pp. 3208-3216, 05 September 2016.
- [98] J. Daintith, *A Dictionary of Physics*, OUP Oxford, 2009.
- [99] Y. He, M. Becker, T. Grotjohn, A. Hardy, M. Muehle, T. Schuelke and J. Papapolymerou, "RF characterization of coplanar waveguide (CPW) transmission lines on single-crystalline diamond platform for integrated high power RF electronic systems," *IEEE MTT-S International Microwave Symposium (IMS)*, pp. 517-520, June 2017.
- [100] X. Konstantinou, C. J. Herrera-Rodriguez, M. T. Craton, A. Hardy, C. Crump, J. D. Albrecht, Q. H. Fan, T. Grotjohn and J. Papapolymerou, "A Monolithic Wilkinson Power Divider on Diamond via a Combination of Additive Manufacturing and Thin-Film Process," *IEEE Radio and Wireless Symposium (RWS)*, January 2020.
- [101] J. Abdul Qayyum, M. Abt, A. Roch, A. Ulusoy and J. Papapolymerou, "Ultra wideband 3D interconnects using aerosol jet printing up to 110 GHz," in *12th European Microwave Integrated Circuits Conference (EuMIC)*, Nuremberg, Germany, 2017.
- [102] A. Dearden, P. Smith, D.-Y. Shin, N. Reis, B. Derby and P. O'Brien, "A Low Curing Temperature Silver Ink for Use in Ink-Jet Printing and Subsequent Production of Conductive Tracks," *Macromolecular Rapid Communications*, pp. 315-318, 17 November 2004.
- [103] P. Smith, D. Shin, J. Stringer, B. Derby and N. Reis, "Direct ink-jet printing and low temperature conversion of conductive silver patterns," *Journal of Materials Science*, pp. 4153-4158, 01 July 2006.

- [104] M. Smith, Y. Choi, C. Boughey and S. Kar-Narayan, "Controlling and assessing the quality of aerosol jet printed features for large area and flexible electronics," *Flexible and Printed Electronics*, vol. 2, no. 1, 28 February 2017.
- [105] J. Hoey, A. Lutfurakhmanov, D. Schulz and I. Akhatov, "A Review on Aerosol-Based Direct-Write and Its Applications for Microelectronics," *Journal of Nanotechnology*, vol. 2012, 5 September 2012.
- [106] T. Seifert, E. Sowade, F. Roscher, M. Wiemer, T. Gessner and R. Baumann, "Additive Manufacturing Technologies Compared: Morphology of Deposits of Silver Ink Using Inkjet and Aerosol Jet Printing," *American Chemical Society*, vol. 54, no. 2, pp. 769-779, 8 January 2015.
- [107] J. Paulsen, M. Renn, K. Christenson and R. Plourde, "Printing conformal electronics on 3D structures with Aerosol Jet technology," in *Future of Instrumentation International Workshop (FIIW) Proceedings*, Gatlinburg, TN, 2012.
- [108] H. Sirringhaus, T. Kawase, R. Friend, S. Inbasekaran and W. Wu, "High-Resolution Inkjet Printing of All-Polymer Transistor Circuits," *Science (American Association for the Advancement of Science)*, vol. 290, no. 5499, pp. 2123-2126, 15 December 2000.
- [109] M. Hilder, B. Winther-Jensen and N. Clark, "Paper-based, printed zinc-air battery," *Journal of Power Sources*, vol. 194, no. 2, pp. 1135-1141, 1 December 2009.
- [110] L. Stepien, A. Roch, S. Schlaier, I. Dani, A. Kiriy, F. Simon, M. Lukowicz and C. Leyens, "Investigation of the Thermoelectric Power Factor of KOH-Treated PEDOT:PSS Dispersions for Printing Applications," *Energy Harvesting and Systems*, vol. 3, no. 1, 16 July 2015.
- [111] B. Thompson and H. Yoon, "Aerosol-Printed Strain Sensor Using PEDOT:PSS," *IEEE sensors journal*, vol. 13, no. 11, pp. 4256-4263, 25 June 2013.
- [112] A. Mahajan, C. D. Frisbie and L. Francis, "Optimization of Aerosol Jet Printing for High-Resolution, High-Aspect Ratio Silver Lines," *ACS Applied Materials & Interfaces*, vol. 5, no. 11, pp. 4856-4864, 9 May 2013.
- [113] A. Roch, M. Greifzu, E. R. Talens, L. Stepien, T. Roch, J. Hege, N. V. Nong, T. Schmiel, I. Dani, C. Leyens, O. Jost and A. Leson, "Ambient effects on the electrical conductivity of carbon nanotubes," *Carbon*, vol. 95, pp. 347-353, December 2015.
- [114] A. Chahadih, P. Y. Cresson, C. Mismar and T. Lasri, "V-Band Via-Less GCPW-to-Microstrip Transition Designed on PET Flexible Substrate Using Inkjet Printing Technology," *IEEE Microwave and Wireless Components Letters*, vol. 25, no. 7, pp. 436-438, 19 May 2015.

- [115] R. A. Serway, Principles of Physics, 2nd ed., Fort Worth, TX: Saunders College Pub., 2011.
- [116] D. J. Griffiths, Introduction to Electrodynamics, 3rd ed., Upper Saddle River, NJ: Prentice Hall, 1999.
- [117] P. Lascelles, M. Brown and D. Williams, "hum3 - Our Journey to Industrialisation," Heraeus, October 2020. [Online]. Available: https://www.heraeus.com/media/media/hng/doc_hng/industries_and_applications_1/arc_and_flash_applications_1/humm3_-_our_journey_to_industrialisation.pdf. [Accessed 22 July 2021].
- [118] F. Houtun, H. J. Chuncheng, Z. Limin and C. Fang, "Reduction of chloride matrix effect using silver oxide as a precipitating reagent for the determination of trace anions in chloride-rich samples via ion chromatography," *Journal of Separation Science*, vol. 30, no. 5, pp. 693-698, 20 March 2007.
- [119] E. S. Rosker, M. T. Barako, E. Nguyen, D. DiMarzio, K. Kisslinger, D.-W. Duan, R. Sandhu, M. S. Goorsky and J. Tice, "Approaching the Practical Conductivity Limits of Aerosol Jet Printed Silver," *Applied Materials & Interfaces*, pp. 29684-29691, 2020.
- [120] "Materials Project," Materials Project, 2021. [Online]. Available: <https://materialsproject.org/>. [Accessed 12 July 2021].
- [121] V. Sundaresan, J. W. Monaghan and K. A. Willets, "Visualizing the Effect of Partial Oxide Formation on Single Silver Nanoparticle Electrodissolution," *The Journal of Physical Chemistry*, pp. 3138-3145, 2018.
- [122] "Silver, Ag," Princeton.edu, [Online]. Available: <https://www.princeton.edu/~maelabs/mae324/glos324/silver.htm>. [Accessed 13 July 2021].
- [123] W. G. Moffat, G. W. Pearsall and J. Wulff, The structure and properties of materials, New York: McGraw Hill LLC, 1964.
- [124] K. Yvon, A. Bezing, P. Tissot and P. Fischer, "Structure and Magnetic Properties of Tetragonal Silver(I,III) Oxide, Ag₂O," *Journal of Solid State Chemistry*, vol. 65, pp. 225-230, 1986.
- [125] "Hum3™ - Intelligent heat for Automated Fibre Placement (AFP)," Heraeus Holding, 2021. [Online]. Available: https://www.heraeus.com/en/hng/products_and_solutions/arc_and_flash_lamps/humm3/humm3.html#tabs-115105-2. [Accessed 24 April 2021].
- [126] G. Kovacs, N. Maluf and K. Petersen, "Bulk micromachining of silicon," *Proceedings of the IEEE*, vol. 86, no. 8, pp. 1536-1551, 1998.
- [127] S. T. Cho, "Batch-dissolved wafer process for low-cost sensor applications," *Micromachining and Microfabrication Process Technology*, 19 Septemebr 1995.

- [128] Y. Gianchandani and K. Najafi, "A bulk silicon dissolved wafer process for microelectromechanical systems," in *International Electron Devices Meeting 1991 [Technical Digest]*, Washington, DC, USA, 1991.
- [129] E. Ciani, V. Foglietti, G. Caliano and M. Pappalardo, "Micromachined capacitive ultrasonic transducers fabricated using silicon on insulator wafers," *Microelectronic Engineering*, Vols. 61-62, pp. 1025-1029, July 2002.
- [130] J. Dong, D. Mukhopadhyay and P. M. Ferreira, "Design, fabrication and testing of a silicon-on-insulator (SOI) MEMS parallel kinematics XY stage," *Journal of Micromechanics and Microengineering*, vol. 17, pp. 1154-1161, 9 May 2007.
- [131] M. Yao, J. Wu, A. P. Zhang, H.-Y. Tam and P. K. A. Wai, "Optically 3-D μ -Printed Ferrule-Top Polymer Suspended-Mirror Devices," *IEEE Sensors Journal*, vol. 17, no. 22, pp. 7257-7261, 9 August 2017.
- [132] X. Lin, A. Hosseini, X. Dou, H. Subbaraman and R. T. Chen, "Low-cost board-to-board optical interconnects using molded polymer waveguide with 45 degree mirrors and inkjet-printed micro-lenses as proximity vertical coupler," *Optics Express*, vol. 21, no. 1, pp. 60-69, 2013.
- [133] R. Das, K. Ghaffarzadeh and X. He, "Flexible, Printed OLED Displays 2020-2030: Forecasts, Markets, Technologies," IDTechEx, 2020.
- [134] J. Perelaer, B. de Gans and U. Schubert, "Ink-jet Printing and Microwave Sintering of Conductive Silver Tracks," *Advanced Materials*, vol. 18, no. 16, pp. 2101-2104, August 2006.
- [135] J. Perelaer, M. Klokkenburg, C. E. Hendriks and U. S. Schubert, "Microwave Flash Sintering of Inkjet-Printed SilverTracks on Polymer Substrates," *Advanced Materials*, vol. 21, no. 47, pp. 4830-4834, 18 December 2009.
- [136] "Jetfirst 100/150 RTP," University of Michigan - LNF, 23 March 2020. [Online]. Available: https://lnf-wiki.eecs.umich.edu/wiki/Jetfirst_100_150_RTP. [Accessed 15 November 2020].
- [137] J. Li, X. Zhang, X. Liu, Q. Liang, G. Liao, Z. Tang and T. Shi, "Conductivity and foldability enhancement of Ag patterns formed by PVAc modified Ag complex inks with low-temperature and rapid sintering," *Materials & Design*, vol. 185, p. 108255, 5 January 2020.